2009-01-01

Monte-Carlo Ray-Trace Modelling of Quantum Dot Solar Concentrators

Manus Kennedy
Technological University Dublin

Monte-Carlo Ray-trace Modelling of Quantum Dot Solar Concentrators

Manus Kennedy BSc, MSc

Dublin Energy Lab.

Dublin Institute of Technology

Thesis submitted for PhD

October, 2009.

Supervised by

Professor Brian Norton

Dr. John Doran

Dr. Sarah McCormack

Abstract

Due to the finite resources of fossil fuel and nuclear reserves, renewable energy technologies must provide an increasing proportion of future energy needs, if the world's population are to expect a secure and sustainable developed society. Quantum dot solar concentrators (QDSCs) can potentially reduce the cost of photovoltaic (PV) electrical power generation and thereby further the growth in installed PV capacity. QDSCs can concentrate both the direct and diffuse components of solar radiation which makes them particularly suitable for climates where the diffuse component is predominant.

A QDSC model has been developed based on Monte-Carlo ray-trace techniques. The model allows the multiple competing, interdependent QDSC loss mechanisms to be quantified for any given set of device parameters. The model provides an important tool for optimizing QDSC design in terms of varying geometry, PV cell configuration, matrix material, and quantum dot types. Combining the ray-trace model with solar radiation models, diurnal and seasonal variations in QDSC performance can be analysed, and devices further optimised for outdoor conditions. Model predictions show that viable QDSCs are realizable provided efficient near infra-red emitting quantum dots can be exploited.

Declaration

I certify that this thesis which I now submit for examination for the award of PhD is entirely my own work and has not been taken from the work of others, save and to the extent that such work has been cited and acknowledged within the text of my work. This thesis was prepared according to the regulations for postgraduate study by research of the Dublin Institute of Technology and has not been submitted in whole or in part for another award in any Institute. The work reported on in this thesis conforms to the principles and requirements of the Institute's guidelines for ethics in research.

The Institute has permission to keep, lend or copy this thesis in whole or in part, on condition that any such use of the material of the thesis be duly acknowledged.

Signature _____ Date 17/12/09

Acknowledgements

This thesis would not have been possible without the excellent guidance and support I have received from my supervisors Dr. Sarah McCormack, Dr. John Doran and Prof. Brian Norton. I am very grateful to them for all their dedication. It has been a pleasure working with them on this project and I look forward to future collaborations together.

I would like to express my appreciation to all my colleagues for their continued support and encouragement over the last number of years. In particular, I would like to express my deep gratitude to Dr. Brenda Rowan who fabricated the quantum dot solar concentrator samples used in this study. I am very grateful to everyone in the FOCAS institute who provided me with invaluable advice and technical instruction.

To my friends and family, who provided me with much needed diversion, and support over the course of my studies, I will always be indebted. Thank you to Maite for being there throughout.

The support of Sustainable Energy Ireland, and the Research Support Unit at the Dublin Institute of Technology is gratefully acknowledged. I would also like to acknowledge the collaboration of the Molecular Based Concepts group, part of the EU-funded FULLSPECTRUM project.

Abbreviations

ARC	Anti-reflection coating
a-Si	Amorphous silicon
ASTM	American society for testing and materials
CdS	Cadmium sulphide
CdSe	Cadmium selenide
CdTe	Cadmium telluride
CIGS	Copper indium gallium selenide
CPC	Compound parabolic concentrator
EOT	Equation of time
EQE	External quantum efficiency
FOB	Fibre optic bundle
FRET	Förster resonant energy transfer
GaAs	Gallium arsenide
GaInP	Gallium indium phosphide
IQE	Internal quantum efficiency
LDS	Luminescent down shifting
LED	Light emitting diode
LSC	Luminescent solar concentrator
mc-Si	Multicrystalline silicon
MgF_2	Magnesium fluoride
NIR	Near infra-red
PbS	Lead sulphide
PbSe	Lead selenide
PC-LDS	Partially covered luminescent down shifting
PMMA	Polymethylmethacrylate
PV	Photovoltaic
QD	Quantum dot
QDSC	Quantum dot solar concentrator
QY	Quantum yield
RET	Renewable energy technology
Si	Silicon
SSR	Spectrally selective reflector
TIR	Total internal reflection
UV	Ultra-violet
W_p	Watt peak
ZnS	Zinc sulfide

Nomenclature		S.I. units
a	CPC entry aperture width	m
a'	CPC exit aperture width	m
A_{conc}	LSC top surface aperture area	m^2
A_{cs_FOB}	Cross sectional area of fibre optic bundle	m^2
A_{PV}	Area of attached PV cells	m^2
A_{FO}	Planar area of fibre optic in solar tree system	
B_h	Beam irradiance component on horizontal surface	$W\ m^{-2}$
B_t	Beam irradiance component on a tilted surface	$W\ m^{-2}$
c	Speed of light	$m\ s^{-1}$
C	Spectrally-specific solar energy concentration ratio	
C_1	Solar energy concentration ratio of solar leaf	
C_2	Solar energy concentration ratio of 2^{nd} stage concentrator	
C_G	CPC geometric concentration ratio	
C_{ph}	Photon count concentration ratio	
d	Distance between boundary intersection points	m
day_J	Julian day of the year	
D_{cs}	Circumsolar component of diffuse irradiance	$W\ m^{-2}$
D_h	Diffuse irradiance component on horizontal surface	$W\ m^{-2}$
D_{hz}	Horizon brightening component of diffuse irradiance	$W\ m^{-2}$
D_{iso}	Isotropic component of diffuse irradiance	$W\ m^{-2}$
D_t	Diffuse irradiance component on a tilted surface	$W\ m^{-2}$
D_t	Ground albedo reflected component on tilted surface	$W\ m^{-2}$
E_h	Extraterrestrial global horizontal irradiance	$W\ m^{-2}$
E_{in}	Input energy distribution	$Wm^{-2}nm^{-1}$
F_1	Circumsolar coefficient	
F_2	Horizon brightening coefficient	
f_{ij}	Perez coefficients	
G_{geom}	Geometric gain	
G_h	Global irradiance on horizontal surface	$W\ m^{-2}$
G_t	Global irradiance on a tilted surface	$W\ m^{-2}$
h	Planck's constant	$m^2\ kg\ s^{-1}$
I_0	Solar constant	
$I_{sc\ PV}$	Short circuit current of PV cells coplanar to concentrator	A
$I_{sc\ PV_C}$	Short circuit current of PV cell attached to concentrator	A
I_{sc}	Short circuit current	A
J_{sc}	Short circuit current density	A/m^2
k_a	Fraction of photons exiting fibre optic bundle within CPC θ_a	
k_D	Diffuse fraction	
k_r	Randomly generated number in the interval [0,1]	
k_T	Clearness index	
L_{loc}	Location longitude in degrees west of L_{ref}	degrees
L_{ref}	Reference longitude	degrees
n	Refractive index	
n_1	Refractive index at location of incident ray	
n_2	Refractive index at location of refracted ray	
n_{CPC}	Refractive index of dielectric filled CPC	

N_{FO}	Number of fibre optics in solar tree system	
N_{in}	Input photon distribution	photons s^{-1} m^{-2} nm^{-1}
N_{out}	Output photon distribution	photons s^{-1} m^{-2} nm^{-1}
$\boldsymbol{p}$	Normalised surface normal vector	
P_{abs}	Probability of absorption event	
R	Probability of reflection	
$R_{\parallel}$	Parallel polarised component of reflected light	
$R_{\perp}$	Perpendicularly polarised component of reflected light	
R_{mirror}	External mirror reflectivity	
R_{PV}	PV cell reflectivity	
R_{SSR}	Spectrally selective reflector reflectivity	
$\boldsymbol{v}$	Normalised ray vector	
$\boldsymbol{v}_{reflect}$	Reflected ray vector	
$\boldsymbol{v}_{refract}$	Refracted ray vector	
W_{FO}	Width of fibre optic	m
W_{Leaf}	Width of solar leaf	m
L_{Leaf}	Length of solar leaf	m
α_{mat}	Matrix material photon absorption coefficient	m^{-1}
α_{QD}	Quantum dot absorption coefficient	m^{-1}
α_{scat}	Matrix material photon scattering coefficient	m^{-1}
β	LSC surface tilt angle	degrees, radians
γ_p	LSC surface azimuth angle	degrees, radians
γ_s	Solar azimuth angle	degrees, radians
Δ	Sky brightness parameter	
δ	Solar declination	degrees, radians
η	Power conversion efficiency	
η_{abs}	Absorption efficiency	
$\eta_{int\ opt}$	Internal optical efficiency	
η_{opt}	Optical efficiency	
η_{ret}	Retention efficiency	
η_{TIR}	Total internal efficiency	
θ_a	CPC acceptance angle	degrees, radians
$\theta_{critical}$	Critical angle	degrees, radians
θ_{entry}	Optical concentrator entry aperture	degrees, radians
θ_{exit}	Optical concentrator exit aperture	degrees, radians
θ_{ip}	Angle of incidence on tilted planar surface	degrees, radians
θ_s	Solar zenith angle	degrees, radians
λ	Wavelength	nm
λ_{co}	Spectrally selective reflector "cut-off" wavelength	nm
ρ	Ground surface albedo	
Φ	Location latitude	degrees
ω	Solar hour angle	degrees, radians

Table of Contents

List of Figures

List of Tables

1 Introduction to quantum dot (luminescent) solar concentrators

1.0 The need for renewable energy sources

In 2007, 81% of world primary energy demand was met by coal, oil and gas resources - 26%, 34%, and 21% respectively - (International Energy Agency, 2009). Global primary energy demand continues to grow with an increasing human population and rising living standards. On average, demand increased by 2% per annum between 1971 and 2002, with higher percentage increases occurring in recent years (Goswami, 2007). Assuming a continued 2% annual increase, demand will have tripled by 2065. All proven global oil and natural gas reserves are predicted to last only until 2048 (Goswami, 2007) and 2065 (Breeze, 2005), respectively. Although coal reserves will last much longer, CO_2 emissions produced in coal-burning power stations make it an unviable option as the primary fuel for electricity generation. Nuclear power generation is one potential solution to fill the gap left by depleting fossil fuel reserves. However, finite resources of Uranium, currently the primary nuclear fuel used in reactors, mean that nuclear power is unlikely to be able to provide a significant proportion of energy needs in the near future (Kreith and Goswami, 2007). Furthermore, nuclear resources are concentrated in a limited number of regions in the world which would mean a poor security of supply for most of the world's countries if they become overly reliant on nuclear fuels. Due to the finite resources of fossil fuel and nuclear reserves, renewable energy technologies

(RETs) must provide an increasing proportion of future energy needs[i], if the world's population are to expect a secure and sustainable developed society. Furthermore, international commitments to reducing greenhouse gas emissions may mean that countries face financial penalties for failing to meet certain RET targets. For example, the European Union has set a target of 20% of primary energy demand to be met by RET by 2020, with financial penalties for member states failing to meet final and intermediate targets across each energy sector.

Electricity generation currently accounts for over 30% of global primary energy demand (Kreith and Goswami, 2007). In 2006, RETs provided 18% of electricity supply, the vast majority of which was hydro-electric, as shown in Figure 1.1 (International Energy Agency, 2009). Photovoltaic (PV) technologies supplied 0.015%. The solar energy resource available is immense, however. The solar energy received by the earth in one *hour* could meet the current global *annual* primary energy demand (Morton, 2006). Solar technologies, both direct (PV, solar thermal) and indirect (wind, wave and biomass) can meet a significant proportion of future electricity needs if expected manufacturing cost and technological developments materialise, and the political will on a global scale is present (deVries *et al.*, 2007, Resch *et al.*, 2008). This chapter introduces the luminescent solar concentrator (LSC), a device which can potentially reduce the cost of PV electrical power generation and, therefore, further the growth in installed PV capacity. An overview is given of the current state of development of LSCs and of *quantum dot* luminescent solar concentrators.

---

[i] along with developments in energy efficiency and conservation

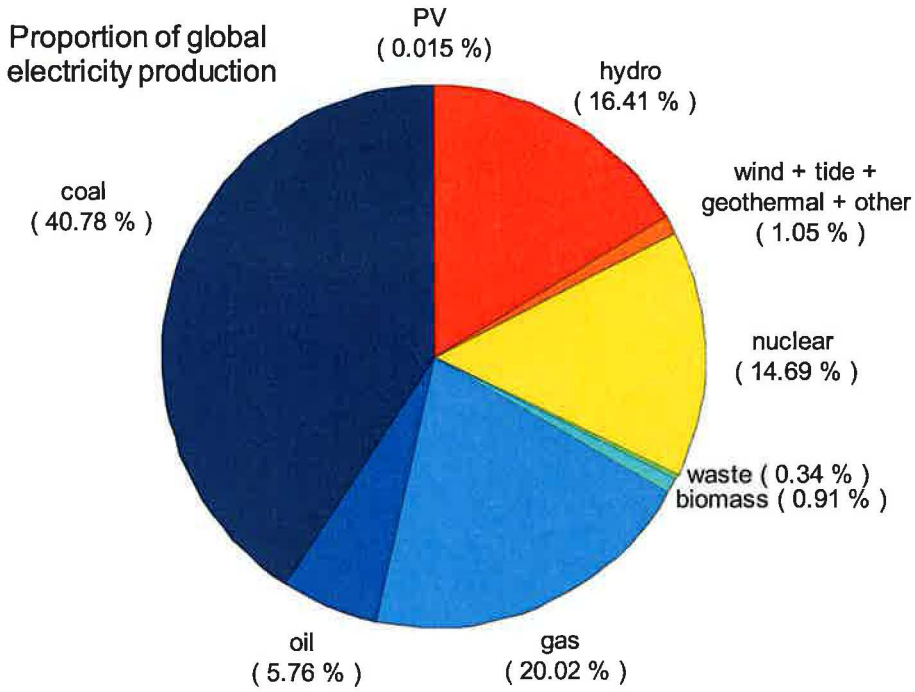

Figure 1.1. Supply of global electricity by fuel type in 2006 (IEA, 2009). Renewable energy technologies accounted for ~18%, of which hydro-electric was the predominant source. Photovoltaics (PV) accounted for 0.015% of global supply.

1.1 Photovoltaics

Global photovoltaic production has grown by an average of 33% per annum in the period 1993 – 2007, as shown in Figure 1.2 (Observ'ER, 2008). Silicon wafer, or "1st generation" PV technologies currently account for 90% of the market share of current PV production (Bagnall, 2008). Production costs are typically quoted per Watt peak (W_p) generated under standard test conditions (STC). Costs have decreased as production capacity and scale has increased and manufacturing methods improved. At an average module production cost of US$ 2.75 / W_p (Margolis *et al.*, 2006), this is too high for PV to compete with conventional energy sources in most

locations worldwide, in the absence of government capital grants or feed-in tariff subsidies. The two principal barriers prohibiting more widespread uptake of PV technology are;

(i) the low energy intensity and variation in energy supply caused by diurnally and seasonally changing solar radiation, and by changing atmospheric and air-mass conditions.

(ii) the manufacturing and installation costs of a solar panel array and balance-of-system components.

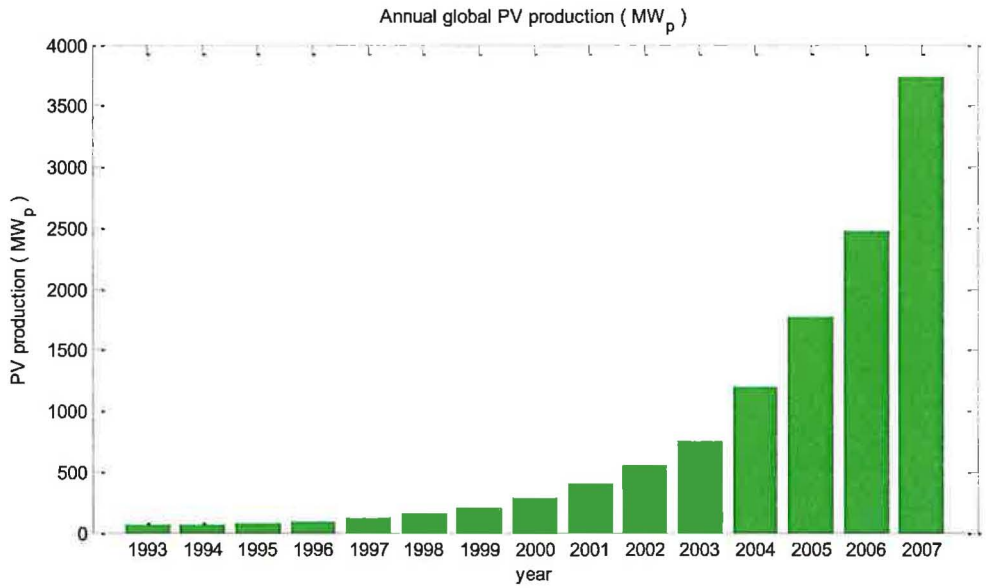

Figure 1.2. Global PV production (MW_p) increased annually by an average of 33% in the period 1993-2007 (Observ'ER, 2008).

"2nd generation" PV technologies such as CdTe (Cadmium telluride) and CIGS (Copper indium gallium selenide) cells can reduce manufacturing costs, as total material costs are lower to produce these *thin-film* cells. For example, FirstSolar currently produce thin-film CdTe modules at ~US$ 1/W_p (FirstSolar, 2009). Another approach to reducing the cost of PV electricity is to concentrate solar energy on to a reduced area of solar cell, thereby reducing the material costs per unit power

produced. Examples of different concentrator types, which have been developed to date for use with PV cells, are outlined in section 1.2

1.2 Optical concentrators of solar energy

The theoretical maximum concentration ratio of an optical concentrator spatially receiving uniform insolation (Winston, 1976, Smestad *et al.*, 1990) is given by;

$$C \leq \frac{\sin^2 \theta_{exit}}{\sin^2 \theta_{entry}} = \frac{1}{\sin^2 \theta_{entry}} \quad \text{(assuming exit angle, } \theta_{exit}, = 90^\circ) \qquad 1.1$$

where θ_{entry} and θ_{exit} are the incident angles at the entry and exit apertures of the concentrator, respectively, as shown in Figure 1.3.

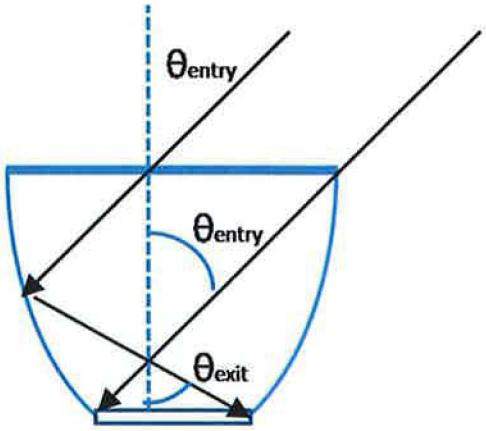

Figure 1.3. Optical concentrator with reflective surfaces (Smestad *et al.*, 1990). The maximum concentration ratio is given by eqn. 1.1.

If the concentrator is made of a medium with refractive index n, and the solar absorber at the exit aperture is immersed in the same medium, it can be shown from Snell's law that the maximum C is enhanced by a factor of n^2 (Smestad *et al.*, 1990).

$$C \leq n^2 \frac{\sin^2 \theta_{exit}}{\sin^2 \theta_{entry}} \qquad 1.2$$

For $n = 1.5$, theoretical C of 10^5 are possible (excluding external Fresnel reflection losses), limited by the sun disk's angular size of ~0.27°.

Many reflector and lens based optical concentrators, using solar tracking devices, have been designed demonstrating very high concentration ratios. The fraction of the *diffuse* component of solar radiation accepted by these concentrator systems is inversely proportional to the concentration ratio. In climatic regions where overcast weather conditions are common, the diffuse component of solar radiation may be greater than the direct component. For example, as shown in section 5.1.1, the diffuse and direct components of the measured annual global insolation on a horizontal surface at a particular site in Dublin, Ireland, were 77% and 23%, respectively. Optical concentrators with a high concentration ratio, C, are not practical in climates where the diffuse component is predominant. Optical concentrators with lower C can accept a higher proportion of the diffuse component. Some particular examples are described below in sections 1.2.1 and 1.2.2. It should be noted, however, that all optical concentrators are subject to the constraint given by eqn. 1.2, whereby increasing the acceptance angle (to accept diffuse light) decreases the maximum possible concentration ratio attainable by the device.

1.2.1 Compound parabolic concentrators with high acceptance angles

The compound parabolic concentrator, CPC, (Hinterberger and Winston, 1966; Winston, 1974) can be optimised, whereby lowering the CPC geometric concentration ratio results in a higher proportion of the diffuse component of incident solar radiation being accepted. A trade-off exists between increasing the geometric concentration ratio, C, and decreasing the acceptance angle. CPCs with a high angular acceptance can operate efficiently without the need for (and the additional capital and maintenance cost of) solar tracking mechanisms. Mallick *et al.* have demonstrated solar energy concentration ratios, C, of 1.62 and 2.01 for building-integrated, wall façade, asymmetrical CPCs with geometric concentration ratios of 2 and 2.45, respectively (Mallick *et al.*, 2006; Mallick and Eames, 2007). The respective acceptance half angles of 50° and 37° mean that a significant proportion of the diffuse component of incident solar radiation is collected by both devices, and the direct component can be collected throughout the day without solar tracking. A reduction of 40% in cost per W_p, compared to a reference non-concentrating panel utilizing the same solar cells, is estimated for the CPC panel with acceptance half angle of 37° (Mallick and Eames, 2007).

1.2.2 Flat plate optical concentrators of diffuse radiation

As noted in section 1.2, the higher the required optical concentrator acceptance angle, the lower the possible C. From eqn. 1.2, the maximum C attainable for isotropically diffuse light ($0 \leq \theta_1 \leq 90°$) is $n^2 = 2.2$, assuming $n = 1.5$. Di-

electric transparent plates with Lambertian or v-grooved rear reflecting surfaces (Smestad and Hamill, 1984, Uematsu *et al.*, 2001) can be used as flat plate static concentrators of direct and diffuse radiation. Incident photons reflected at the rear reflector are trapped within the plate by total internal reflection and transmitted to a reduced area (relative to the concentrator entry aperture area) of PV cell, as shown in Figure 1.4(a). Measured optical efficiencies, over all angles of incidence, range from 60% to 85% for a device with a geometric concentration ratio of 2.0. Potential module costs per W_p are estimated at 15% lower than a non-concentrating PV module utilizing the same PV cells (Weber *et al.*, 2006).

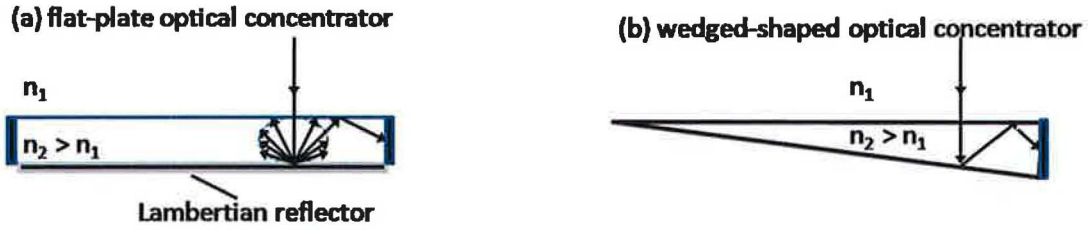

Figure 1.4. (a) Dielectric flat-plate (Smestad and Hamill, 1984), utilising a lambertian rear reflector and (b) wedge-shaped (Maruyama and Osako, 1999) optical concentrators. In (a) and (b), incident rays may be reflected at an angle within the angular range for total internal reflection to occur and is guided to the exit aperture at plate edges.

Other static concentrator designs exist, which utilise reflection and refraction, to concentrate light over a wide incident angular range, e.g. the wedge shaped concentrator (Maruyama and Osako, 1999) shown in Figure 1.4(b). The n^2 concentration limit for diffuse radiation applies to *all* such optical concentrators. This limit does not apply, however, to *luminescent* solar concentrators, LSCs (Smestad *et al.*, 1990), shown in Figure 1.5. Therefore, much higher diffuse radiation concentration ratios are possible with non-optical LSCs than is the case for optical

concentrators. In this thesis, the potential optical performance of LSCs is analysed using ray-trace modelling.

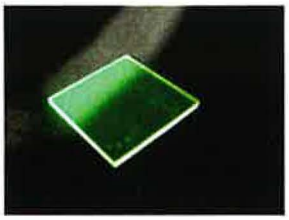

Figure 1.5. Flat-plate luminescent (non-optical) solar concentrator without PV cells or external reflectors attached.

1.3 Luminescent solar concentrators

Luminescent solar concentrators, LSCs, (Weber and Lambe, 1976; Goetzberger and Greubel, 1977) are non-optical concentrators which can concentrate both direct and diffuse radiation. As incident insolation passes through an LSC device matrix consisting of a flat polymer plate doped with a luminescent dye, as shown in Figure 1.6, it is absorbed by the dye. Light emitted by the luminescent dye in the device matrix is transmitted by total internal reflection (TIR) to the plate edges, where PV cells are attached. The solar energy concentration effect arises as the exit aperture surface area at the plate edges is much smaller than the top surface aperture area. External reflectors may be placed adjacent and parallel to plate surfaces to reflect light that may outside the angular range for TIR.

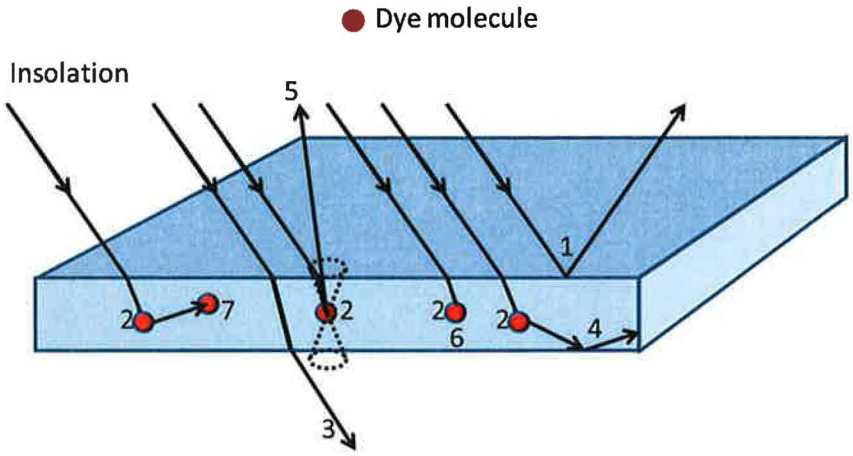

Figure 1.6. Schematic of LSC without PV cells or external mirrors attached. Incident photons may be externally reflected [1], or transmitted into the plate. Photons may be absorbed by a dye molecule [2] in the plate, or transmitted through the plate [3], depending on the dye absorption coefficient and the pathlength through the plate. Energy absorbed by the dye molecule may be re-radiated at a longer wavelength within the angular range for total internal reflection to occur [4], or within the "escape-cone" of the plate [5]. An absorption event may result in no luminescence from the dye molecule [6] whereby the absorbed energy is converted to heat. Dye emitted photons may be absorbed by another dye molecule within the plate (so-called "re-absorption") [7], after which [4], [5], or [6] may ensue. Photon attenuation also occurs within the plate, and photons within the escape-cone may be reflected or refracted at plate boundaries.

Advantages of luminescent solar concentrators include;

- The concentration limits of optical concentrator systems do not apply (Smestad *et al.*, 1990). Therefore, LSCs can concentrate both the direct and diffuse components of solar radiation.
- Solar tracking is not required for LSCs to operate efficiently.
- The flat-plate structure makes them suitable for building integrated applications.
- The overall capital cost of the concentrator components is low, as shown in section 6. Richards *et al.* (2007) estimated LSC plate (without PV cells) production costs to be potentially as low as €24/m^2, ~15 times lower than

conventional crystalline silicon PV modules. Therefore, the LSC has the potential to significantly reduce the cost of PV electrical power generation.

- The cells receive light collected from a large plate area, so they are less sensitive to partial shading effects which can cause a severe decrease in PV cell power output and damage cells (Sakuta *et al.*, 1994).
- High energy incident photons are down-shifted in the host matrix material by the luminescent species[ii]. Photons emitted by the luminescent species are better matched to the band gap energy of the attached PV cell, so thermalisation at the cell is reduced.
- Stacked layered devices may be used, where each layer collects a different part of the solar spectrum and different cells are attached to each layer (with the band-gap of the cell matched to the emission wavelength of the luminescent species in each layer), theoretically allowing higher overall power conversion efficiency than a single band-gap cell (Goetzberger and Wittwer, 1981; Goldschmidt *et al.*, 2006).

[ii] [ii] Down-shifting is defined distinctly from the process of down-conversion. In the former case, energy is lost in the form of heat when high energy photons are absorbed. In the latter case multiple low energy photons are emitted following the absorption of a high energy photon, i.e., there is no loss of light energy.

1.4 High efficiency LSCs and performance comparative measures

The retention efficiency of an LSC plate (i.e. the fraction of emitted photons trapped within the plate by TIR) is a function of the plate refractive index, n, as is shown in section 2.2.6. A typical value of n in LSCs is ~1.5. It can be shown that, in this case, the retention efficiency is 75%. The overall LSC power conversion efficiency, η, is limited by the power conversion efficiency of the attached PV cell, η_{PV}. In an idealised LSC (assuming external reflection losses and transport losses within the plate to be zero) with a monocrystalline silicon cell attached (where η_{PV}=20%), LSC η could, therefore, approach 15% (i.e., 75% of 20%). However, due to device loss mechanisms, which are detailed in section 1.3, real η are typically much lower than 15%. High η LSCs reported in the literature are listed in Table 1.1. While a viable LSC device should have an acceptably high η, it is important not to compare two devices solely by the respective η. It is also important to consider the LSC geometric gain, which is defined as the ratio of the top surface aperture area to the area of attached solar cell. For example, consider LSC 7(a) and LSC 7(b), listed in Table 1.1, fabricated using the same plate materials and solar cells;

- LSC 7(b) has a geometric gain, G_{geom}, of 2.5 and η is 7.1%, the record LSC efficiency currently quoted in the literature. LSC 7(a) has G_{geom} of 10 and η is reduced to 4.6%. Owing to transport losses within the plate, LSC efficiency is inversely proportional to G_{geom}. However, larger LSCs have higher concentration ratios. Consequently, LSC 7(a) may be a more optimal device, despite the lower efficiency attained. Therefore, η is only a useful comparative measure of two LSCs if G_{geom} are approximately equivalent.

The PV cell type varies between LSCs, thereby affecting the overall η, for example;

- LSCs 2(a) and 2(b) have η of 2.1% and 2.5%, employing Si and GaAs cells, respectively. Currie *et al.* (2008) estimate that GaAs and GaInP costs could reduce to ~US\$50/W_p at large scale production. This is an order of magnitude higher than silicon PV cells. LSC performance should therefore be evaluated taking into account realistic cell costs, and not only η attained.

It is also important to take into account which external reflectors are used, for example;

- LSCs 4(a) and 4(b) are equivalent in dimensions and cell type used, but 4(b) employs a spectrally selective reflector layer to minimise escape cone losses. η increases from 2.6% to 3.1% with the inclusion of the layer.

The general approach adopted in this research is to quantify LSC *concentration ratio*, C, as a function of device size, rather than quantify η at a *single* particular device size. From C, the power output can be calculated and, under certain cost assumptions, the cost per W_p (either relative or absolute) determined. Any two LSC configurations can thus be compared (or a given LSC compared with a conventional PV cell) by its cost per unit power output.

Configuration	#	G_{geom}	Dye materials	PV cell type	η (%)	Reference
Single-plate single dye	1	16	KF-241.	Si	2.3	Sidrach de Cardona *et al.*, 1985b
	2	33.3	Not given.	(a) Si	2.1	Wittwer *et al.*, 1984
				(b)GaAs	2.5	
	3	16.7	Lumogen Red 305.	Si	2.4	van Sark *et al.*, 2008
	4	20	(a) BA241.	GaInP	2.6	Goldschmidt *et al.*, 2009
			(b) BA241+ Rugate spectrally selective reflector top layer	GaInP	3.1	
	5	(a) 3	DCJTP.	GaInP	5.9*	Currie *et al.*, 2008
		(b) 45	DCJTP.	GaInP	4.0*	
Single-plate multiple dye	6	16.7	Lumogen Red 305 + Coumarin yellow.	Si	2.7	van Sark *et al.*, 2008
	7	(a) 10	Lumogen Red 305 + Coumarin yellow.	GaAs	4.6	Slooff *et al.*, 2008
		(b) 2.5	Lumogen Red 305 + Coumarin yellow.	GaAs	7.1	
	8	Not given	Lumogens Violet 570 + Yellow 083 + Orange 240 + Red 300.	Si	4.4†	Richards and McIntosh, 2006
	9	(a) 3	Rubrene + DCJTB. FRET	GaInP	5.5*	Currie *et al.*, 2008
		(b) 45	Rubrene + DCJTB. FRET	GaInP	4.7*	
Stacked systems	10	16.7	Not given	GaAs	4.0	Wittwer *et al.*, 1984
	11	0.83	BA241 + BA856	GaInP	6.7	Goldschmidt *et al.*, 2009

Table 1.1. Power conversion efficiency, η, for LSCs of varying configurations. †model prediction. *measured edge photon flux used to predict η from theoretical PV cell data. FRET: Förster resonant energy transfer. DCJTB: 4-(dicyanomethylene)-2-t-butyl-6-(1,1,7,7-tetramethyljulolidyl-9-enyl)-4H-pyran.

1.4.1 Thin-film LSCs

Thin-film LSCs, shown in Figure 1.7, consist of a highly doped thin-film (< 0.1 mm) polymer layer supported on a transparent polymer or glass substrate. One motivation for thin-film LSCs being developed was the theory that luminescence is transported to the PV cell primarily through the highly transparent substrate plate, thereby reducing re-absorption losses (Reisfeld *et al.*, 1988c). However, photons transported by TIR still must pass through the more heavily doped thin-film layer. Assuming the probability of absorption over any distance is given by the Beer-Lambert law, re-absorption losses should be equivalent in thin-film LSC and homogeneously doped LSC plate configurations. Bose *et al.* (2007) showed that both configurations attained approximately equal efficiency when the absorbance was equivalent in each configuration.

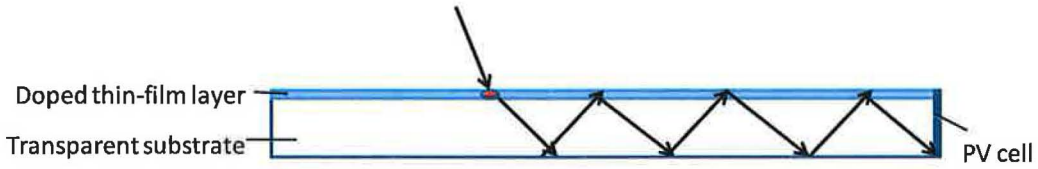

Figure 1.7. Thin-film LSCs consist of a highly doped thin-film polymer layer supported on a transparent substrate.

The most interesting characteristic of thin-film LSCs, however, is that (non-radiative) Förster resonant energy transfer (FRET) may take place between different dyes if the distance between dye molecules is small (Swartz *et al.*, 1977). This technique has been used in LSCs comprised of multiple thin-film layers, each doped with a distinct dye, on glass or polymer substrates (Bailey *et al.*, 2007; Currie *et al.*, 2008). These thin-film LSCs partly overcome the problem of re-absorption and associated escape-cone losses, which occur in multiple dye *homogeneously doped*

LSCs (Burgers *et al.*, 2006; Richards and McIntosh, 2006; Kennedy *et al.*, 2008b). The thin-film LSC 9 (b) listed in Table 1.1, which has an efficiency of 4.7% at a large plate size (G_{geom}), shows that this is a very promising approach for achieving efficient LSCs with broadband absorption of the solar spectrum.

1.5 LSC stability and absorption range limitations

For viable LSCs to be realised, dye absorbance, luminescence, and the matrix material transmittance all need to be stable, ideally over the lifetime of the attached solar cells (>20 years). A dye LSC containing a Perylene (Lumogen F Red) exhibited <3% absorbance degradation after 595 days in outdoor testing (van Sark *et al.*, 2008). The change in *electrical* output of this plate over time was not measured, however. A separate Lumogen F Red 305 sample which showed almost zero degradation in absorbance after 205 days outdoor testing exhibited a decrease of ~15% in short circuit current over the same time period, showing that stability measurements of absorbance alone are not sufficient. Suggested explanations for the observed decrease in short circuit current were i) a possible decrease in the dye luminescent quantum yield, and/or ii) an increase in transport losses caused by a small increase in matrix absorption (van Sark *et al.*, 2008). A study by Currie *et al.* (2008) found an 8% decrease in edge luminescence for an LSC after accelerated indoor testing, where the integrated solar flux corresponded to an equivalent of ~3 months outdoor exposure. However, the authors expected that lifetimes would approach organic LED standards of lifetime of 10 to 100 years, when samples

incorporate a UV filter as is the case with organic LED devices. Stability of dye LSCs currently remains a significant barrier to realizing viable devices.

The absorption range of current dye LSCs is limited to the visible range of the solar spectrum, as illustrated in Figure 1.8, and therefore only a fraction of the available solar spectrum is converted to electricity. Near infra-red (NIR) absorbing dyes are not suitable for inclusion in LSCs owing to low quantum yields and poor stability (Friedman and Parent, 1987; Richards and McIntosh, 2006; Rowan *et al.*, 2008). Semiconductor nanocrystals, or quantum dots (QDs), can potentially overcome both stability and absorption range limitations of luminescent dyes as discussed in section 1.6.

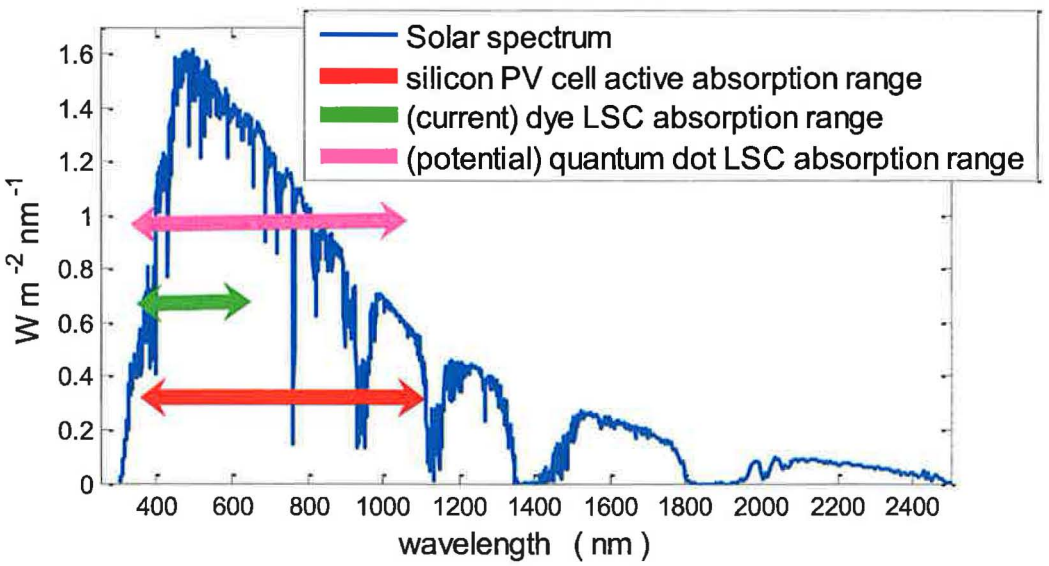

Figure 1.8. The absorption range of current dye luminescent solar concentrators (LSC) is limited to the visible range of the solar spectrum, and therefore only a fraction of the available solar spectrum is converted to electricity. Quantum dot luminescent solar concentrators, can potentially overcome absorption range limitations (and stability limitations) of organic dye LSCs.

1.6 Quantum Dot Solar Concentrators

A Quantum Dot Solar Concentrator, QDSC, (Barnham *et al.*, 2000; Chatten *et al.*, 2003; Gallagher *et al.*, 2004; Schüler *et al.*, 2007) employs quantum dots (QDs) rather than a luminescent dye in the device matrix. One advantage of using QDs is the ability to spectrally tune a device by varying the dot size to collect specific wavelengths in the solar spectrum. Secondly, as QDs are composed of crystalline semiconductor materials, they should exhibit a greater resistance than dyes to degradation in ultra-violet light (Chatten *et al.*, 2003). For an LSC[iii] with Si cells attached, the ideal single luminescent species would absorb light from the UV region of the solar spectrum up to ~900 nm and emit at ~950 nm, just below the band gap of silicon (Richards, 2007). PbS QDs can be tuned to exhibit the required broad absorption and NIR emission by controlling the QD size. However, commercially available PbS QDs currently have low quantum yields, QY, of ~10% (Rowan *et al.*, 2008), where QY is defined as the ratio of photons emitted to photons absorbed by a QD.

The optical efficiency of currently fabricated QDSCs, incorporating visible-emitting QDs, has been limited by reduced QY and by large overlaps between QD emission and absorption spectra (Hyldahl *et al.*, 2009; Rowan *et al.*, 2008; Sholin *et al.*, 2007). Spectral overlap results in QD-emitted photons being re-absorbed in the plate before reaching the PV cell, giving both higher escape cone losses and higher QY losses. More efficient QDSCs would result if spectral overlap could be reduced. Patanè *et al.* (2000) and Chatten *et al.* (2003) have shown that the emission spectrum

---

[iii] (The term "LSC" used within this work refers both to QDSCs and organic dye LSCs, unless specified otherwise. The term "QDSC" specifically refers to QD devices, however many results/conclusions for QDSCs given are also applicable, in general, to dye LSCs)

peak wavelength is related to the spread of QD sizes in a sample, which can be determined during the growth process. One objective of the present research is to quantify the realistic potential performance of QDSCs, incorporating current commercially-available QD types subject to the re-absorption limitations arising from spectral overlaps between QD emission and absorption spectra.

1.7 Modelling LSCs through a Monte-Carlo ray-trace approach

Monte-Carlo ray-trace modelling is used to analyse LSC performance. The advantages of adopting a ray-trace approach are a) it allows varying plate geometries to be modelled, and b) it can be combined with solar radiation models to investigate diurnal and annual variations in electrical output for varying device configurations. Within the ray-trace model, a *Monte-Carlo* method, detailed in section 2, is used to determine the path and eventual outcome of each incident ray vector representing an incident photon. In doing so, LSC loss mechanisms can be quantified for a given set of device parameters. Analytic, *deterministic* expressions have previously been derived to quantify individual LSC loss mechanisms (Goetzberger and Wittwer, 1981; El-Shaarawy *et al.*, 2007). In QDSCs, in particular, it is critical to accurately account for re-absorption losses as large spectral overlaps exist between QD photon emission and absorption spectra, and luminescent QYs are currently significantly lower than the most efficient organic dyes. Re-absorption losses can be calculated analytically in the limit of zero matrix material absorption and scattering losses

(Batchelder *et al.*, 1979). A *Monte-Carlo* model allows *all* interdependent, competing loss mechanisms to be quantified for *any* given set of device parameters.

1.8 Research objectives

The primary research objectives are outlined below in sections 1.8.1-1.8.5.

1.8.1 Model development and validation;

The principal objectives of this section are to;

- Implement a multi-parameter LSC model using a Monte-Carlo ray-trace approach.
- Validate model predictions for varying LSC size, shape, doping concentration (of single/multiple species), and matrix material refractive index, through comparison with measurements from previously fabricated LSCs and with predictions from other modelling techniques.

1.8.2 Investigation of QDSC geometries

Quantifying the net effect of varying device geometry on QDSC solar energy concentration ratios, C, is a non-trivial problem owing to the multiple, interdependent, competing loss mechanisms in the device. The optimum geometry is

ultimately that which minimises the costs per unit power generated. The principal objectives of this section are to;

- Analyse the effect of varying 2-D planar geometry on C using the ray-trace model.
- Determine the optimum geometry type and optimum plate size for any given set of device parameters.
- Investigate 3-D geometries to determine whether re-absorption losses within the plate can be reduced.

1.8.3 Quantifying QDSC performance for varying material properties

The effect of varying QD, matrix material, and external reflector optical properties on QDSC performance can be analysed using the model. While maximizing QDSC efficiency ultimately remains an experimental challenge, modelling can be used to investigate under what circumstances certain goals are attainable. The principal objectives of this section are to;

- Quantify the realistic potential performance of QDSCs, incorporating current commercially-available QD types.
- Investigate QDSC performance for varying external reflector types.

1.8.4 Outdoor modelling and annual energy yield predictions

The ray-trace model can be combined with solar radiation models to investigate the outdoor performance of a QDSC. The concentration ratio of QDSCs varies diurnally

and seasonally due to variation in incident insolation spectra and in incident angle distribution. The principal objective of this section is to;

- Analyse the effect of varying device parameters on annual *energy yields* and, in particular, quantify the effect of tilt angle, plate refractive index, and external anti-reflective coating layers on device energy yield.

1.8.5 Quantum dot luminescent down-shifting layers

PV cell short circuit current, I_{sc}, can be enhanced through the application of a luminescent down-shifting (LDS) layer. In the literature, quoted mc-Si cell I_{sc} enhancement predictions for LDS layers incorporating *quantum dots* are higher than that for LDS layers incorporating organic *dyes*. The principal objectives of this section are to;

- Investigate, using the ray-trace model, whether the optical properties of QDs make them more suitable candidates than organic dyes for incorporation in LDS layers.
- Quantify the electrical output of "partially-covered" LDS layers, of varying sizes and PV cell areas.

1.9 Chapter conclusions

- Due to the finite resources of fossil fuel and nuclear reserves, renewable energy technologies must provide an increasing proportion of future energy needs, if the world's population are to expect a secure and sustainable developed society.
- Luminescent solar concentrators, LSCs, can potentially reduce the cost of PV electrical power generation and further the growth in installed PV capacity.
- LSCs can concentrate both the direct and diffuse components of solar radiation. Solar tracking is not required for LSCs to operate efficiently. The flat-plate structure makes them suitable for building integrated applications.
- Stability of dye LSCs currently remains a significant barrier to realizing viable devices. The absorption range of current efficient dye LSCs is limited to the visible range of the solar spectrum. Semiconductor nanocrystals, or quantum dots (QDs), can potentially overcome absorption range and stability limitations characteristic of dye LSCs.
- A validated ray-trace model can be used to investigate the effect of varying QD, geometry, and matrix material types on QDSC costs per unit power output and energy yield.

1.10 References

Bagnall, D.M., (2008). Photovoltaic technologies. *Energy Policy,* 36, 12, 4390-6.

Bailey, S.T., Lokey, G.E., Hanes, M.S., Shearer, J.D.M., McLafferty, J.B., Beaumont, G.T., Baseler, T.T., Layhue, J.M., Broussard, D.R., Zhang, Y., Wittmershaus, B.P., (2007). Optimized excitation energy transfer in a three-dye luminescent solar concentrator. *Solar Energy Materials and Solar Cells,* 91, 1, 67-75.

Barnham, K.W.J., Marques, J.L., Hassard, J., O'Brien, P., (2000). Quantum dot concentrator and thermodynamic model for the global redshift. *Applied Physics Letters,* 76, 9, 1197-9.

Batchelder, J.S., Zewail, A.H., Cole, T., (1979). Luminescent solar concentrators. 1:Theory of operation and techniques for performance evaluation. *Applied Optics,* 18, 18, 3733-54.

Bose, R., Farrell, D.J., Chatten, A.J., Pravettoni, M., Büchtemann, A., Barnham, K.W.J., (2007). Novel configurations of luminescent solar concentrators. *Proceedings of 22nd European Photovoltaic Solar Energy Conference and Exhibition*, Milan, Italy, 210-4.

Breeze, P., (2005). *Power generation technologies*, Newnes/Elsevier, Burlington, USA.

Chatten, A.J., Barnham, K.W.J., Buxton, B.F., Ekins-Daukes, N.J., Malik, M.A., (2003). A new approach to modelling quantum dot concentrators. *Solar Energy Materials and Solar Cells,* 75, 3-4, 363-71.

Currie, M., Mapel, J.K., Heidel, T.D., Goffri, S., Baldo, M.A., (2008). High-Efficiency Organic Solar Concentrators for Photovoltaics. *Science,* 321, 226-8.

deVries, B.J.M., van Vuuren, D.P., Hoogwijk, M.M., (2007). Renewable energy sources: Their global potential for the first-half of the 21st century at a global level: An integrated approach. *Energy Policy,* 35, 2590-610.

El-Shaarawy, M.G., El-Bashir, S.M., Hammam, M., El-Mansy, M.K., (2007). Bent fluorescent solar collectors (BFSCs): Spectroscopy, stability and outdoor performance. *Applied Physics,* 7, 643-9.

FirstSolar, Arizona, USA, (2009). CdTe thin film modules. www.firstsolar.com (last accessed 10/9/09)

Friedman, P.S., Parent, C.R., (1987). Luminescent Solar Concentrator Development. Final Subcontract Report. Solar Energy Research Institute, Department of Energy, USA.

Gallagher, S.J., Eames, P.C., Norton, B., (2004). Quantum dot solar concentrator behaviour predicted using a ray trace approach. *International Journal of Ambient Energy,* 25, 1, 47-56.

Goetzberger, A., Wittwer, V., (1981). Fluorescent Planar Collector-Concentrators: A Review. *Solar Cells,* 4, 3-23.

Goldschmidt, J., Glunz, S.W., Gombert, A., Willeke, G., (2006). Advanced Fluorescent Concentrator. *Proceedings of Proceedings of 21st European Photovoltaic Conference*, Dresden, Germany, 107-10.

Goldschmidt, J., Peters, M., Bosch, A., Helmers, H., Dimroth, F., Glunz, S.W., Willeke, G., (2009). Increasing the efficiency of fluorescent concentrator systems. *Solar Energy Materials and Solar Cells,* 93, 176-82.

Goswami, D.Y., (2007). Energy: The Burning Issue, *reFOCUS*, January/February, 22-25.

Hinterberger, H., Winston, R., (1966). Efficient Light Coupler for Threshold Cherenkov Counters. *Review of Scientific Instruments,* 37, 1094-5.

Hyldahl, M.G., Bailey, S.T., Wittmershaus, B.P., (2009). Photo-stability and performance of CdSe/ZnS quantum dots in luminescent solar concentrators. *Solar Energy,* 83, 566-73.

International Energy Agency, (2009). www.iea.org/Textbase/stats/ (last accessed 20/9/09)

Kennedy, M., Dunne, M., McCormack, S.J., Doran, J., Norton, B., (2008). Multiple dye luminescent solar concentrators and comparison with Monte-Carlo ray-trace predictions. *Proceedings of 23rd European Photovoltaic Solar Energy Conference and Exhibition*, Valencia, Spain, 390-3.

Kreith, F., Goswami, D.Y., (2007). *Handbook of energy efficiency and renewable energy*, CRC Press, Boca Raton, USA.

Mallick, T.K., Eames, P.C., (2007). Design and fabrication of low concentrating second generation PRIDE concentrator. *Solar Energy Materials and Solar Cells,* 91, 7, 597-608.

Mallick, T.K., Eames, P.C., Norton, B., (2006). Non-concentrating and asymmetric compound parabolic concentrating building façade integrated photovoltaics: An experimental comparison *Solar Energy,* 80, 834-49.

Margolis, R., Mitchell, R., Zweibel, K., (2006). Lessons Learned from the Photovoltaic Manufacturing Technology/PV Manufacturing R&D and Thin-Film PV Partnership Projects. National Renewable Energy Laboratory (NREL).

Maruyama, T., Osako, S., (1999). Wedge-shaped light concentrator using total internal reflection. *Solar Energy Materials and Solar Cells,* 57, 1, 75-83.

Morton, O., (2006). Solar energy: A new day dawning?: Silicon Valley sunrise. *Nature,* 443, 19-22.

Observ'ER, (2008). Photovoltaic Barometer. www.eurobserver-er.org/pdf/baro184.pdf (last accessed 20/9/09)

Patanè, A., Levin, A., Polimeni, A., Eaves, L., Main, P.C., Henini, M., (2000). Carrier thermalization within a disordered ensemble of self-assembled quantum dots. *Physical Review B,* 62, 16, 11083-7.

Reisfeld, R., Zusman, R., Cohen, Y., Eyal, M., (1988). The spectroscopic behaviour of Rhodamine 6G in polar and non-polar solvents and in thin glass and PMMA films. *Chemical Physics Letters,* 147, 142-7.

Resch, G., Held, A., Faber, T., Panzer, P., Toro, F., Reinhard, H., (2008). Potentials and prospects for renewable energies at global scale. *Energy Policy,* 36, 4048-56.

Richards, B.S., (2007). Performance enhancement and cost reduction potential of photovoltaic technologies via the application of luminescent materials. *Proceedings of Photovoltaic Science and Applications Technology 3*, Durham, UK, 5-8.

Richards, B.S., McIntosh, K.R., (2006). Ray-Tracing simulations of Luminescent Solar Concentrators Containing Multiple Luminescent Species. *Proceedings of 21st European Photovoltaic Solar Energy Conference*, Dresden, Germany, 185-8.

Richards, B.S., (2007). Performance enhancement and cost reduction potential of photovoltaic technologies via the application of luminescent materials.

Proceedings of Photovoltaic Science and Applications Technology 3, Durham, UK, 5-8.

Rowan, B.C., Wilson, L.R., Richards, B.S., (2008). Advanced material concepts for luminescent solar concentrators. *IEEE Journal of Selected Topics In Quantum Electronics,* 14, 5, 1312-22.

Sakuta, K., Sawata, S., Tanimoto, M., (1994). Luminescent concentrator module of a practical size. *Proceedings of 1st World Conference on Photovoltaic Energy Conversion*, Hawaii, USA, 1115-8.

Schüler, A., Kostro, A., Galande, C., Valle del Olmo, M., deChambrier, E., Huriet, B., (2007). Principles of Monte-Carlo ray-tracing simulations of quantum dot solar concentrators. *Proceedings of International Solar Energy Society World Solar Congress*, Beijing, China, 1033-7.

Sholin, V., Olson, J.D., Carter, S.A., (2007). Semiconducting polymers and quantum dots in luminescent solar concentrators for solar energy harvesting. *Journal of Applied Physics,* 101, 1231141-9.

Sidrach de Cardona, M., Carrascosa, M., Messeguer, F., Cusso, F., Jaque, F., (1985). Outdoor evaluation of luminescent solar concentrator prototypes. *Applied Optics,* 24, 13, 2028-32.

Slooff, L.H., Bende, E.E., Burgers, A.R., Budel, T., Pravettoni, M., Kenny, R.P., Dunlop, E.D., Büchtemann, A., (2008). A luminescent solar concentrator with 7.1% power conversion efficiency. *physica status solidi (RRL) - Rapid Research Letters,* 2, 6, 257-9.

Smestad, G.P., Hamill, P., (1984). Concentration of solar radiation by white backed photovoltaic panels. *Applied Optics,* 23, 4394–402.

Smestad, G.P., Ries, H., Winston, R., Yablonovitch, (1990). The thermodynamic limits of light concentrators. *Solar Energy Materials,* 21, 99-111.

Swartz, B.A., Cole, T., Zewail, A.H., (1977). Photon trapping and energy transfer in multiple-dye plastic matrices: an efficient solar-energy concentrator. *Optics Letters,* 1, 2, 73-5.

Uematsu, T., Yazawa, Y., Tsutsui, K., Miyamura, Y., Ohtsuka, H., T., W., Joge, T., (2001). Design and characterization of flat-plate static-concentrator photovoltaic modules. *Solar Energy Materials and Solar Cells,* 67, 441-8.

van Sark, W.G.J.H.M., Barnham, K.W.J., Slooff, L.H., Büchtemann, A., Meyer, A., McLafferty, J.B., Koole, R., Chatten, A.J., Farrell, D.J., Bose, R., Bende, E.E., Quilitz, J., Kennedy, M., Meyer, T., Wadman, S.H., Meijerink, A., Vanmaekelbergh, D., (2008). Luminescent Solar Concentrators - A review of recent results. *Optics Express,* 16, 26, 21773-92.

Weber, K.J., Everett, V., Deenapanray, P.N.K., Franklin, E., Blakers, A.W., (2006). Modeling of static concentrator modules incorporating lambertian or v-groove rear reflectors. *Solar Energy Materials and Solar Cells,* 90, 1741-9.

Winston, R., (1974). Principles of Solar Concentrators of a Novel Design. *Solar Energy,* 16, 89-95.

Winston, R., (1976). Dielectric Compound Parabolic Concentrators. *Applied Optics,* 15, 2, 291-2.

Wittwer, V., Stahl, W., Goetzberger, A., (1984). Fluorescent Planar Concentrators. *Solar Energy Materials,* 11, 187-97.

2 Ray-trace modelling of luminescent solar concentrators

2.0 Introduction

Modelling techniques enable LSC loss mechanisms to be quantified and optimised devices to be designed. The ray-trace modelling approach (Heidler *et al.*, 1982; Carrascosa *et al.*, 1983; Reisfeld *et al.*, 1988b; Gallagher *et al.*, 2004; Burgers *et al.*, 2005; Bose *et al.*, 2007; Kennedy *et al.*, 2007b; Richards and McIntosh, 2007; Schüler *et al.*, 2007) allows the multiple interdependent, competing LSC loss mechanisms to be accounted for, including losses arising from multiple re-absorption events. While commercial ray-trace packages are available, none can calculate absorption of traced rays by a luminescent species (at variable doping concentrations), nor trace rays emitted isotropically subsequent to an absorption event. Therefore, a Monte-Carlo ray-trace model was developed. Gallagher *et al.* (2004) previously developed a ray-trace model allowing the optical efficiency of rectangular QDSC devices to be quantified under varying input spectral irradiance. In the model, the plate is divided into a discrete number of zones and individual QD locations are assigned at random, in each zone, according to the specified QD doping level. Due to the computation time required for larger plate sizes the model was revised, removing the stored QD locations and introducing a background probability calculation to determine QD photon absorption events. This approach is not as computationally intensive, and allows more flexibility for device modelling, e.g. modelling of plates containing multiple luminescent species, matrix material light scattering approximation, and varying plate geometries of large sizes.

The main algorithms required to implement the model engine, i.e. ray reflection, refraction, absorption, emission, matrix material absorption and scattering, are outlined in section 0. Device concentration ratios are determined using the ray-trace model output and the attached photovoltaic (PV) cell spectral response curves. To validate the model, predictions are compared with a range of experimental measurements in section 2.2;

- Electrical output predictions are compared with measurements from fabricated QDSCs of varying *size*, *shape*, and *QD doping concentration.*
- Predicted spectral output for varying input *light position* on the QDSC top surface aperture is compared with observed spectra.
- Ray-trace predicted *loss mechanisms* (escape cone and external reflection losses) are compared with analytical predictions.
- Predicted *photon fluxes* emerging at each plate surface are compared with those of two other LSC models.

The validation tests show that the ray-trace approach provides an accurate tool for quantifying device loss mechanisms, and predicting QDSC output for any given set of material parameters. The model can be used to optimise device design in terms of geometry, luminescent species, matrix material, external reflector, and PV cell types.

2.1 Monte-Carlo ray-trace modelling

In the model, an incident photon, represented by a ray vector, is traced through the QDSC until it is lost from the system or transmitted to the PV cell. A Monte-Carlo method, described by the flow diagram in Figure 2.1, is used to determine the photon count optical efficiency (η_{opt}) and the output spectrum obtained at the PV cell, for a given monochromatic input light source at a random starting point on the top surface. Extensive MATLAB code was required to implement the model engine described in diagram in Figure 2.1.

At each branching point in the flow diagram, randomly generated numbers are tested against the respective calculated probabilities to determine whether the event ensues or not. A large number of rays of a given initial wavelength and angle are traced through the system from the same starting point, and the outcome of each ray is determined. This approach is then extended to model a non-monochromatic input light source incident on the entire QDSC top surface aperture. The algorithms behind each part of the model are described in detail in sections 2.1.1 to 2.1.6.

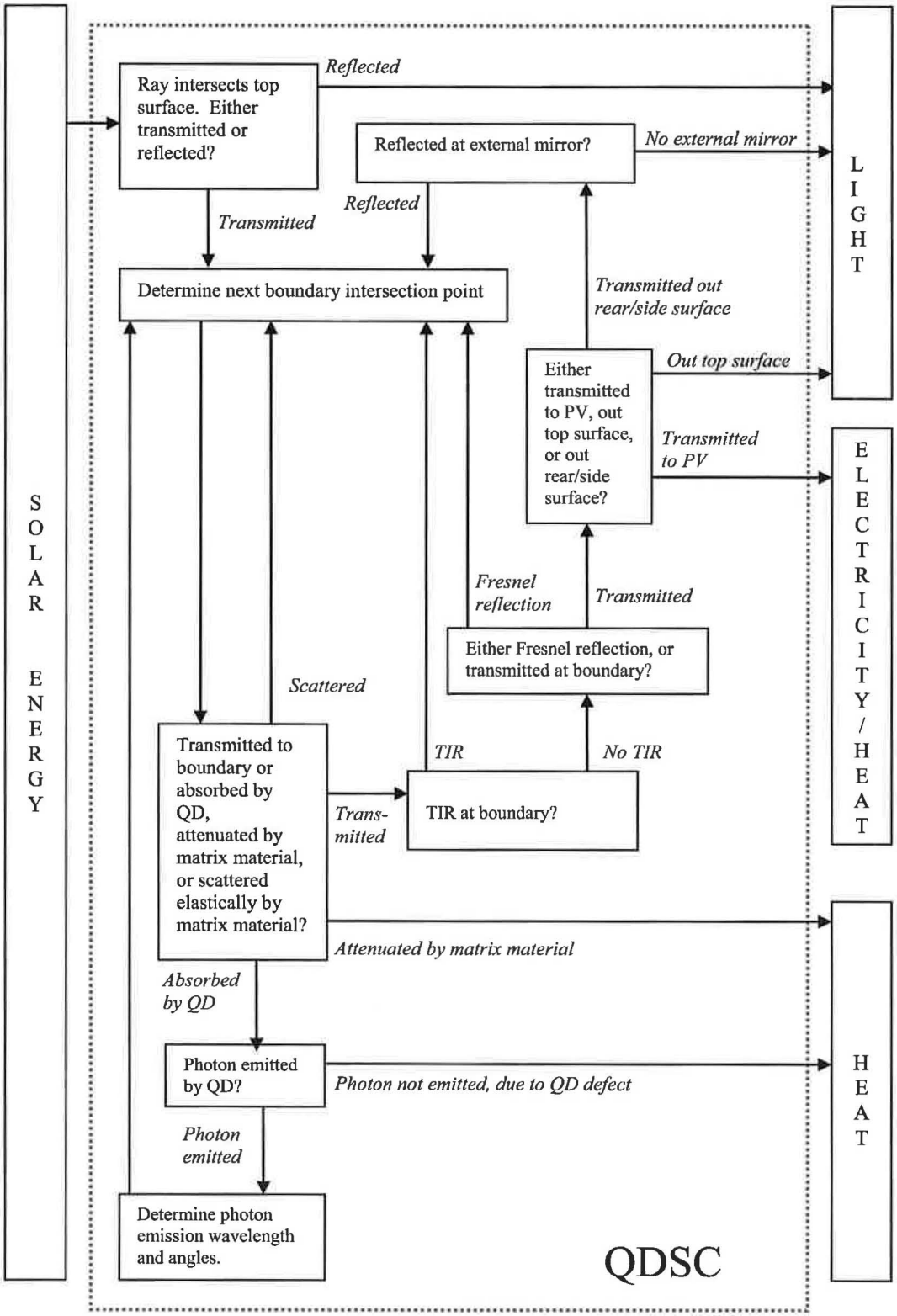

Figure 2.1. Ray-trace model flow diagram for ray incident on QDSC top surface.

2.1.1 Reflection and transmission at plate boundaries

To determine if an incident ray is reflected or transmitted at a boundary, consider;

Case A: $n_1 < n_2$, where n_1 and n_2 are the refractive indicies at the location of the incident and refracted ray, respectively. In this case the ray may be reflected or transmitted. The probability of reflection, R, is given by the Fresnel equations (Hecht, 2002);

$$R = \frac{R_\perp + R_\parallel}{2} \quad where, \quad R_\perp = \left(\frac{n_1 \cos\theta_1 - n_2 \cos\theta_2}{n_1 \cos\theta_1 + n_2 \cos\theta_2} \right)^2, R_\parallel = \left(\frac{n_1 \cos\theta_2 - n_2 \cos\theta_1}{n_1 \cos\theta_2 + n_2 \cos\theta_1} \right)^2 \qquad 2.1$$

Defining the incident ray as a normalised ray vector, $\boldsymbol{v}$, and the surface normal as a normalised vector, $\boldsymbol{p}$, the reflected ray vector is given by;

$$v_{reflect} = v - (2\cos\theta_1)p \qquad where, \quad \cos\theta_1 = v.p \qquad 2.2$$

If a ray is not reflected, then the transmitted refracted ray vector (Glassner, 1989) is given by;

$$v_{refract} = \left(\frac{n_1}{n_2} \right) v + \left(\cos\theta_2 - \frac{n_1}{n_2} \cos\theta_1 \right) p \quad where, \qquad 2.3$$

$$\cos\theta_2 = \sqrt{1 - \left(n_1 / n_2 \right)^2 (1 - (\cos\theta_1)^2)}$$

A Monte-Carlo technique is used to determine whether reflection or transmission ensues at the boundary intersection point. For example, a ray vector υ =

[0.785 0.453 -0.423] incident on a QDSC of refractive index 1.5 at $\theta_1 = 65°$, as shown in Figure 2.2, is considered. From eqn. 2.1, R is calculated at 0.1205. For each incident ray, a random number, k_r is then generated in the interval [0,1]. If $k_r <$ 0.1205, the ray is reflected. If $k_r > 0.1205$, the ray is transmitted into the plate. When the number of incident rays is increased, the number of rays reflected and transmitted tends to 12.05% and 87.95%, respectively.

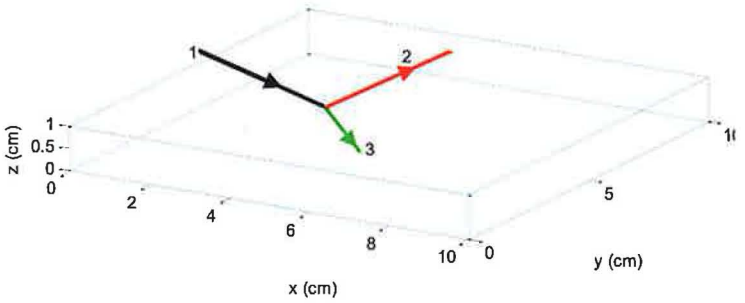

Figure 2.2. An incident photon may be either reflected (ray 2) or refracted (ray 3) depending on the calculated probability of reflection which is tested against a randomly generated number in the interval [0,1].

Case B: $n_1 > n_2$. The ray undergoes total internal reflection (TIR) if $\theta_1 > \theta_{critical}$. A TIR coefficient is defined by the user. If $\theta_1 < \theta_{critical}$, TIR does not occur, however the ray may still undergo Fresnel reflection at the boundary, with the probability determined by eqn. 2.1. The probability of reflection at external mirror surfaces is given by a user-defined mirror reflectivity (R_{mirror}).

2.1.2 Finding the intersection point of a ray and a plane

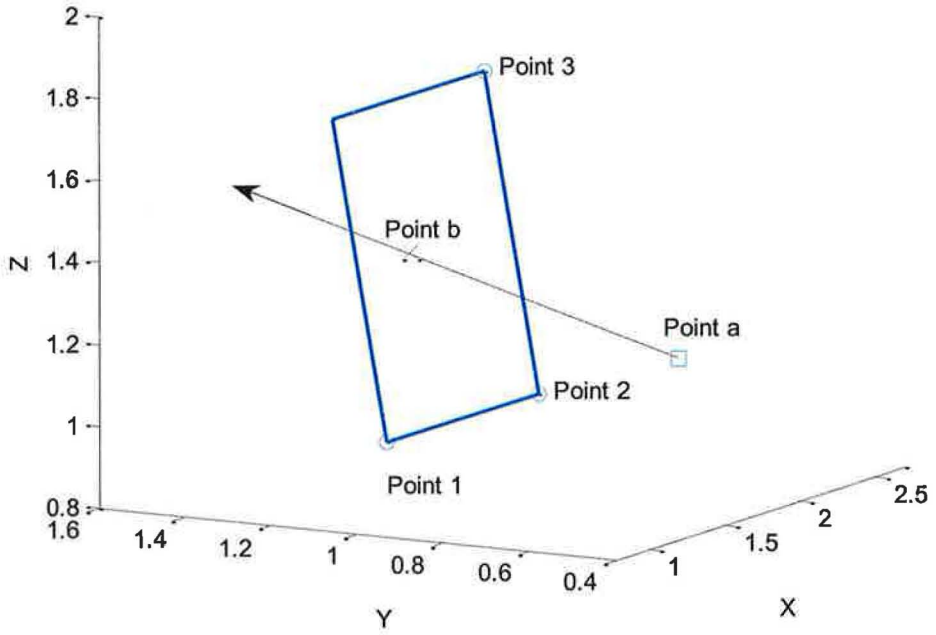

Figure 2.3. "Point b" is the intersection point of the ray vector, $\boldsymbol{v}$, and the plane defined by the three points, "Point 1", "Point 2", and "Point 3".

The equation of a plane defined by three co-planar points, "Point 1" = (x_1,y_1,z_1), "Point 2" = (x_2,y_2,z_2), and "Point 3" = (x_3,y_3,z_3), shown in Figure 2.3, is given by;

$$Ax+By+Cz+D=0 \qquad 2.4$$

where the determinants A, B, C and D are given by (Bourke, 1989);

$$A=\begin{vmatrix} 1 & y_1 & z_1 \\ 1 & y_2 & z_2 \\ 1 & y_3 & z_3 \end{vmatrix} \quad B=\begin{vmatrix} x_1 & 1 & z_1 \\ x_2 & 1 & z_2 \\ x_3 & 1 & z_3 \end{vmatrix} \quad C=\begin{vmatrix} x_1 & y_1 & 1 \\ x_2 & y_2 & 1 \\ x_3 & y_3 & 1 \end{vmatrix} \quad D=-\begin{vmatrix} x_1 & y_1 & z_1 \\ x_2 & y_2 & z_2 \\ x_3 & y_3 & z_3 \end{vmatrix} \qquad 2.5$$

or

$$
\begin{aligned}
A &= y_1(z_2 - z_3) + y_2(z_3 - z_1) + y_3(z_1 - z_2) \\
B &= z_1(x_2 - x_3) + z_2(x_3 - x_1) + z_3(x_1 - x_2) \\
C &= x_1(y_2 - y_3) + x_2(y_3 - y_1) + x_3(y_1 - y_2) \\
D &= -\left(x_1(y_2 z_3 - y_3 z_2) + x_2(y_3 z_1 - y_1 z_3) + x_3(y_1 z_2 - y_2 z_1) \right)
\end{aligned}
\qquad 2.6
$$

A ray travelling from "Point a" (x_a, y_a, z_a) is defined by the direction ray vector, $\upsilon = [x_\upsilon \; y_\upsilon \; z_\upsilon]$. The intersection point of the ray with the plane, i.e. "Point b", is given by;

$$
\text{"Point b"} = (x_b, y_b, z_b) = (x_a, y_a, z_a) + u(v) \qquad 2.7
$$

Substituting into 2.4 gives;

$$
A(x_a + ux_v) + B(y_a + uy_v) + C(z_a + uz_v) + D = 0 \qquad 2.8
$$

or

$$
u = -\frac{Ax_a + By_a + Cz_a + D}{Ax_\upsilon + By_\upsilon + Cz_\upsilon} \qquad 2.9
$$

2.1.3 Determining boundary intersection points

Each surface of the QDSC is represented by a plane defined by three of the four corner points. A set of intersection points of the ray vector, υ, with each surface of the QDSC is determined using eqn. 2.7. The actual intersection point is then determined from the set of all intersection points by eliminating those points that are (i) outside the boundaries of the respective plane or (ii) in the opposite direction of the ray.

2.1.4 QD photon absorption and emission

To determine if a ray is absorbed by a QD, the QD absorption coefficient, α_{QD}, for the particular ray wavelength, λ, is obtained from the measured QD absorption spectrum. The total probability of an absorption event occurring between boundary intersection points, separated by distance, *d*, is determined from;

$$P_{abs} = 1 - e^{-\alpha_{QD} d} \qquad 2.10$$

If a ray is absorbed by a QD, the probability of photon emission is given by the QD QY. The emission wavelength, λ_{em}, is assigned at random from a weighted distribution corresponding to the measured emission profile of a low QD concentration sample (Kennedy *et al.*, 2007b). Figure 2.4 shows a series of measured emission spectra of a sample of CdSe/ZnS core-shell QDs, for varying excitation wavelengths. The ray-trace model can utilise a series of QD photon emission spectra, as proposed by Schüler et al., (2007), where the particular emission spectrum used is selected depending on the wavelength of the absorbed ray, λ.

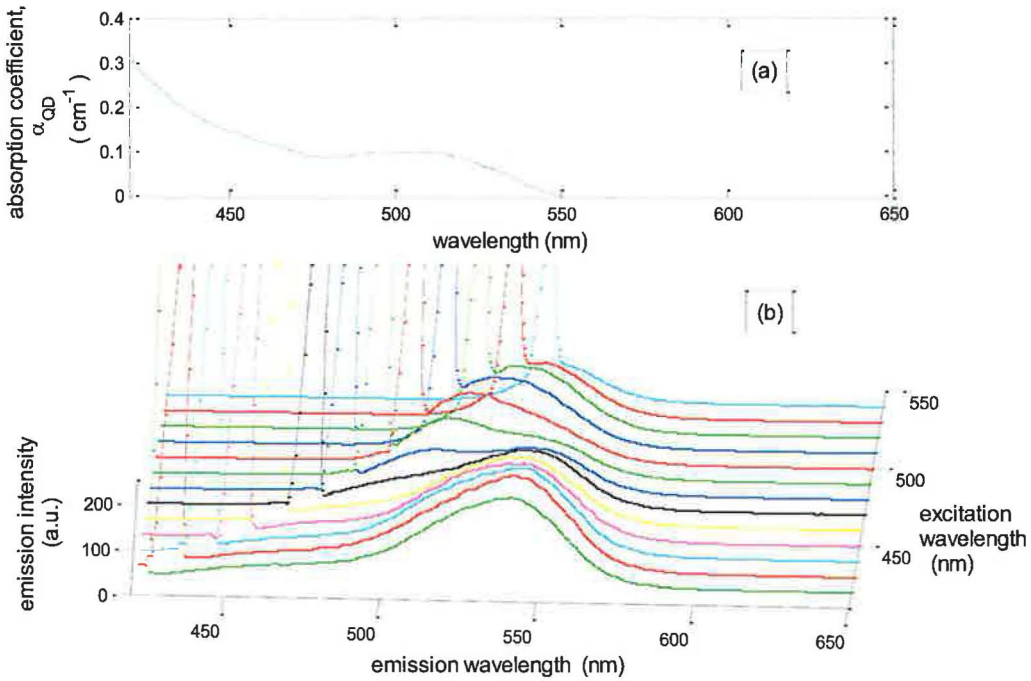

Figure 2.4 (a) Absorption spectrum of CdSe/ZnS core-shell QDs (Evident Technologies) measured with a Perkin Elmer 900 UV/Vis/NIR spectrometer. (b) Emission spectra using range of excitation wavelengths measured with a Perkin Elmer LS55B spectrometer. The excitation line is seen as the sharp spike in each spectrum at the respective excitation wavelength.

2.1.5 Matrix material absorption and scattering

In current low efficiency QDSC devices, where the optical efficiency < 1%, a significant fraction of light reaching the PV cell is due solely to scattering caused by the polymer matrix material[iv]. Scattering events are included in the model to enable comparison of predictions with experimental measurements. A scattering spectrum for the epoxy matrix material was measured by Gallagher *et al.*, (2007). The total attenuation loss (i.e. Fresnel reflection, matrix material absorption and scattering losses) of the epoxy sample was measured using a Perkin Elmer 900 UV/Vis/NIR

[iv] The optical efficiency, η_{opt}, of the fabricated QDSC devices in sections 2.2.2 - 2.2.4 is of the same order as that of a polymer plate un-seeded with QDs

spectrometer in the setup configuration illustrated in Figure 2.5(a). By locating the epoxy sample at the entry aperture to an integrating sphere within the spectrometer, as illustrated in Figure 2.5(b), scattered light is collected by the detector, thereby removing scattering losses from the measured "attenuation". The difference between the spectra using the respective setups in (a) and (b) yields a scattering spectrum approximation for the epoxy material (Gallagher et al., 2007). The matrix scattering and absorption spectra are shown in Figure 2.6, from which the matrix material absorption coefficient, α_{mat}, and scattering coefficient, α_{scat}, for a particular λ are obtained. The scattering coefficient is inversely proportional to wavelength, indicating that scattering process is Rayleigh scattering which is proportional to λ^{-4}.

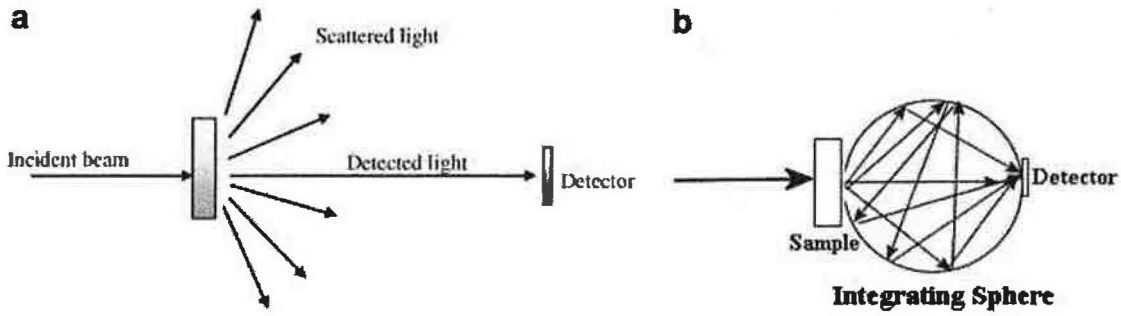

Figure 2.5. Experimental set up for absorbance measurements using a Perkin Elmer Lambda 900 UV/VIS/NIR Spectrometer; (a) normal set up; (b) using an integrating sphere to account for scattering in the samples (Gallagher *et al.*, 2007).

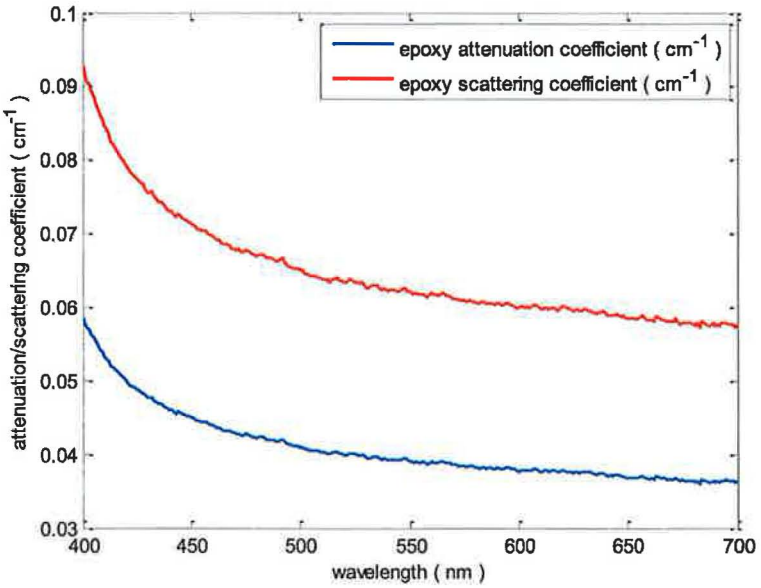

Figure 2.6. Measured absorption and scattering spectra of an epoxy matrix material sample (Gallagher *et al.*, 2007).

The total probability that a ray will undergo either an absorption (by QD), a matrix material absorption or a scattering event between boundary intersection points is given by;

$$P_{total} = 1 - e^{-(\alpha_{QD} + \alpha_{mat} + \alpha_{scat})} \qquad 2.11$$

A randomly generated number, in the interval [0,1], is tested against P_{total} to determine if any event occurs between boundary intersection points. Assuming an event occurs, the ratio of the relative individual event probabilities over the distance, d, i.e.,

$$1 - e^{-(\alpha_{QD} d)} : 1 - e^{-(\alpha_{mat} d)} : 1 - e^{-(\alpha_{scat} d)} \qquad 2.12$$

is then used to determine which particular event ensues. A ray deemed to be attenuated by the matrix material is lost (as heat in the matrix). Scattering is assumed to be elastic, and predominantly in a forward direction, based on scattering measurements carried out by Thomas *et al.*, (1983) on a PMMA LSC plate. The weighted forward scattering angle distribution used is given in Figure 2.7(a). An illustration of 10,000 rays scattered at angles selected from this distribution is shown in Figure 2.7(b).

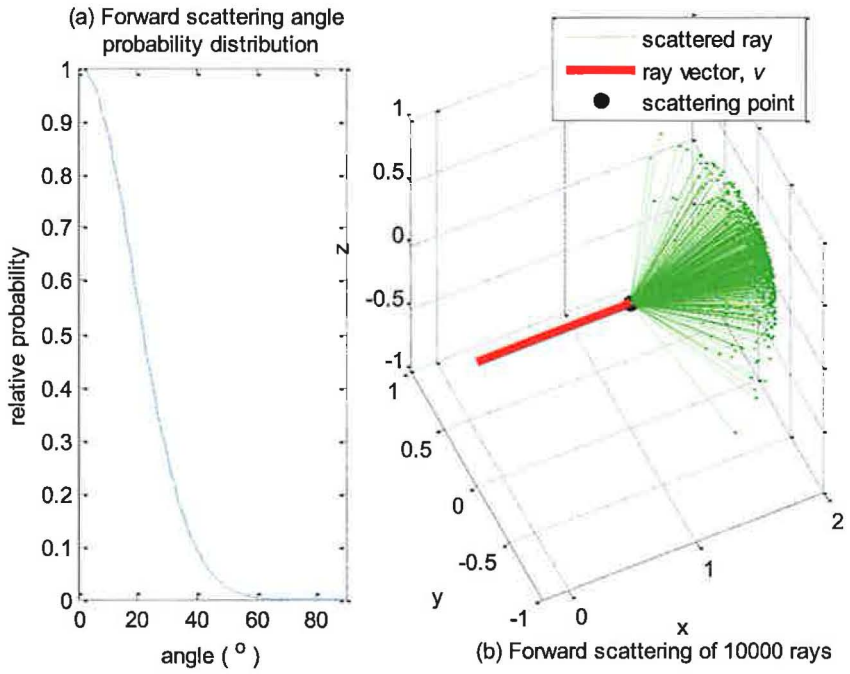

Figure 2.7. (a) The weighted forward scattering probability distribution used in the model (b). An example plot of 10,000 rays scattered at angles selected at random from a weighted distribution corresponding to (a).

A ray deemed not to be absorbed by a QD, nor attenuated or scattered by the matrix material is transmitted to the next intersection point where reflection/transmission ensues, as detailed in section 2.1.1.

2.1.6 Concentration ratio and photovoltaic cell spectral response

The optical efficiency, η_{opt}, is defined as the total number of photons that are transmitted to the PV cell relative to the total incident on the top surface aperture;

$$\eta_{opt} = \frac{\int N_{out}(\lambda)\, d\lambda}{\int N_{in}(\lambda)\, d\lambda} \qquad 2.13$$

where, N_{in} and N_{out} are the input and output photon distributions, respectively. The geometric gain, G_{geom}, is defined as the ratio between the top surface aperture area and PV cell area. The photon concentration ratio, C_{ph}, is calculated as the product of η_{opt} and G_{geom};

$$C_{ph} = \eta_{opt} G_{geom} \qquad 2.14$$

The overall spectrally-specific concentration ratio (C) is given by;

$$C = \frac{\int N_{out}(\lambda)\eta_{EQE}(\lambda)\, d\lambda}{\int N_{in}(\lambda)\eta_{EQE}(\lambda)\, d\lambda} G_{geom} \qquad 2.15$$

where η_{EQE} is the measured cell external quantum efficiency, and the terms are integrated over the spectral response range of the attached PV cell. In the ray-trace model, the input spectral energy distribution, $E_{in}(\lambda)$, is converted to a photon distribution, $N_{in}(\lambda)$, using the relationship;

$$N_{in} = E_{in}\left(\frac{\lambda}{hc}\right) \qquad 2.16$$

The PV cell η_{EQE} is given by;

$$\eta_{EQE} = \eta_{IQE}(\lambda)\ (1\text{-}R_{pv}(\lambda)) \qquad 2.17$$

where R_{pv} and η_{IQE} are the measured PV cell reflectivity, and internal quantum efficiency, respectively. η_{EQE}, η_{IQE} and R_{pv} curves for a mc-Si cell are shown in Figure 2.8(a) (van Sark, 2008).

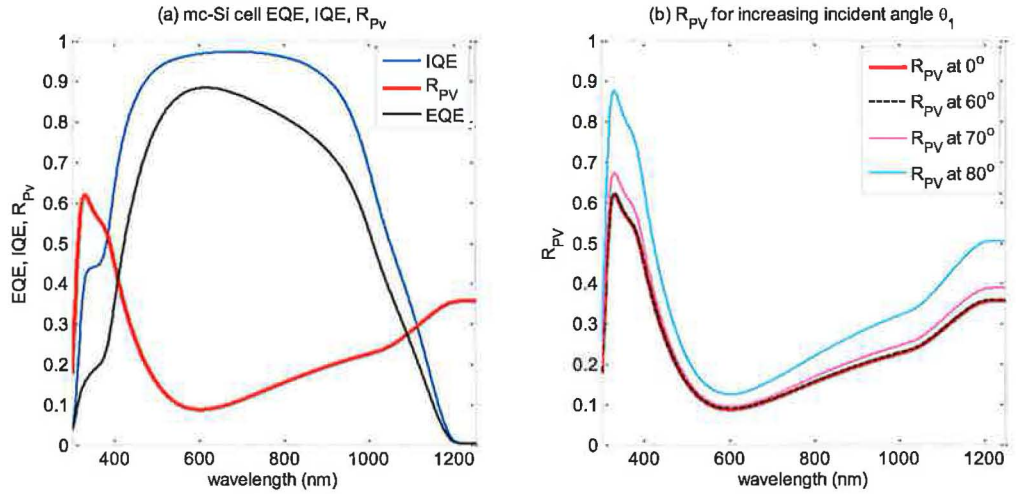

Figure 2.8. (a) Measured EQE, IQE and reflectivity (R_{pv}) at normal incidence of a mc-Si cell. (b) Extrapolated R_{pv} curves for higher angles of incidence.

Using eqn. 2.1 a set of angle dependent PV reflectivity curves, R_{pv} (θ,λ) shown in Figure 2.8(b), are approximated from R_{pv}. PV cell IQE may also vary with incident angle due to the increase in pathlength through the cell. This is not accounted for by the model. However, as IQE is close to unity at typical QD emission wavelengths, variations in IQE with incidence angle will introduce only limited errors in predicted

PV cell short circuit current. The QDSC concentration ratio, incorporating angle-dependent PV reflectivity can thus be calculated from;

$$C = \frac{\int N_{out}(\lambda)\ \eta_{IQE}(\lambda)\ (1\text{-}R_{pv}(\theta,\lambda))\ \mathrm{d}\lambda}{\int N_{in}(\lambda)\ \eta_{IQE}(\lambda)\ (1\text{-}R_{pv}(\theta,\lambda))\ \mathrm{d}\lambda} G_{geom} = \frac{I_{sc,PV_C}}{I_{sc,PV}} \qquad 2.18$$

QDSC concentration ratio is defined as the ratio of the short circuit current of the PV cells attached to the concentrator, I_{sc,PV_C}, to the short circuit current of the same PV cells not attached to the concentrator, $I_{sc,PV}$, oriented on the same plane as the concentrator top surface.

2.2 Model Validation

At the initial model development stage, it was found useful to plot traced rays as they propagate through non-attenuating plates, un-seeded with QDs. This provided a visual check that the geometric ray-trace algorithms had been implemented correctly. Ray-trace predicted escape cone and external reflection losses are compared with analytical predictions (calculated for simplified, idealized QDSCs), providing a further check of the geometric ray-trace algorithms.

Incorporating QD photon absorption and emission, and matrix material absorption and scattering, the model predictions are compared with measured electrical output from fabricated QDSCs of varying *size*, *shape* and QD *doping concentration*. Predicted and measured efficiencies are found to match for all QDSCs. Measured QDSC edge emission spectra show a variation in peak

wavelength and intensity, depending on the distance between the detector (at the plate edge) and the input laser spot position on the top surface aperture. The predicted peak wavelengths and relative intensities exhibit the same trend as the measured data. The validation checks indicate that QD absorption and emission, re-absorption of QD emitted photons, and transport losses within the plate are calculated accurately in the model.

Model predictions also match with measured electrical output from four LSC plates of varying plate dimensions, containing Coumarin luminescent dyes, which were fabricated by Chatten *et al.*, (2005). Predictions are compared with those from two other LSC models. A high level of agreement exists between all three models, with < 1% absolute difference in the predicted photon flux magnitude emerging at each plate surface.

2.2.1 Visualization of traced rays

To check that the *geometric* ray-trace algorithms, i.e. the boundary intersection point and reflection/transmission algorithms, are implemented correctly, it is useful to plot the traced rays. Assuming α_{mat} and α_{scat} to be zero and perfectly reflecting external mirrors at all surfaces, a ray is given a random initial angle and is traced inside a hexagonal QDSC until it has intersected a boundary a given number of times. The trace, plotted in Figure 2.9, provides a visual check that the geometric ray trace algorithms are operating correctly.

Figure 2.10 shows 25 rays incident at different angles on one surface of a triangular QDSC, assuming a plate refractive index of 1.5 and no external mirrors at any surface. It can be observed that if $\theta_1 > \theta_{critical}$, TIR ensues correctly. In this

example, all rays with $\theta_1 < \theta_{critical}$ are transmitted out of the device, except a single ray which was deemed by the Monte-Carlo method employed to undergo Fresnel reflection at the boundary. A more quantitative validation check of reflection/transmission algorithms is given in section 2.2.6.

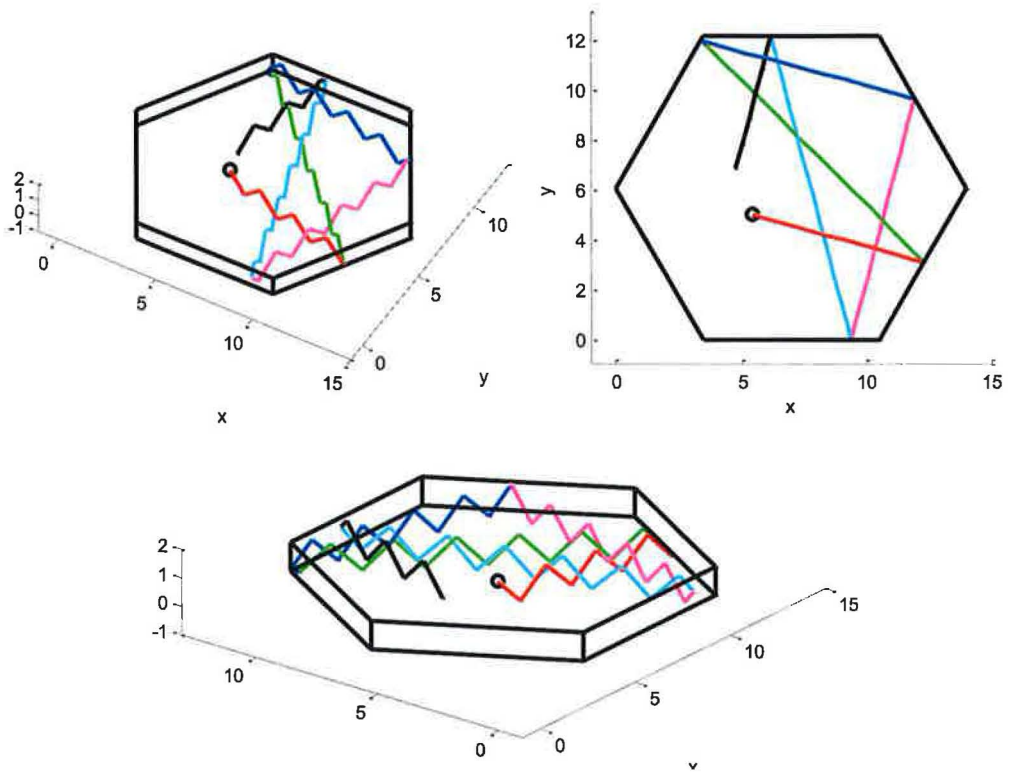

Figure 2.9. A ray given a random initial angle is traced inside a non-attenuating hexagonal QDSC, assuming perfectly reflecting external mirrors at all surfaces.

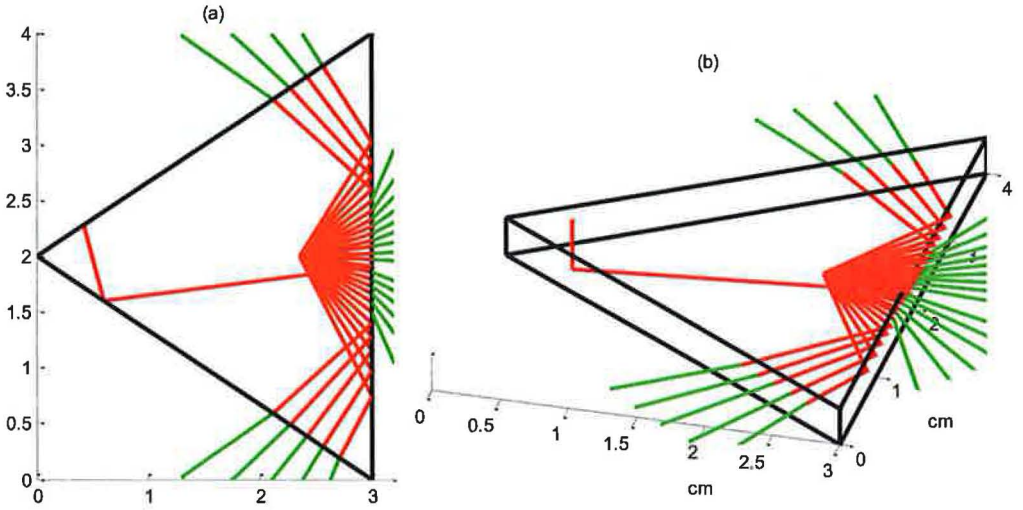

Figure 2.10. Rays are traced inside a non-attenuating triangular QDSC, assuming a plate refractive index of 1.5 and no external mirrors at any surface. If $\theta_1 > \theta_{critical}$, TIR ensues. In this example, all rays with $\theta_1 < \theta_{critical}$ are transmitted out of the device, except a single ray which undergoes Fresnel reflection at the boundary.

2.2.2 Edge emission spectra for varying input light position

Objective

The red-shift in measured edge emission spectra for varying input laser positions on the top surface aperture are compared with model predictions of the red-shift, testing whether the model accurately determines re-absorption effects and transport losses in QDSCs.

Experimental

A QDSC containing 'OMN28' QDs (CdSe/ZnS core-shell, emission wavelength 550 nm, Nanoco Technologies) was fabricated by Rowan *et al.* (2007). Using a 457 nm argon-ion laser input light source, the edge emission spectrum of the QDSC was measured using seven different input laser positions on the top surface

aperture at increasing distances from the detector. The experimental setup is illustrated in Figure 2.11. The relative intensity of the edge emission spectra should decrease for input laser spot positions further from the edge where detector is positioned, due to higher material absorption and re-absorption losses. Moreover, the edge emission spectra for input laser spot positions further from the detector should be more red-shifted, due to re-absorption of QD emitted photons (Batchelder *et al.*, 1979; Chatten *et al.*, 2004).

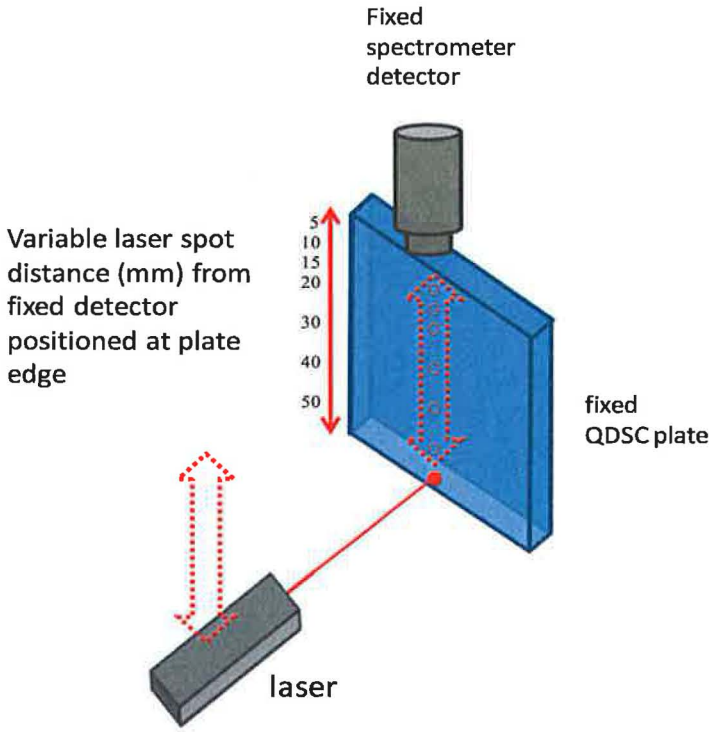

Figure 2.11. Measurement of QDSC edge emission spectrum, using different input laser positions on the QDSC surface, at varying distances (5mm - 50mm) from the plate edge at which the spectrometer detector is positioned.

Results

Figure 2.12 shows the measured edge emission spectra for a QDSC containing a 0.05% mass/volume 'OMN 28' QD concentration (Kennedy *et al.*, 2007b). The measured peak at ~556 nm for the "5mm" input position is matched

closely by the predicted peak, shown in Figure 2.13. The expected red-shifting of the edge emission peaks for input laser positions further from the detector is observed, matched to a large degree by the red-shifting of the predicted spectra. The measured and predicted edge emission peak wavelengths, for each input laser position, are shown in Figure 2.14(a). The relative integrated edge emission intensities for varying input laser positions are shown in Figure 2.14(b). The close match indicates that QDSC transport losses and re-absorption are calculated accurately in the ray-trace model. There is some divergence in predicted and measured emission peaks. One possible cause of the divergence is the uncertainty in actual matrix material absorption and scattering. Absorption and scattering spectra of the epoxy matrix material used in QDSCs can vary from sample to sample due to fabrication inhomogeneities (e.g. time taken for curing which is dependent on plate dimensions, or the mixing procedure used which can create small air-bubbles in the sample). The epoxy attenuation spectra shown in Figure 2.6 may differ from the actual spectra of the fabricated QDSC. In particular, a higher degree of scattering in the fabricated QDSC would result in higher attenuation losses at shorter wavelengths, resulting in an apparent redshift in the measured spectra. The total divergence in peak emission wavelength is < 4 nm. This will not introduce significant errors in predicted electrical output of a PV cell, as the cell spectral response *variation* is small over this wavelength range.

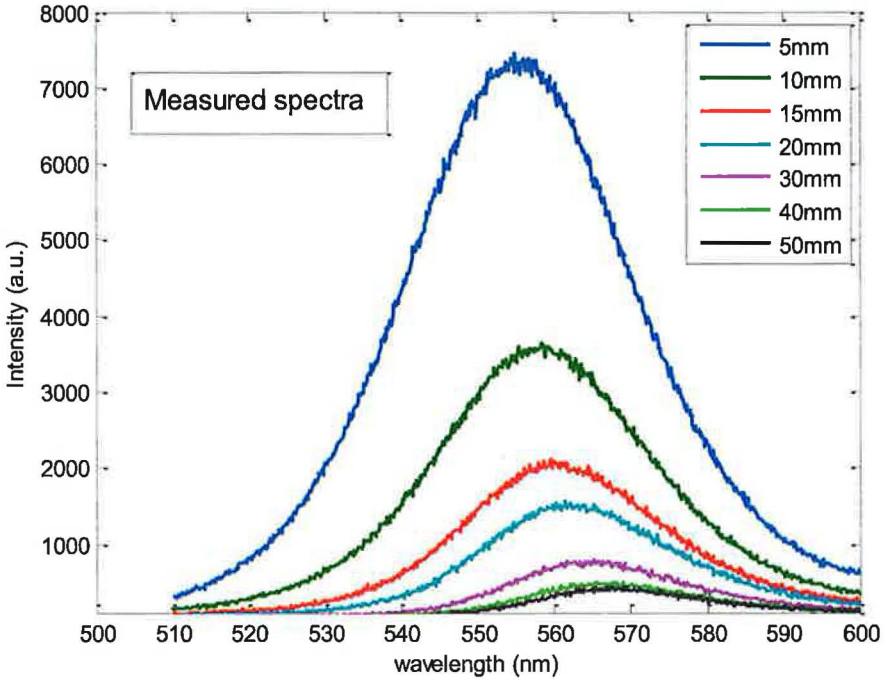

Figure 2.12. Measured edge emission spectra for a laser (457nm) input at seven different distances (increasing from 5mm to 50 mm) from the detector.

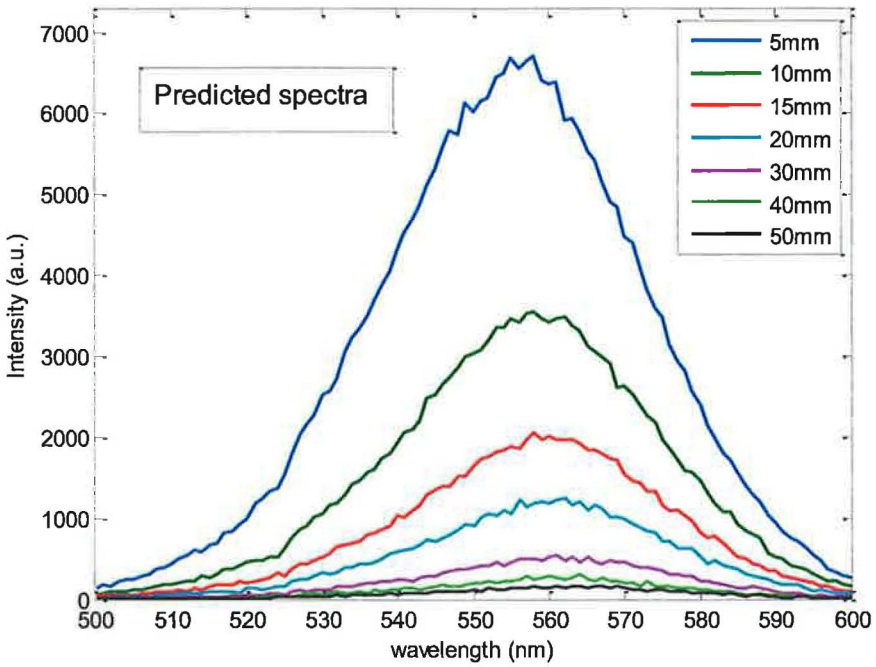

Figure 2.13. Predicted edge emission spectra for a laser (457nm) input at seven different distances (increasing from 5mm to 50 mm) from the detector.

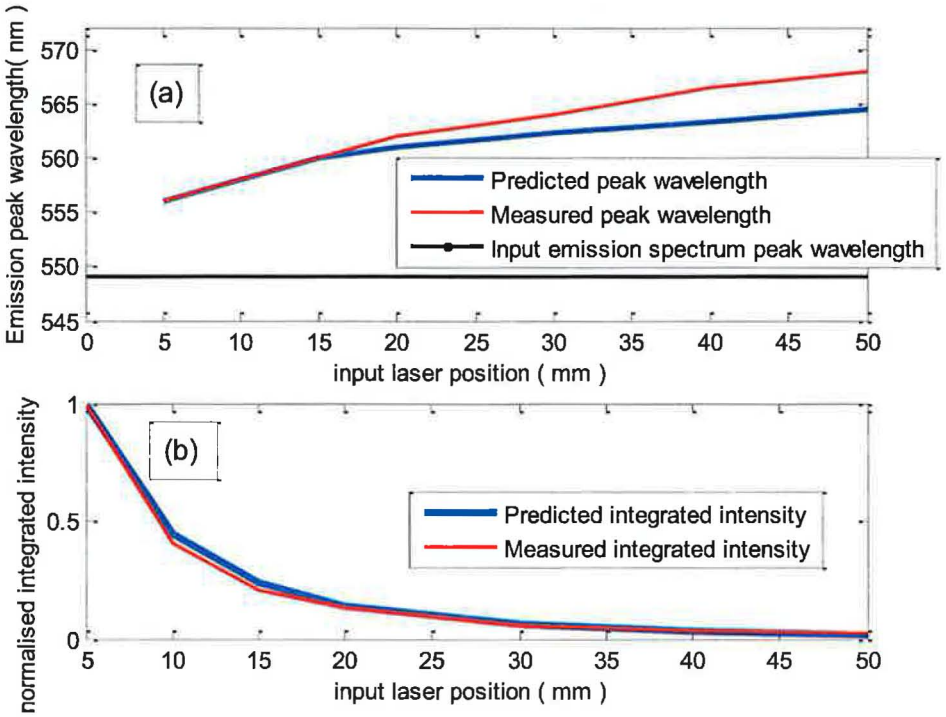

Figure 2.14. (a) compares the *peak wavelengths* and (b) compares the *relative integrated intensities* of the measured and predicted edge emission spectra, shown in Figure 2.12 and Figure 2.13, respectively.

2.2.3 QDSC optical efficiency with varying QD concentration

Objective

Increasing the QD doping concentration results in higher absorption efficiency (η_{abs}). However, re-absorption of QD emitted photons also increases with higher concentrations, implying a maximum η_{opt} should occur at a particular optimum QD concentration. A matching predicted and measured trend in η_{opt} with varying QD concentration will indicate that QD photon absorption and re-absorption is calculated accurately in the ray-trace model.

Experimental

Six QDSC devices with increasing QD concentrations of '488C' QDs (CdSe/ZnS core-shell, emission wavelength 488nm, Nanoco Technologies) were fabricated by Rowan *et al.* (2007). Figure 2.15 shows the absorption and emission spectra of the six QDSCs containing different QD concentrations (% mass/volume). A solely epoxy device, un-seeded with QDs, was also fabricated. Filtered light from a metal halide lamp, with the spectrum shown in Figure 2.15, was used as the incident light source. The short circuit current of a monocrystalline PV cell was used to measure the light intensity emerging at the QDSC edge. The same PV cell was employed to measure the light intensity incident on the top surface entry aperture area of the QDSCs.

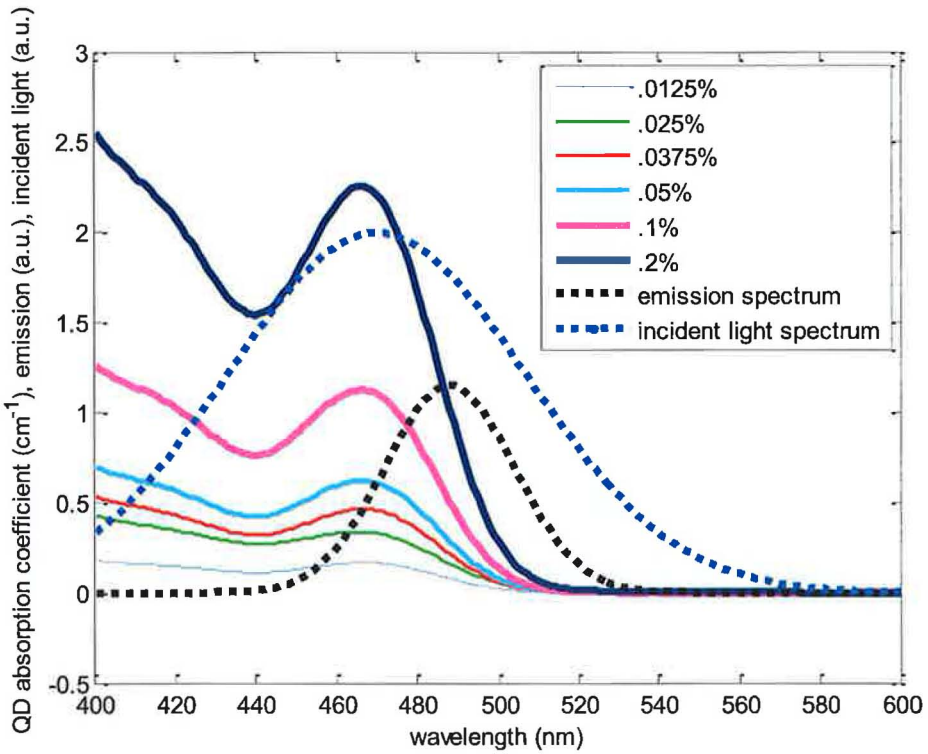

Figure 2.15. Measured absorption and emission spectra of six samples containing different concentrations of '488C' CdSe/ZnS QDs.

Results

Predicted η_{opt}, using a range of QD QYs, for each QDSC are shown in Figure 2.16 (Kennedy *et al.*, 2007b). A QY of ~10% results in a match with the measured η_{opt} values. The optical efficiency of the six QDSCs is of the same order as the solely epoxy device, indicating that light reaches the PV cell predominantly through scattering in all six devices. Model predictions are in agreement with the observed trend, in that no significant increase in η_{opt} with QD concentration was observed. This indicates that QD photon absorption and re-absorption are calculated accurately in the ray-trace model for devices with varying QD doping concentration.

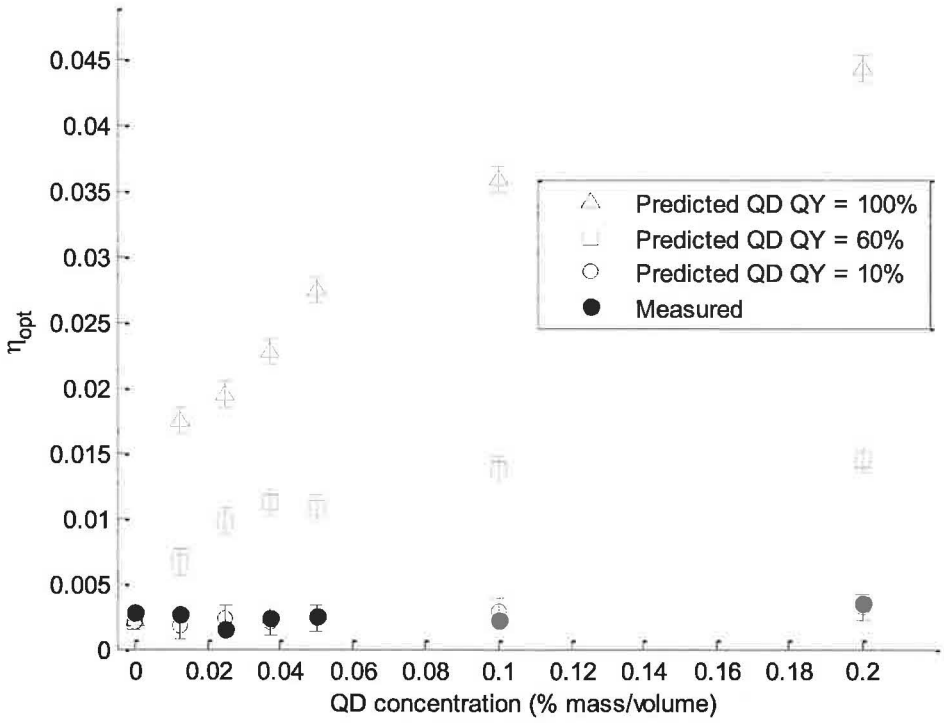

Figure 2.16. Measured and predicted optical efficiencies (η_{opt}) of fabricated devices containing different concentrations of QDs. The predicted η_{opt} values are calculated using a QD QY of 10%, 60% and 100%. The error bars on the predicted values indicate the η_{opt} uncertainty due to inhomogeneous matrix material scattering in different plates.

Predicted errors

A single scattering spectrum (shown in Figure 2.6), representative of the epoxy matrix material, is used to model all QDSC samples. The magnitude of scattering in individual QDSCs varies from sample to sample, and therefore the model will under- or overestimate η_{opt}. The predicted error bars indicate the uncertainty in η_{opt} which arises from this non-homogeneous matrix material scattering. Uncertainty in the other model input parameters, detailed in section 2.3, is not considered as the error introduced to the *relative* η_{opt} (in these particular plates which have very low η_{opt}) is much less than the error introduced by scattering uncertainty.

2.2.4 QDSC optical efficiency with varying size and shape

Objective

Optical efficiency decreases with larger concentrator size due to increased total re-absorption losses, matrix material losses and side reflection losses. Measured optical efficiencies of four rectangular QDSCs of varying size are compared with model predictions. Varying the QDSC shape alters the mean number of reflections from side surfaces. Measured optical efficiencies of triangular and circular QDSCs are compared with model predictions. Matched observations and predictions will indicate that transport losses, i.e. matrix material losses, side reflection losses and QD re-absorption losses, are determined accurately in the ray-trace model for devices of varying size and shape.

Experimental

Nine QDSCs of varying geometries containing 'Fort Orange' (CdSe/ZnS core-shell, emission wavelength 605 nm, Nanoco Technologies) QDs were fabricated by Rowan *et al.* (2007). The dimensions of each plate are given in Table 2.1. Each plate has a thickness of 0.3 cm. The incident light spectrum used and the QD absorption and emission spectra are shown in Figure 2.17.

Shape	Photo	Dimensions (cm)	Aperture Area (cm^2)	G_{gain}
r1		2 x 4.0	8.0	6.66
r2		2.8 x 4.0	11.2	9.33
r3		3.5 x 4.0	14.0	11.7
r4		3.6 x 4.0	14.4	12.0
t1		Base: 4.0 Length: 1.9	3.8	3.33
t2		Base: 4.0 Length: 3.1	6.2	4.66
c1		Radius: 2.0	6.28	5.23
c2		Radius: 3.0	26.2	21.8
c3		Radius:4.0	48.8	40.7

Table 2.1. Dimensions and geometric gain (G_{geom}) of nine QDSCs of varying shape and size (Rowan *et al.*, 2007).

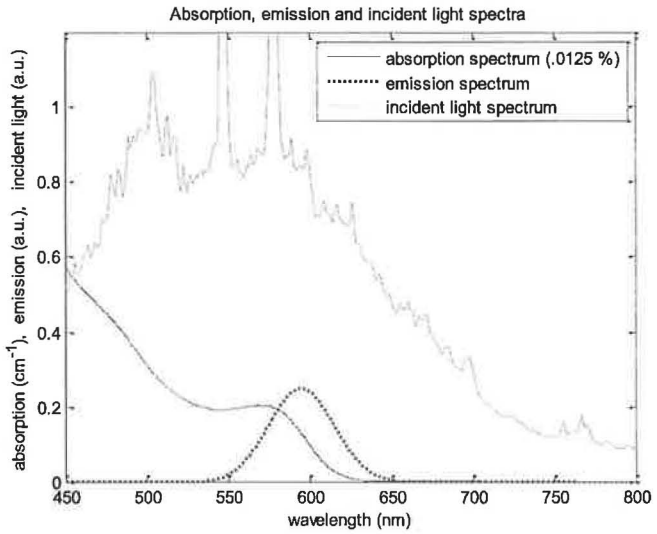

Figure 2.17. Absorption and emission spectra of 'Fort Orange' QDs. Incident light spectrum from metal halide lamp.

Results

The predicted QDSC η_{opt}, using a QD QY of 14%, given in Figure 2.18, show good agreement with measured values. The predicted error bars indicate the uncertainty due to inhomogeneous matrix material scattering. The smallest plates of each geometry type are the most efficient. The decrease in predicted η_{opt} for larger plate sizes, matches the decrease in measured η_{opt}, indicating that transport losses are calculated accurately in the model, for QDSCs of varying *size*. A validation of the effect of QDSC *shape*, however, would require a range of many rectangular, circular and triangular plates with equal G_{geom}, whereas in these fabricated plates G_{geom} of each geometry type are in different ranges.

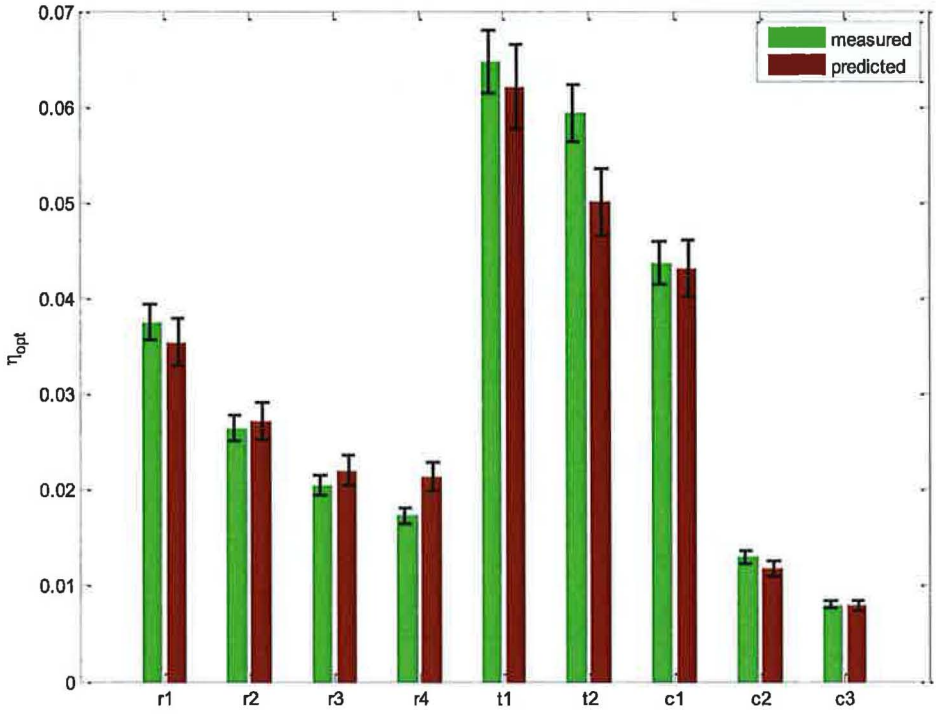

Figure 2.18. Predicted and measured optical efficiencies from four rectangular (r1 – r4), two triangular (t1,t2) and three circular (c1 – c3) QDSCs of varying size as given Table 2.1.

2.2.5 Multiple dye liquid LSCs

Objective

The addition of multiple dyes in an LSC allows the absorption of the solar spectrum to be enhanced compared to a single dye LSC (Burgers *et al.*, 2006; Richards and McIntosh, 2006; Bailey *et al.*, 2007). However, as there may be a large degree of overlap between different dyes' absorption and emission spectra, re-absorption losses may increase significantly in a multiple dye LSC. Predictions of multiple dye LSCs are compared with measurements, to verify whether absorption and re-absorption effects in LSCs containing multiple luminescent species are calculated accurately by the ray-trace model.

Experimental

A 10 x 4 x 0.5 cm quartz cuvette was used as a liquid LSC container, as shown in Figure 2.19. A 2.0 x 0.3 cm silicon cell was placed adjacent to one side of the cuvette at a right angle to the incident beam. Three Perylene dyes (BASF Lumogen Yellow 170, Lumogen Orange 240 and Lumogen Red 305) of varying concentrations, given in Table 2.2, were prepared in chloroform solution. The absorption and emission spectra of each dye, along with the spectrum of the metal halide incident light source, are shown in Figure 2.20. Four multiple dye mixes, listed in Table 2.2, were prepared. The different dye solutions were placed into the LSC container and the resulting PV cell short circuit current density, J_{sc}, measured (Kennedy *et al.*, 2008b).

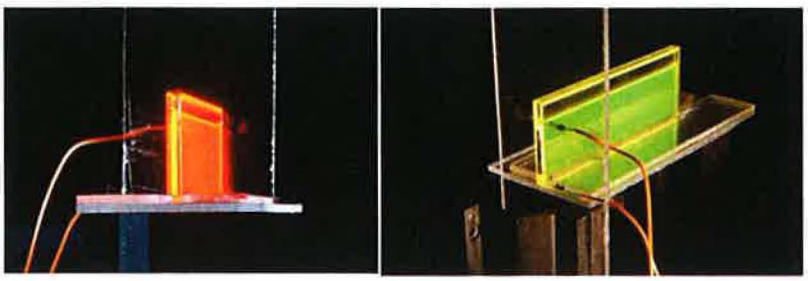

Figure 2.19. A liquid LSC is pictured containing a Lumogen Orange 240 sample (left) and Lumogen Yellow 170 sample (right). A silicon PV cell is placed adjacent to one side of the liquid LSC, at right angles to the incident beam.

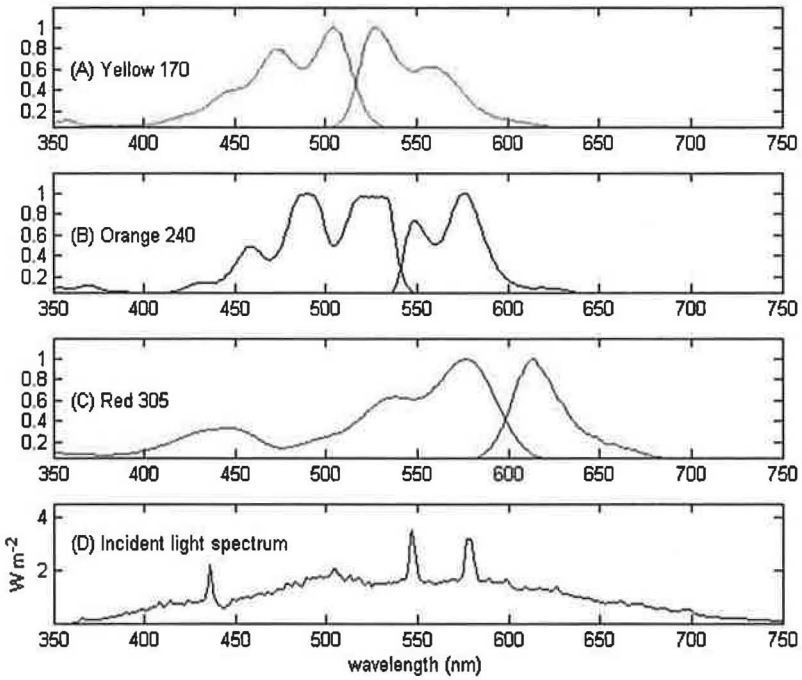

Figure 2.20. Normalised absorption and emission spectra of (A) Lumogen Yellow 170, (B) Lumogen Orange 240 and (C) Lumogen Red 305. The shorter wavelength emitting dye(s) overlap significantly with the longer wavelength absorbing dye(s), resulting in a large degree of re-absorption in the LSC containing multiple dyes. The spectrum of the incident light is shown in (D).

			Abbreviation	Concentration $x10^{-2}$ (mg/ml)
Dye	Single dye	Yellow 170	Y1	3
			Y2	6
			Y3	12
			Y4	25
		Orange 240	O1	5
			O2	10
			O3	20
			O4	40
		Red 305	R1	2
			R2	5
			R3	10
			R4	20
	Dye Mix	R4+O4	Mix 1	60
		R4+O4+Y4	Mix 2	85
		R2+O2+Y2	Mix 3	21
		Y2+O2	Mix 4	16

Table 2.2. Luminescent dyes of varying concentrations and the dye mixes used in liquid LSC tests.

Results

Absolute short circuit current densities (J_{sc}) predicted by the ray-trace model were, on average, ~30% higher than measured J_{sc} for each dye sample. One surface wall of the quartz cell (10 x 0.5 cm surface) had a frosted finish. Efficient total internal reflection does not occur at this frosted surface, which may account for the higher predicted J_{sc} (Kennedy *et al.*, 2008b). The measured and predicted *relative* J_{sc} for each single dye concentration, are shown in Figure 2.21. J_{sc} is given relative to that attained for the R4 (0.2 mg/ml Lumogen red 305) sample which obtained the highest J_{sc} of the single dyes. Predicted J_{sc} is lowest for Y1 and R1, in agreement with the measured values. The measured and predicted J_{sc} for each of the four dye mixes are also shown in Figure 2.21, each matching within the experimental error. While reasonable agreement between measurements and predictions is observed, the experimental setup requires some refinement to determine whether *absolute* predicted J_{sc} values match measured values.

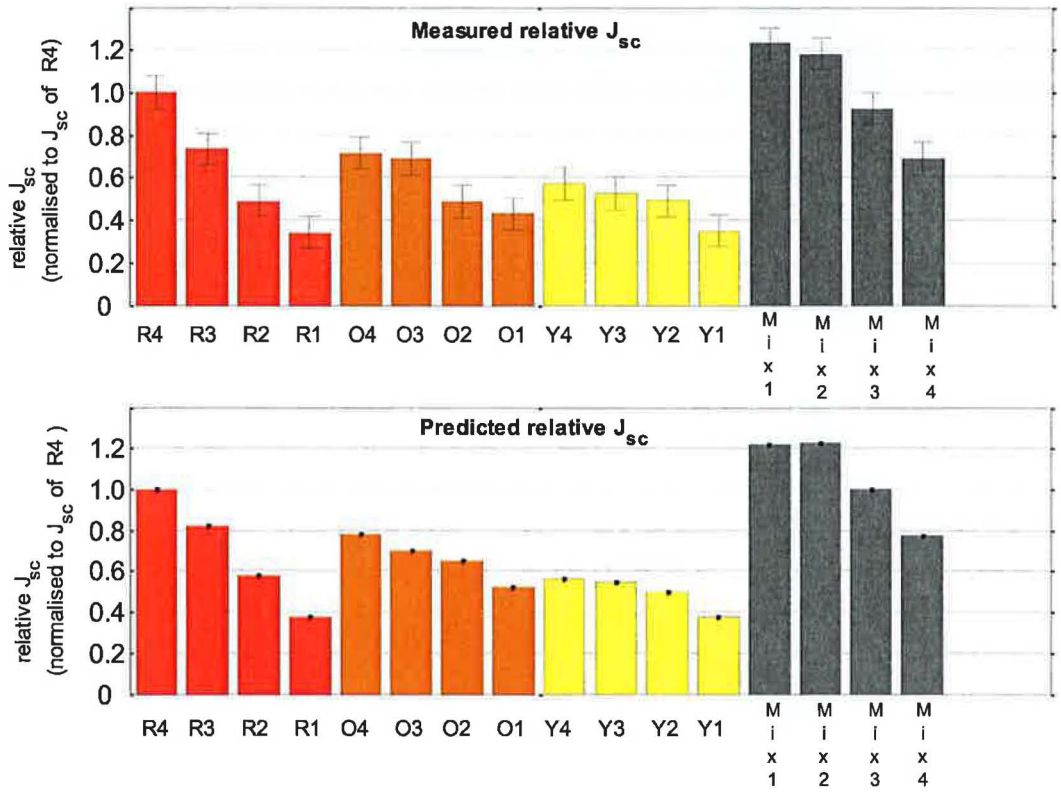

Figure 2.21. Measured and predicted relative short circuit current densities (J_{sc}) for the dye samples listed in Table 2.2.

2.2.6 Comparison with analytically predicted loss mechanisms

External top surface reflection losses, escape-cone losses, and η_{opt} of a QDSC were calculated for varying plate refractive index, n, using the ray-trace model. An ideal QD QY of 100%, α_{mat} of 0 cm^{-1} and a QD emission spectrum exhibiting zero spectral overlap were assumed. The only loss mechanisms thus remaining are initial reflection losses (proportional to n), and escape-cone losses (proportional to $1/n$). The variation of these loss mechanisms and η_{opt} with n is shown in Figure 2.22. With zero re-absorption and QY losses, η_{opt} for LSCs is predicted *analytically* (Goetzberger and Greubel, 1977) for vertical incidence from;

$$\eta_{opt} = 4(n^2 - 1)^{1/2} / (n+1)^2 \qquad 2.19$$

Analytically and ray-trace predicted η_{opt} match closely, as shown in Figure 2.22, thus validating the ray-trace reflection/transmission algorithms (Kennedy *et al.*, 2007a). Figure 2.22 also shows that ~25% of QD emitted photons are lost in the escape cone for n=1.5, in agreement with analytical predictions (Goetzberger and Greubel, 1977; Batchelder *et al.*, 1979).

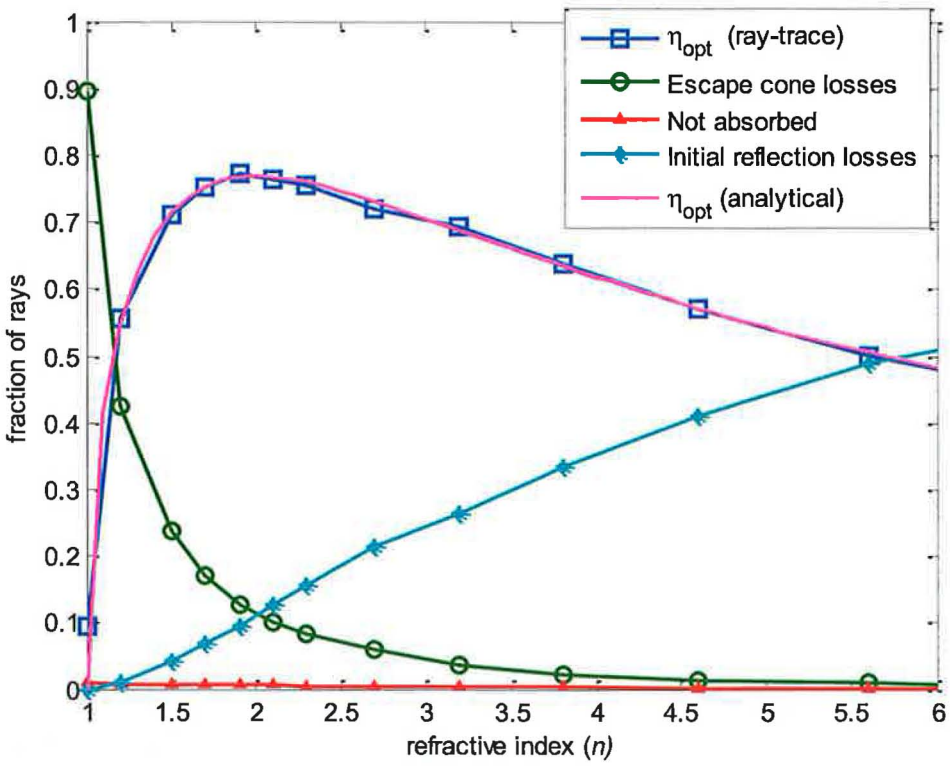

Figure 2.22. Ray-trace predicted η_{opt} and loss mechanisms with varying refractive index, n. Analytically predicted η_{opt} is also shown. Ideal absorption and emission spectra with no spectral overlap, a QD QY=100%, α_{mat} = 0 cm^{-1}, and R_{mirror}=1.0 are assumed.

2.2.7 Comparison with predictions from other models

Two LSC plates of different sizes containing a red Coumarin dye and two containing a yellow Coumarin dye were fabricated by Chatten *et al.* (2005). The plate dimensions and the labels given to each plate surface are shown in Figure 2.23. The quantum yield of both dyes was determined to be 95% (Chatten *et al.*, 2005).

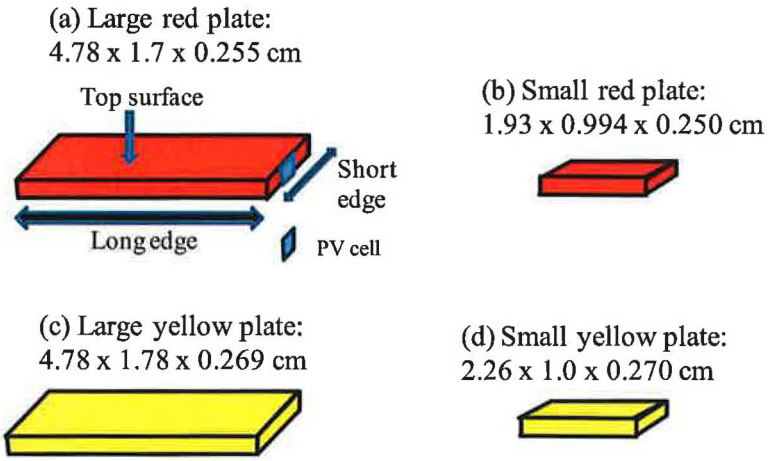

Figure 2.23. The dimensions of two LSC plates containing a Bayer Fluorescent Red Coumarin dye (a) and (b), and two plates containing Fluorescent yellow Coumarin dye (c) and (d).

Predicted photon count emerging at plate edges

The predicted percentage of incident photons emerging at the bottom and top surface of the plate and at the short and long edges, is shown in Figure 2.24 (Kennedy *et al.*, 2008a). The predictions were compared with those from a ray-trace model developed at the Energy Research Centre of the Netherlands (ECN) (Burgers *et al.*, 2005), and from a Thermodynamic model developed at Imperial College London (ICL) (Chatten *et al.*, 2003). There is agreement between all three models, with an *average* absolute difference in photons emerging at all surfaces of 0.3% and a *maximum* absolute difference of 1.0%. The differences can be attributed to the differing absorption calculation methods used in each model.

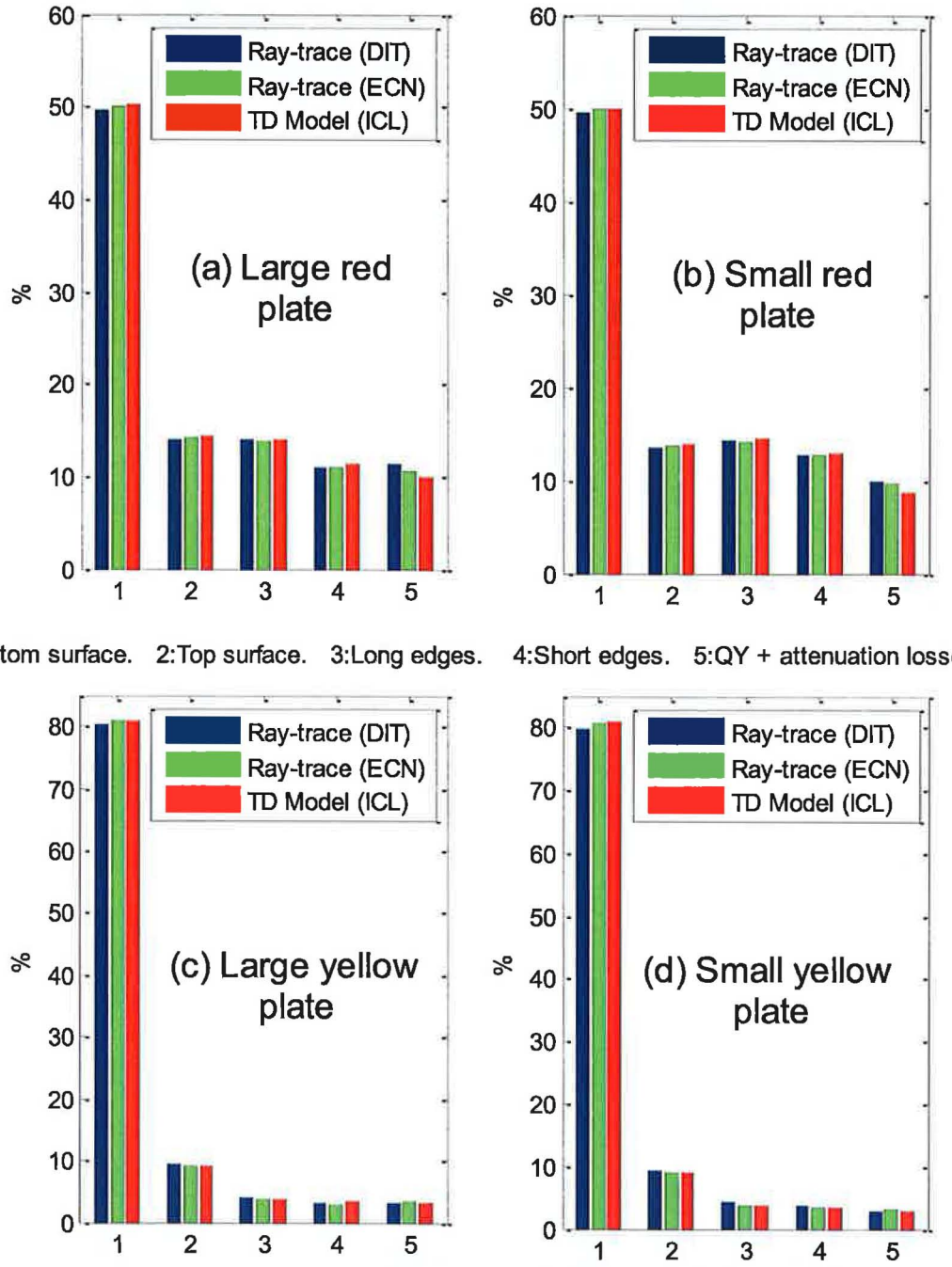

Figure 2.24. Percentage of photons exiting; "1":bottom surface, "2":top surface, "3":two long edges, and "4":two short edges, of four different LSC plates. Predictions are shown for the DIT ray-trace model (blue bars), the ECN ray-trace model (green bars) and the ICL Thermodynamic model (red bars). Total predicted QY and matrix absorption losses are also shown by the bars labelled "5".

Predicted electrical output

The short circuit current density, J_{sc}, of a silicon photodiode attached at the short edge of each of the four LSC plates was measured by Chatten *et al.* (2005). The photodiode spectral response and its angle dependent reflectivity are used with the predicted photon count escaping at the short edge to obtain the predicted J_{sc}. Table 2.3 shows the measured and predicted J_{sc} from the four LSC devices. There is agreement, within experimental error, between the predicted and observed values. The error in predicted values is due to uncertainty in the incident light intensity used as model input.

		J_{sc} (mA/m^2)	
		Measured	Predicted by ray-trace model
Plate	Red Large	53.2 ± 2.0	51.9 ± 2.59
	Red Small	22.5 ± 2.0	24.9 ± 1.24
	Yellow Large	10.4 ± 2.0	9.3 ± 0.46
	Yellow Small	5.2 ± 2.0	5.0 ± 0.25

Table 2.3. Comparison of measured and predicted J_{sc} values of the four dye LSC plates.

2.3 Model assumptions, limitations, and uncertainties.

PV model

In the model, PV cell short circuit current is assumed to increase linearly with C. In silicon PV cells open circuit voltage, V_{oc}, increases logarithmically with C. For example, an increase of ~5% in V_{oc} was obtained by Sidrach de Cardona *et al.* (1985b) for an LSC with C ≈ 4 compared to the same PV cell not attached to the LSC. In the current model V_{oc} is assumed to be constant with C. Predicted LSC power output, therefore, underestimates the power output of a fabricated LSC.

Temperature effects have not been included in the model. Optical concentration of light on a PV cell results in a temperature increase and a resulting decrease in cell efficiency. However, light transmitted to the PV cell within a *luminescent* concentrator is in the wavelength region where the cell IQE is close to its maximum. Therefore, temperature increases in the PV cell attached to a *luminescent* concentrator would be lower compared to that in the same cell attached to an *optical* (non wavelength shifting) concentrator with an equivalent photon count concentration ratio.

Luminescent species emission

Discrete energy levels exist in an individual QD. Therefore, photon emission would be expected to occur at a wavelength equivalent to the absorption onset wavelength of the individual QD. In a QD ensemble, therefore, the emission spectrum should correspond to the absorption onset of the ensemble. However, the emission peak is observed at a slightly *longer* wavelength than the absorption onset. This redshift has been shown experimentally to be related to the QD ensemble inhomogeneous broadening linewidth (Patanè *et al.*, 2000; Patanè *et al.*, 2001) and the redshift tends to zero for a homogeneous (identical size) ensemble of QDs. Patanè *et al.* propose that carriers can thermally escape from QDs and redistribute by diffusing from high energy to lower energy dot states. This process is not inherently modelled in the ray-trace approach. Instead, a *measured* photon emission spectrum[v], representative of the ensemble emission, is used as model input. The emission measurement used as model input should be taken from a very low QD doping

[v] or, ideally, a series of spectra for varying incident wavelengths, as detailed in section 2.1.4.

concentration so as to omit effects of re-absorption and subsequent emission from the spectrum.

In all LSCs modelled, it is assumed that there is no luminescence quenching with increasing doping concentration, that the QY is independent of excitation wavelength, and that emitted light is unpolarised. While the assumptions made may over-simplify the real physical processes underlying photon absorption and emission in an LSC plate, they are sufficiently detailed to allow accurate predictions of LSC electrical and spectral output, as shown in section 2.2.

Solar radiation

To simplify the analysis in sections 3 and 4, two specific skyward angular distributions are considered - either a) isotropic, representing the diffuse component of solar radiation angular distribution, as proposed by Liu and Jordan (1960) or b) non-existent, i.e. at normal incidence only. Section 5 utilises a more detailed solar radiation model which allows for more realistic angular distributions to be simulated.

Model uncertainties

Taking the assumptions made above (i.e. those made for modelling photovoltaic energy conversion and luminescent species emission) as accurate, model predictions can still only be made to within the uncertainty in the input parameters, i.e.;

- luminescent QY,
- incident light spectral irradiance and angle,
- magnitude of matrix material absorption and scattering,
- external mirror reflectivity,

- matrix material refractive index.

The predicted error bars in any given subsection of section 2 quantify the error arising due to uncertainty in the model input parameter/s which significantly affect the *relative* electrical output. For example, the most significant source of error affecting the relative electrical output of the devices in sections 2.2.3 and 2.2.4, where the QD QY is very low (QY < 15%), arises from inhomogeneous matrix material scattering in different QDSC samples. At higher QYs, uncertainty due to inhomogeneous matrix material scattering is relatively less significant, as shown by Figure 2.16. The predicted error in the more efficient dye LSC plates (where the QY = 95%), detailed in section 2.2.7, is most significantly affected by the uncertainty in the incident light intensity (Chatten, 2008). Where the predicted electrical output is given without error bars, the assumption is made that model input parameters are exact. Stochastic error arises from using the Monte-Carlo approach. To reduce stochastic error and produce repeatable results, the model must be run for longer, i.e., using more input rays. The number of decimal places used for predicted results indicates the level of certainty at which the model attains *repeatable* results over successive programme runs.

2.4 Chapter conclusions

- The algorithms behind modelling each of the main processes in a QDSC have been detailed. Using a Monte-Carlo approach, these processes have been combined to form a multi-parameter ray-trace model of QDSCs, enabling the principal interdependent, competing loss mechanisms to be quantified.
- Visualisation of the traced rays around varying QDSC configurations provides an initial check that the geometric ray-trace algorithms have been implemented correctly. Agreement between ray-trace model and analytic predictions of top surface reflection losses and escape cone losses, with varying plate refractive index, provides a further validation.
- A matrix material scattering approximation is included in the model to enable comparison with measured η_{opt} from fabricated QDSCs, where the QD QY was found to be very low.
- To validate the model, predictions are compared with a range of experimental measurements;

- Predicted η_{opt} are in good agreement with measured values from QDSCs of varying *size* and QD *doping concentration*.
- Predicted η_{opt} of QDSCs with varying *shape* match measured values, although more plates of each geometry type are required here for a validation.
- Predicted edge emission spectra, using varying *input laser spot positions* on the device top surface aperture, show good agreement with measured spectra.
- Predicted trends in electrical output of liquid LSCs containing *multiple dyes* of *varying concentrations* match measured trends.

- The results indicate that photon absorption and emission, and re-absorption of light and transport losses within the LSC plate are determined accurately by the ray-trace model.
- There is a high level of agreement between predicted and observed electrical output from four dye LSC plates, as well as between the predictions of the ray-trace and two other LSC models.
- The ray-trace approach provides a tool for quantifying device loss mechanisms and optimizing QDSC design in terms of varying geometry, luminescent species, matrix material, external reflector, and PV cell types.

2.5 References

Bailey, S.T., Lokey, G.E., Hanes, M.S., Shearer, J.D.M., McLafferty, J.B., Beaumont, G.T., Baseler, T.T., Layhue, J.M., Broussard, D.R., Zhang, Y., Wittmershaus, B.P., (2007). Optimized excitation energy transfer in a three-dye luminescent solar concentrator. *Solar Energy Materials and Solar Cells,* 91, 1, 67-75.

Batchelder, J.S., Zewail, A.H., Cole, T., (1979). Luminescent solar concentrators. 1:Theory of operation and techniques for performance evaluation. *Applied Optics,* 18, 18, 3733-54.

Bose, R., Farrell, D.J., Chatten, A.J., Pravettoni, M., Büchtemann, A., Barnham, K.W.J., (2007). Novel configurations of luminescent solar concentrators. *Proceedings of 22nd European Photovoltaic Solar Energy Conference and Exhibition*, Milan, Italy, 210-4.

Bourke, P., (1989). local.wasp.uwa.edu.au/~pbourke/geometry/ (last accessed 20/7/09)

Burgers, A.R., Slooff, L.H., Büchtemann, A., Van Roosmalen, J.A.M., (2006). Performance of single layer Luminescent Concentrators with multiple dyes. *Proceedings of 4th World Conference on Photovoltaic Energy Conversion*, Hawaii, USA, 198-201.

Burgers, A.R., Slooff, L.H., Kinderman, R., Van Roosmalen, J.A.M., (2005). Modelling of Luminescent Concentrators by Ray-tracing. *Proceedings of 20th European Photovoltaic Solar Energy Conference*, Barcelona, Spain, 394-7.

Carrascosa, M., Unamuno, S., Agullo-Lopez, F., (1983). Monte-Carlo simulation of the performance of PMMA luminescent solar collectors. *Applied Optics,* 22, 20, 3236-41.

Chatten, A.J., Barnham, K.W.J., Buxton, B.F., Ekins-Daukes, N.J., Malik, M.A., (2003). A new approach to modelling quantum dot concentrators. *Solar Energy Materials and Solar Cells,* 75, 3-4, 363-71.

Chatten, A.J., Barnham, K.W.J., Buxton, B.F., Ekins-Daukes, N.J., Malik, M.A., (2004). Quantum Dot Solar Concentrators and Modules. *Proceedings of 19th European Photovoltaic Solar Energy Conference and Exhibition*, Paris, France, 109-13.

Chatten, A.J., Farrell, D.J., Jermyn, C., Thomas, P., Buxton, B.F., Büchtemann, A., Danz, R., Barnham, K.W.J., (2005). Thermodynamic modelling of luminescent solar concentrators *Proceedings of 31st IEEE Photovoltaic Specialists Conference and Exhibition*, Orlando, USA, 82-5.

Chatten, A.J., (2008). *Private Communication.*

Gallagher, S.J., Eames, P.C., Norton, B., (2004). Quantum dot solar concentrator behaviour predicted using a ray trace approach. *International Journal of Ambient Energy,* 25, 1, 47-56.

Gallagher, S.J., Rowan, B.C., Doran, J., Norton, B., (2007). Quantum dot solar concentrator: Device optimisation using spectroscopic techniques. *Solar Energy,* 81, 4, 540-7.

Glassner, A.S., (1989). *An introduction to ray-tracing*, Academic Press, London, United Kingdom.

Goetzberger, A., Greubel, W., (1977). Solar Energy Conversion with Fluorescent Collectors. *Applied Physics,* 14, 123-39.

Hecht, E., (2002). *Optics*, Addison-Wesley, Reading, Massachusetts, USA.

Heidler, K., Goetzberger, A., Wittwer, V., (1982). Fluorescent Planar Concentrator. Monte-Carlo Computer Model, Limit Efficiency, and Latest Experimental Results. *Proceedings of 4th Photovoltaic Solar Energy Conference*, Stresa, Italy, 682-6.

Kennedy, M., Chatten, A.J., Farrell, D.J., Bose, R., Büchtemann, A., McCormack, S.J., Doran, J., Barnham, K.W.J., Norton, B., (2008a). Luminescent Solar Concentrators: A Comparison of Thermodynamic Modelling and Ray-trace Modelling Predictions. *Proceedings of 23rd European Photovoltaic Solar Energy Conference and Exhibition*, Valencia, Spain, 334-7.

Kennedy, M., Dunne, M., McCormack, S.J., Doran, J., Norton, B., (2008b). Multiple dye luminescent solar concentrators and comparison with Monte-Carlo ray-trace predictions. *Proceedings of 23rd European Photovoltaic Solar Energy Conference and Exhibition*, Valencia, Spain, 390-3.

Kennedy, M., McCormack, S.J., Doran, J., Norton, B., (2007a). Modelling of Re-absorption Losses in Quantum Dot Solar Concentrators. *Proceedings of 3rd Photovoltaic Science Application and Technology Conference*, Durham, UK, 123-6.

Kennedy, M., Rowan, B.C., McCormack, S.J., Doran, J., Norton, B., (2007b). Modelling of a Quantum Dot Solar Concentrator and Comparison with Fabricated Devices. *Proceedings of 3rd Photovoltaic Science Application and Technology Conference*, Durham, UK, 27-30.

Liu, B., Jordan, R., (1960). The interrelationship and characteristic distribution of direct, diffuse and total solar radiation. *Solar Energy*, 4, 3, 1-19.

Patanè, A., Levin, A., Polimeni, A., Eaves, L., Main, P.C., Henini, M., (2000). Carrier thermalization within a disordered ensemble of self-assembled quantum dots. *Physical Review B,* 62, 16, 11083-7.

Patanè, A., Levin, A., Polimeni, A., Eaves, L., Main, P.C., Hill, G., (2001). Universality of the Stokes Shift for a Disordered Ensemble of Quantum Dots. *physica status solidi (b),* 224, 1, 41-5.

Reisfeld, R., Eyal, M., Chernyak, V., Zusman, R., (1988). Luminescent Solar Concentrators based on Thin Films of Polymethylmethacrylate on a Polymethylmethacrylate Support. *Solar Energy Materials,* 17, 439-55.

Richards, B.S., McIntosh, K.R., (2006). Ray-Tracing simulations of Luminescent Solar Concentrators Containing Multiple Luminescent Species. *Proceedings of 21st European Photovoltaic Solar Energy Conference*, Dresden, Germany, 185-8.

Richards, B.S., McIntosh, K.R., (2007). Overcoming the poor short-wavelength spectral response of CdS/CdTe photovoltaic modules via luminescence down-shifting - ray-trace simulations. *Progress in Photovoltaics,* 15, 1, 27-34.

Rowan, B.C., (2007). PhD Thesis: The Development of a Quantum Dot Solar Concentrator. School of Physics, Dublin Institute of Technology, Dublin.

Rowan, B.C., McCormack, S.J., Doran, J., Norton, B., (2007). Quantum Dot Solar Concentrators: An investigation of various geometries. *Proceedings of SPIE Optics and Photonics and Solar Energy Conference*, San Diego, USA, 66490A-1.

Schüler, A., Kostro, A., Galande, C., Valle del Olmo, M., deChambrier, E., Huriet, B., (2007). Principles of Monte-Carlo ray-tracing simulations of quantum dot

solar concentrators. *Proceedings of International Solar Energy Society World Solar Congress*, Beijing, China, 1033-7.

Sidrach de Cardona, M., Carrascosa, M., Messeguer, F., Cusso, F., Jaque, F., (1985). Outdoor evaluation of luminescent solar concentrator prototypes. *Applied Optics,* 24, 13, 2028-32.

Thomas, W.R.L., Drake, J.M., Lesiecki, M.L., (1983). Light transport in planar luminescent solar concentrators: the role of matrix losses. *Applied Optics,* 22, 21, 3440-9.

van Sark, W.G.J.H.M., (2008). *Private Communication.*

3 Device geometry

3.0 Introduction

3.0.1 QDSC geometry

Current fabricated QDSCs utilise a planar rectangular geometry. Quantifying the net effect of varying device geometry on QDSC solar energy concentration ratios (C) is a non-trivial problem owing to the multiple, interdependent, competing loss mechanisms in the device. The ray-trace model, described in chapter 2, provides a tool for doing so. A novel analysis of device geometry is undertaken using ray-trace predictions to calculate relative costs per unit power output of varying two-dimensional planar QDSC shapes. The analysis shows that, under certain assumptions, each two-dimensional planar geometry attains the same minimum cost per unit power, indicating that no advantage accrues from varying the plate shape.

The predictions show that the correct selection of the concentrator top surface aperture area is crucial in minimising QDSC cost per unit power output – an important criterion not previously highlighted in the research literature. For example, the predicted cost per unit power of a particular 7 x 7 cm square QDSC is 10% lower than that of an 11 x 11 cm square QDSC with the same properties, despite a higher C attained in the latter. Obtaining a 10% decrease in the cost per W_p by altering only the dimensions of the device illustrates the importance of utilizing accurate QDSC modelling techniques.

Whether PV cells are attached at (a) one side of a plate only, or (b) at all sides of the plate perimeter has multiple effects on power output and costs; (i) A higher C

is attained in case (a) due to the higher geometric gain, (ii) the power output may be lower in case (a), despite the higher C, due to the smaller area of PV cells attached, and (iii) the cost in case (a) is lower. The net effect of PV cell distribution on cost per unit power is quantified using the ray-trace model predictions.

Re-absorption losses, which increase with higher QD doping concentration levels, severely limit the potential C of QDSC devices, as is discussed in section 4.1. Current fabricated QDSCs utilise a planar geometry with plates of uniform thickness. A tapered QDSC is proposed, with the aim of reducing re-absorption losses in the device. This configuration would allow a lower QD doping concentration to be used to attain a given absorption efficiency, thereby reducing re-absorption losses. The disadvantage is that the internal optical efficiency decreases due to the sloped surfaces of the tapered devices. Ray-trace modelling is used to investigate the net effect of tapered geometry on device C. The results show an overall decrease in C for tapered devices, compared to plates of uniform thickness.

3.0.2 Solar tree geometry

A luminescent "solar tree" system is proposed in section 3.2, where fibre optics are used to transmit light exiting multiple plates, or "leaves", to a single PV cell via a 2^{nd} stage concentrator. Potentially, the concept allows high solar energy concentration ratios to be attained under direct or diffuse insolation conditions. However, the maximum concentration ratio of the 2^{nd} stage concentrator, C_2, is limited by the angular distribution of light exiting the fibre optics. It is shown that the limitations in C_2, combined with the additional associated costs of the fibre optics required, result in no cost per unit power reduction for the solar tree structure

compared with that of a single-plate QDSC. If fibre optic costs were significantly reduced compared to current levels, however, then the concept should be further evaluated.

3.0.3 Luminescent down-shifting layer geometry

Luminescent down-shifting (LDS) layers, examined in section 3.3, can enhance the short circuit current density, J_{sc}, of solar cells by transforming the wavelength of incident light from short to longer wavelengths better matching the spectral response of the cell. LDS layers are modelled, to investigate whether the optical properties of *QDs* (i.e. broad absorption range and characteristic increased absorption in the UV and blue wavelength regions) make them a more suitable candidate than organic dyes for incorporation in LDS layers. Predictions for LDS layers containing two types of commercially available QDs show only a limited potential enhancement in J_{sc} of a mc-Si cell (~1%), and show no enhancement in J_{sc} when compared to an LDS layer incorporating particular organic dyes.

In "partially-covered" LDS (PC-LDS) layers a reduced fraction of the down-shifting layer is covered with PV cells, thereby introducing a geometric concentration effect not present in an LDS layer. The performance of PC-LDS layers incorporating currently available luminescent dyes is quantified for the first time for varying device sizes. As with LSC plates, the optimum size of a PC-LDS layer, of given optical parameters, must be determined. It is shown that, for the particular dye modelled, the optimum PC-LDS configuration yields a significantly higher device power conversion efficiency compared to an optimised LSC device fabricated using the same materials.

3.1 An investigation of QDSC geometry

3.1.1 Concentration ratios for varying device geometry

Roncali and Garnier (1984) showed that, for any given concentrator top surface aperture area, A_{conc}, hexagonal LSCs attain higher C than square or triangular shaped LSCs, resulting from the higher geometric gain, G_{geom}, of the hexagonal geometry. In general, C increases as the number of sides in the LSC polygon increases, for any given A_{conc}. Circular LSCs, therefore, attain the highest C as concluded by Reisfeld and Jorgensen (1982) and by Roncali and Garnier. Hexagonal geometry is preferable to circular, however, for fabricating larger panels containing multiple adjacently packed LSC plates, as it is possible to pack the plates in a honeycomb formation without gaps between individual plates (Sidrach de Cardona *et al.*, 1985a). As the concentration ratio attained for hexagonal geometry is close to that of circular geometry, hexagonal geometry was proposed as the optimum. In terms of cost per W_p, hexagonal geometry may not be advantageous, however. To investigate this, and to compare with previous findings of Roncali and Garnier, C are determined for varying geometry types using the ray-trace model.

Using QD photon absorption spectrum 5 and the QD emission spectrum, shown in Figure 3.1, C is calculated for 0.3 cm thick QDSC plates, of varying geometry type and size, using eqn. 2.14. Square, right-angled triangular, hexagonal and "circular" geometries are considered. Two specific PV cell configurations are considered – a) PV is placed at one side only and external mirrors at the other sides, as shown in Figure 3.2, and b) PV is placed around the full perimeter of each device. The circular devices modelled have a single PV cell attached, where the length of the

cell is equal to the radius of the circle. A QD quantum yield of 100%, matrix material absorption coefficient, α_{mat}, of 0.02 cm^{-1}, and refractive index of 1.5, and external mirror reflectivity, R_{mirror}, of 0.94 are assumed in the analysis.

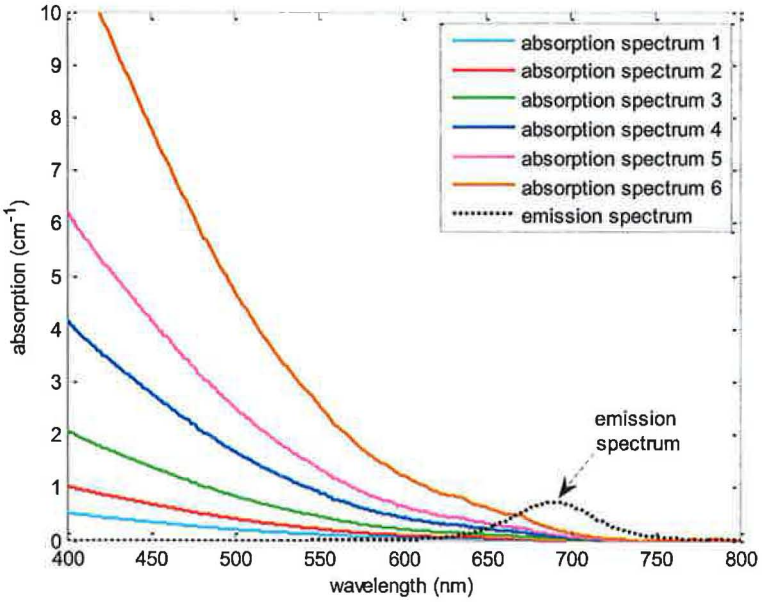

Figure 3.1. Absorption spectrum 1 is the measured photon absorption spectrum of CdSe QDs with CdS/CdZnS/ZnS multi-shell coating (fabricated at Utrecht University). Absorption spectra 2-6, corresponding to higher QD doping concentrations, are extrapolated from absorption spectrum 1.

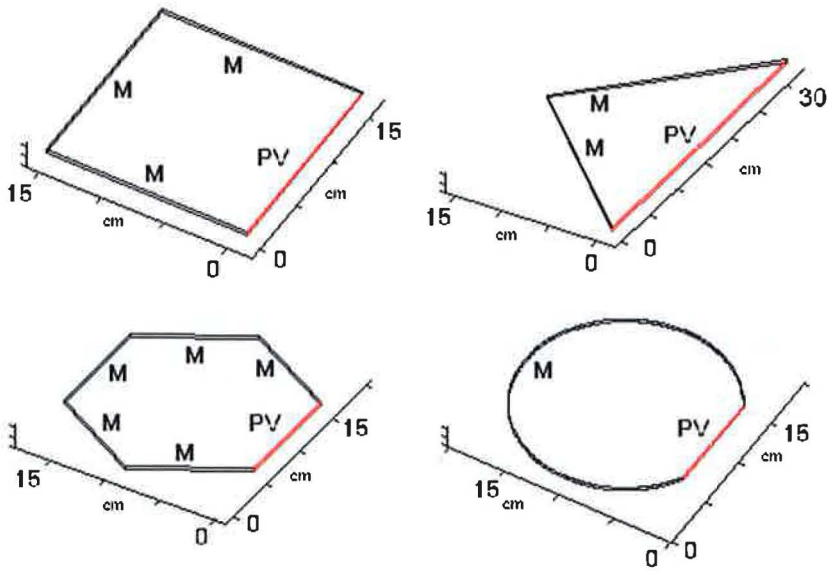

Figure 3.2. Square, right angled triangular, hexagonal and circular devices with A_{conc} = 256cm^2. External mirrors (M) may be placed at the "non PV" sides, as indicated here, or PV may be placed at all sides of the device perimeter.

The predicted C are given in Figure 3.3. The circular geometry attains the highest C for the range of A_{conc} considered, matched closely by the hexagonal geometry as was found by Roncali and Garnier (1984). With PV placed at one side only of each device, predicted C are higher than those assuming PV around all sides of the perimeter. This is due to the decreased area of attached PV, A_{pv}, and the resulting higher G_{geom}. However, the geometry which attains the highest C is not necessarily the optimum in terms of the cost per unit power output. This is investigated, under certain material capital cost assumptions, in section 3.1.2.

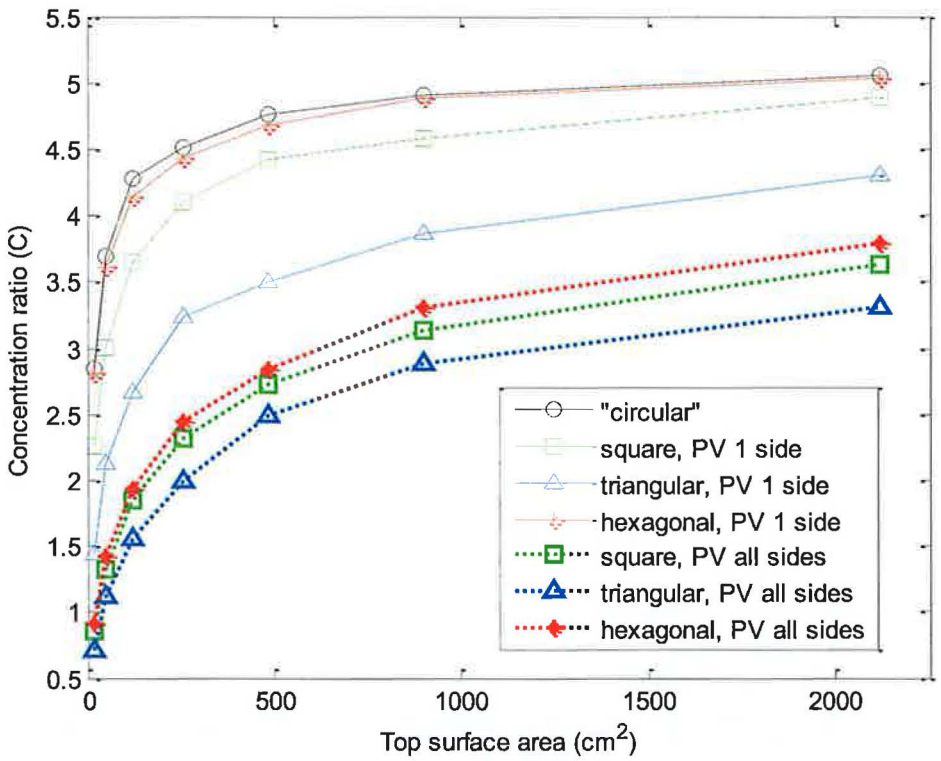

Figure 3.3. Predicted concentration ratios, C, for devices of varying geometry and top surface aperture area, A_{conc}.

3.1.2 Optimum device geometry - relative costs per unit power output

In section 3.1.1, hexagonal geometry was found to attain higher C than rectangular or triangular geometries, for the range of A_{conc} considered. However, the aim of the LSC is to reduce the cost per Watt peak (W_p) of photovoltaic generated power, not to maximise C. A new approach is undertaken to determine the optimum QDSC geometry type, whereby the relative cost per unit power output is calculated for each of the shapes and sizes considered in section 3.1.1. Circular geometry is excluded due to the difficulty, previously outlined, in packing multiple plates efficiently onto a larger panel.

For each particular device shape and size, the relative power output is assumed to be proportional to the product of A_{pv} and the resulting device C;

$$\text{relative power} = A_{pv}C \tag{3.1}$$

The relative total production cost of a device is assumed to be proportional to the quantity of materials required, and is calculated using A_{conc} and A_{pv};

$$\text{relative cost} = (A_{pv}) + \left(\frac{A_{conc}}{costfactor} \right) \tag{3.2}$$

The variable *costfactor*, defining the cost of the concentrator plate relative to the cost of PV per unit area, is given by;

$$costfactor = \frac{\text{cost of PV per unit area}}{\text{cost of concentrator plate per unit area}} \tag{3.3}$$

A *costfactor* of 15 is considered. Taking the cost of PV to be €450/m^2, then the cost of the concentrator plate in this case would be €30/m^2, similar to that estimated for a LSC plate containing a dye (Meyer, 2007). The relative cost per unit power output for each particular shape and size can thus be calculated from;

$$\text{relative cost per unit power} = \frac{\text{relative cost}}{\text{relative power}} = \frac{1}{C} + \frac{A_{conc}}{CA_{pv}\,costfactor} = \frac{1}{C} + \frac{G_{geom}}{C\;costfactor} \qquad 3.4$$

Figure 3.4 (a) and (b) show the relative cost per unit power assuming a *costfactor* of 15. The minimum relative cost per unit power is ~0.8, which corresponds to a 20% decrease in the production cost per W_p compared to that of the mc-Si cells used. Hexagonal, square, and triangular geometry all attain the same minimum cost per unit power, indicating that there is no advantage in using any specific 2-D planar geometry. Significantly, approximately the same minimum cost per unit power is achieved whether PV is placed at one side only, or at all sides of the device perimeter.

The model predictions do show, however, that the correct selection of A_{conc} is crucial in minimising QDSC cost per unit power output – an important criterion not highlighted in the literature. For example, (assuming PV is placed at one side only) the predicted cost per unit power of the 7 x 7 cm square QDSC is 10% lower than that of the 11 x 11 cm QDSC. Obtaining a 10% decrease in the cost per W_p solely by altering the dimensions of the device illustrates the importance of utilizing accurate QDSC modelling techniques.

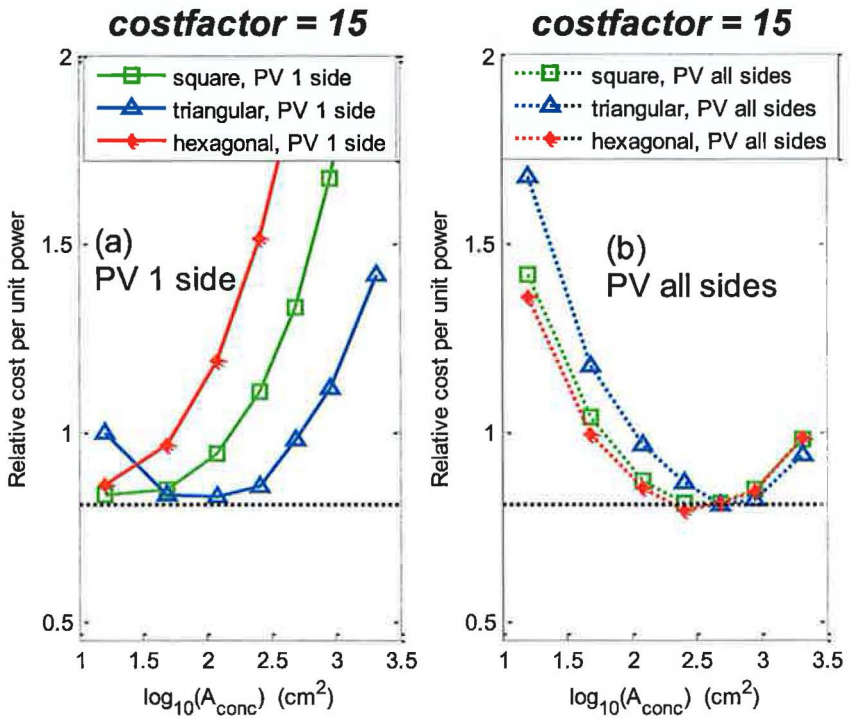

Figure 3.4. Relative cost per unit power for different geometries of varying top surface aperture area (A_{conc}) for two PV cell configurations - (a) PV at one side only, (b) PV at all sides of the perimeter. The price of the concentrator plate per m^2 is assumed to be 15 times less than that of PV per m^2 (i.e. *costfactor* = 15).

Figure 3.5 (a) and (b) show the relative cost per unit power assuming a *costfactor* of *30*. The increase in *costfactor*, compared to that in Figure 3.4, results in a lower QDSC minimum relative cost per unit power, and the optimum plate size of each geometry type shift to larger A_{conc}. Each geometry type, however, still attains the same minimum cost per unit power as the other geometry types. A more detailed cost optimization is presented in section 6, however, the analysis here shows that varying the geometry *type* does not offer any significant reduction in relative cost per unit power, but that the choice of device *size* is critical.

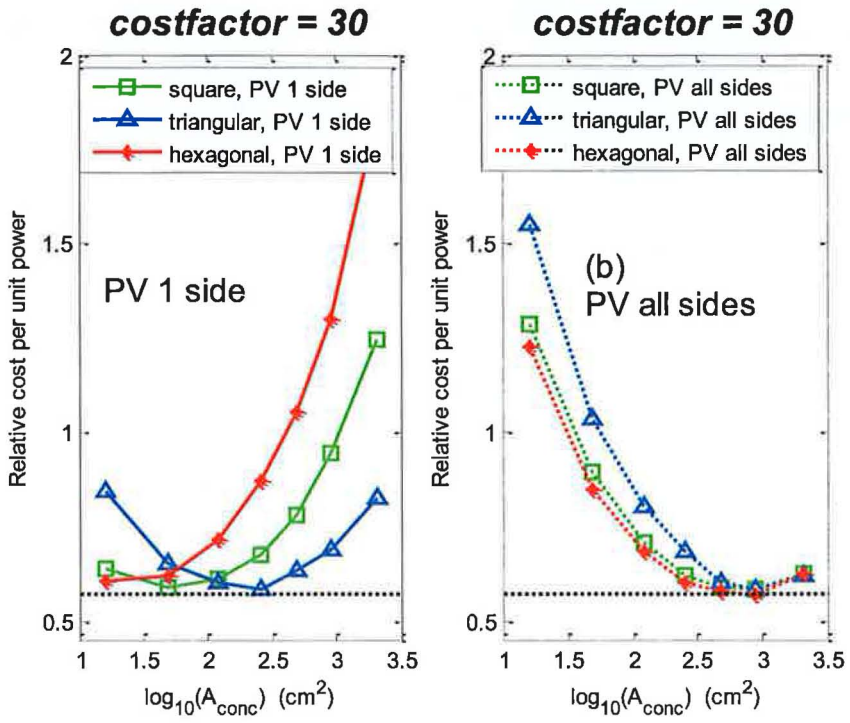

Figure 3.5. Relative cost per unit power for different geometries of varying top surface aperture area (A_{conc}) for two PV cell configurations - (a) PV at one side only, (b) PV at all sides of the perimeter. The price of the concentrator plate per m^2 is assumed to be 30 times less than that of PV per m^2 (i.e. *costfactor* = 30).

3.1.3 Edge effects

It is noted that only the total photon *count* reaching the PV cell has been considered in section 3.1.2, and not the *spatial distribution* of photons along the PV cell. An uneven photon spatial distribution affects the overall fill factor of an *individual* PV cell (Smyth *et al.*, 1999) attached at that side. If *multiple* PV cells were connected in series along one side subject to an uneven incident photon spatial distribution, the overall current would be limited by the cell generating the lowest current. Figure 3.6 shows the predicted spatial distribution of photons along the normalised length of one side of the hexagonal, square, and triangular QDSC plates. The so-called "edge-effect" is less pronounced for hexagonal geometry, as was previously shown by Sidrach de Cardona *et al.* (1985a). For this reason, hexagonal

geometry may offer an advantage over square or triangular shaped plates. The non-uniformity in the photon spatial distribution is easily explained with reference to the two-dimensional LSCs illustrated in Figure 3.7. Isotropic emission is represented by rays originating from the centre of the circle at angular separation intervals of 10°. It is observed that the spatial distribution of rays intersecting each of the three triangle sides is more weighted to the centre of each side. For the hexagon, the distribution is more uniform along each side, and for the circle a uniform distribution is obtained.

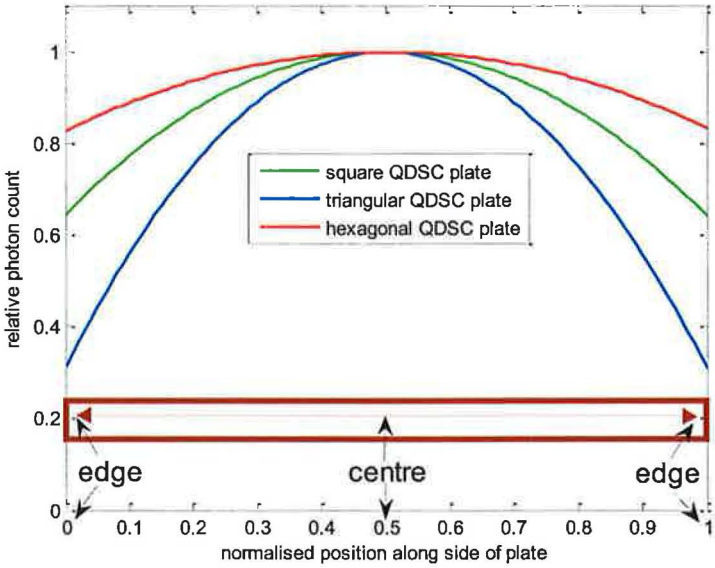

Figure 3.6. Relative photon spatial distribution along the normalised length of one side of the square, triangular and hexagonal QDSC plates. The "edge effect" is greatest for triangular geometry.

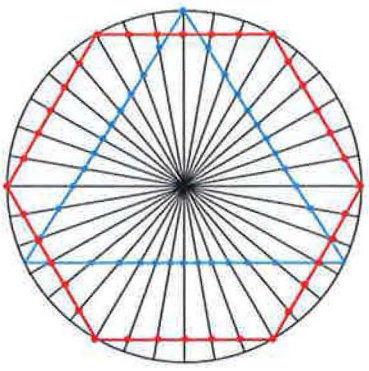

Figure 3.7. The distribution of intersection points of rays (emitted isotropically from the circle centre) with each of the polygon sides is most non-uniform in the triangular geometry.

3.1.4 QDSC plates with reduced thickness

LSC concentration ratio, C, increases with reduced plate thickness (Carrascosa *et al.*, 1983; Roncali and Garnier, 1984). Decreasing the thickness has a two-fold effect – (i) G_{geom} increases, but (ii) the absorption efficiency, η_{abs}, is reduced. By increasing the QD doping concentration η_{abs} can be increased but, in doing so, the internal optical efficiency, η_{int_opt}, is reduced due to higher re-absorption losses in the plate. Hence, an optimum QD concentration exists for each particular plate thickness. The net effect of varying plate thickness on C is examined using the ray-trace model. Square devices of dimensions 11 x 11 cm and of varying plate thickness are modelled, assuming PV cells attached to one side only, as illustrated in Figure 3.8. The QD photon absorption spectra shown in Figure 3.1, corresponding to a range of QD doping concentrations, are used in the model, with the optimum concentration for each plate thickness selected. Predicted η_{opt} decreases with thinner plates, due to a combination of lower η_{abs} and lower η_{int_opt}, as shown in Figure 3.9(a). However, the increase in G_{geom} with thinner plates, as shown in Figure 3.9(b), results in an overall increase in C, indicating significant potential reductions in cost per W_p are realizable with thinner QDSC devices.

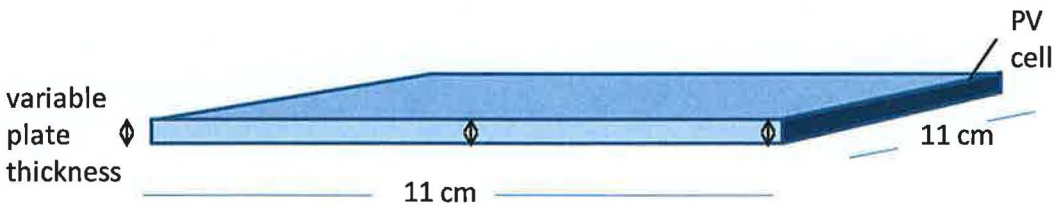

Figure 3.8. Square QDSC 11 x 11 cm plate with variable plate thickness and PV cells attached at one side.

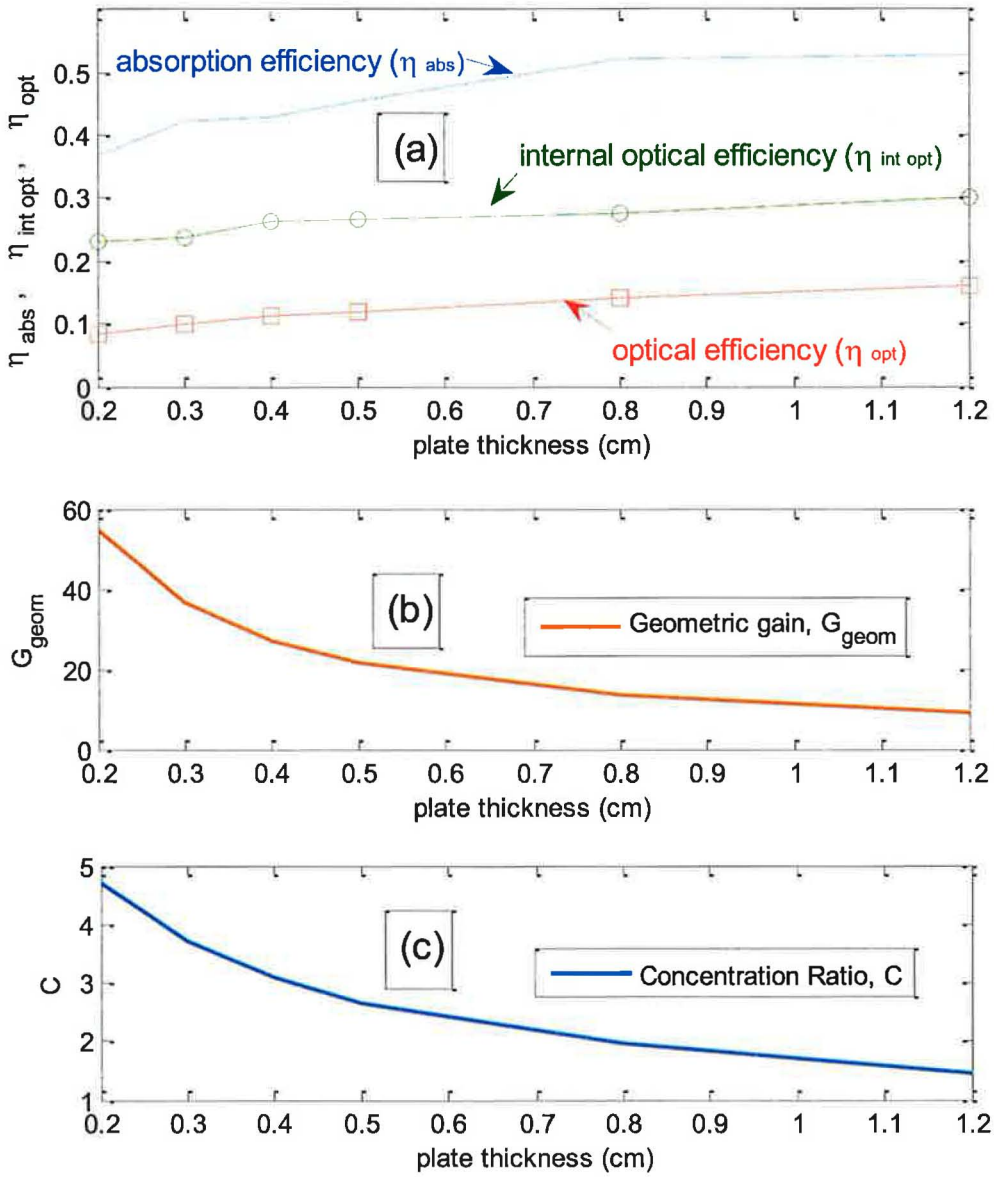

Figure 3.9. (a) shows the decrease in optical efficiency for thinner plates due to lower absorption efficiency and lower internal optical efficiency. However, the increase in geometric gain, as shown in (b), results in an overall increase in C for thinner plates, as shown in (c), where, $C = \eta_{opt} G_{geom}$.

3.1.5 Concentration ratios of tapered QDSC plates

In this section, a tapered QDSC device is proposed with the aim of reducing re-absorption losses in the QDSC, thereby attaining higher solar energy concentration ratios compared to plates of uniform thickness.

Current fabricated devices utilise a planar geometry with plates of uniform thickness. Re-absorption losses, which increase with higher QD doping concentration levels, severely limit the potential C of QDSC devices. A tapered QDSC device, shown in Figure 3.10, is proposed with the aim of reducing re-absorption losses in the QDSC. The thickness of the device is increased on one side, which allows a lower QD doping concentration to be used, thereby reducing re-absorption losses in the plate. The side where the PV is attached remains at a thickness of 0.3 cm, thereby maintaining a high G_{geom}. In the tapered device, however, the angle of propagation of emitted photons is altered by multiple reflections at the sloped top and bottom surface. This causes some photons, emitted initially inside the angular range for TIR, to be lost through the top surface, as illustrated in Figure 3.11. The ray-trace model is used to determine if the net effect is an increase or decrease in C, compared to a device of uniform thickness. Using the optimum QD concentration, from the range of QD concentrations shown in Figure 3.1, C was calculated for varying "side 2" thickness, where "side 2" is indicated in Figure 3.10. The tapered devices do not attain a higher C than the device of uniform thickness, as is shown in Figure 3.12.

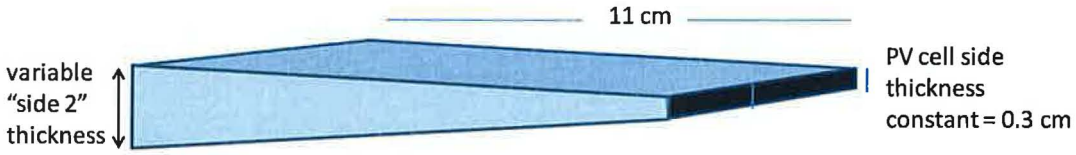

Figure 3.10. QDSC device with tapered geometry. The thickness of the PV side remains constant at 0.3 cm. The thickness of side 2 is varied to investigate the effect on the concentration ratio attained at the PV side.

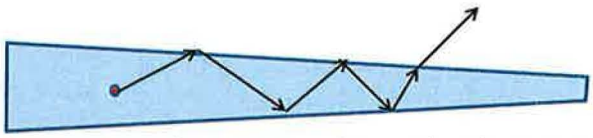

Figure 3.11. For tapered geometry, the angle of propagation of a QD emitted photon is altered after multiple reflections at the sloped top and bottom surfaces. Therefore, photons emitted initially inside the angular range for total internal reflection may be lost through the top surface.

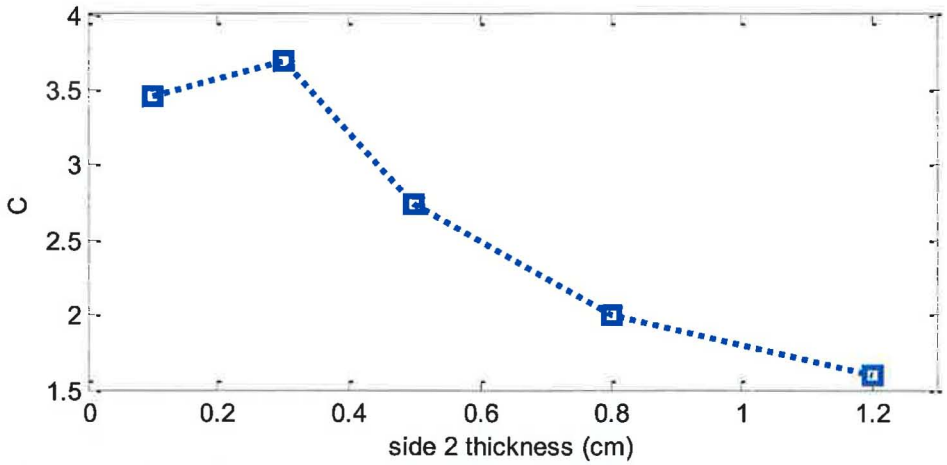

Figure 3.12. Concentration ratio, C, for varying thickness of "side 2". The thickness of the plate at the PV side remains constant at 0.3 cm. The side labels are illustrated in Figure 3.10. The highest C is obtained for a "side 2" thickness of 0.3 cm, i.e. for a plate of uniform thickness.

3.2 Luminescent "solar tree" with 2nd stage concentrator

Figure 3.13 illustrates the concept of the luminescent "solar tree", where fibre optics are used to transmit light exiting multiple plates, or "leaves", to a single PV cell via a 2nd stage concentrator. The concept is investigated to determine whether;

a) A higher concentration ratio compared to a single-plate QDSC is attained.

b) The cost per unit power generated is lower than a single-plate QDSC.

The concentration ratio of the 2nd stage concentrator, C_2, is limited by the angular distribution of light exiting the fibre optics. The angular distribution can be determined from the ray-trace model.

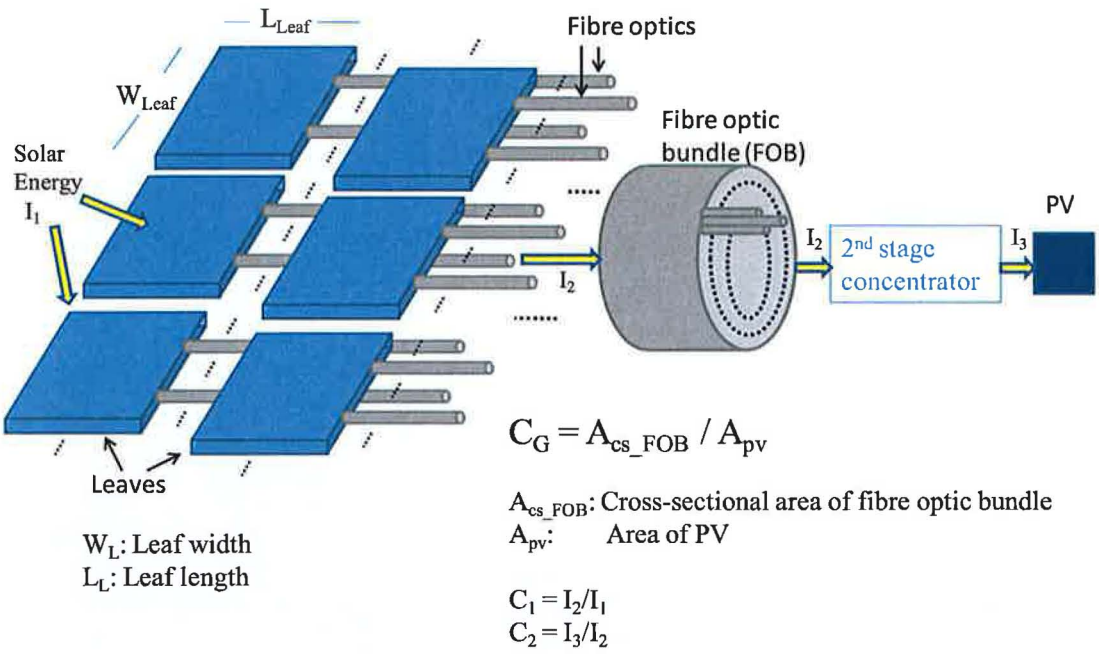

Figure 3.13. Fibre optics collect light along one side of each QDSC "solar leaf". Light is transmitted via the fibre optics, through a 2nd stage concentrator to PV cells. C_1 and C_2 are the effective concentration ratios attained by the individual leaves and the 2nd stage concentrator, respectively. C_G is the ratio of the cross-sectional area of the fibre optic bundle (FOB) to the area of PV cells.

3.2.1 Solar tree components: Solar leaves and fibre optics

Solar leaves

The concentration ratio of a 0.1 cm thick solar leaf is calculated using QD photon absorption spectrum 6 and the photon emission spectrum shown in Figure 3.1. A range of leaf lengths, L_{Leaf}, are considered, with the leaf width, W_{Leaf}, a constant 10.0 cm. The other device parameters assumed, e.g. QD QY, n_2, α_{mat}, R_{mirror}, are as given for the QDSC plates in section 3.1.1. The concentration ratio attained by the leaf, C_1, is shown in Figure 3.14(a) for varying L_{leaf}. The relative cost per unit power of QDSC plates of equivalent dimensions to each particular solar leaf is also calculated, to allow comparison of the solar tree configuration performance with that of single-plate QDSC devices. The QDSC relative cost per unit power is calculated from eqn. 3.4, and is shown in Figure 3.14(b).

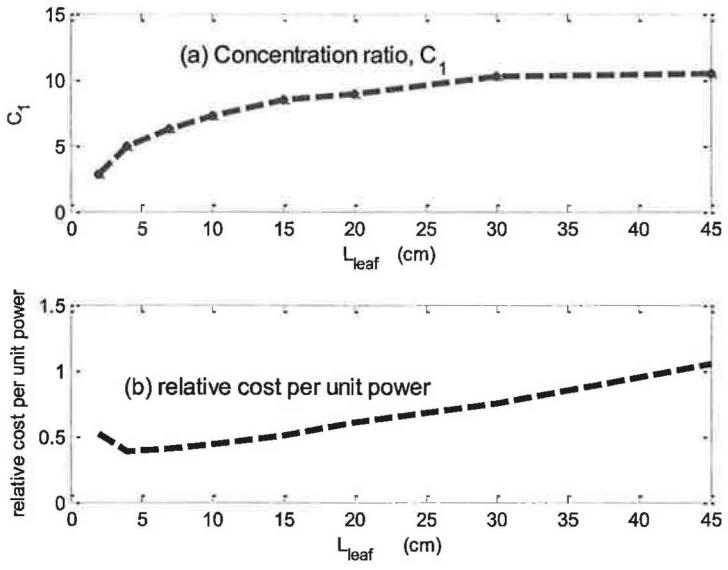

Figure 3.14. (a) C_1 is the concentration ratio attained by the solar leaf, for varying leaf length, L_{Leaf}. (b) To allow comparison of the solar tree configuration with QDSC devices, the relative cost per unit power of equivalent QDSC plate sizes is calculated.

Solar tree fibre optics

To investigate the performance of the solar tree configuration, the following idealistic fibre optic (FO) characteristics are assumed;

- All photons transmitted to the leaf edge and impinging on the FO entrance aperture are within the acceptance angle of the FO, and no reflection occurs at the FO-leaf interface.
- There are no transmission losses in the FOs and no reflection occurs at the FO exit aperture.
- The thickness of the FO cladding is zero.
- To simplify the calculations, FOs have a square cross-section with a width, W_{FO}, equal to the thickness of the solar leaf, as illustrated in Figure 3.15.

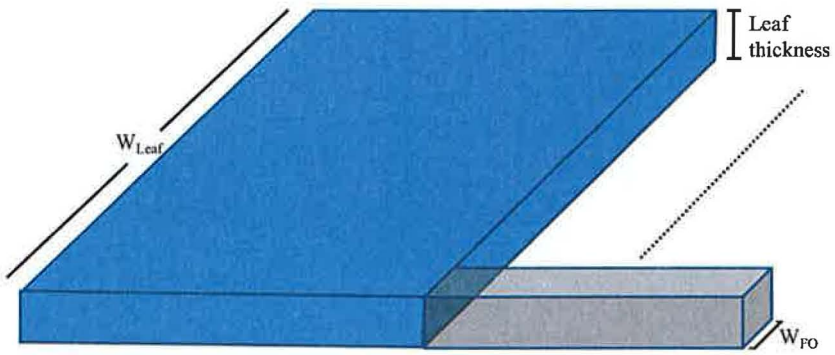

Figure 3.15. As a first approximation, each fibre optic (FO) is assumed to have a square cross section. The width of each FO, W_{FO}, is equal to the thickness of the leaf.

Whether the solar tree components' idealised optical and physical properties are completely realisable or not is not the principal objective in this section. The main aim is to calculate a 1st approximation of the theoretical upper limit of scaleable[vi] solar tree system concentration ratio and cost per unit power output.

[vi] i.e., solar tree systems of varying collector area to PV area ratio

3.2.2 Solar tree 2nd stage concentrator

A compound parabolic concentrator, CPC, (Hinterberger and Winston, 1966; Winston, 1974) may be utilised as the 2nd stage concentrator indicated in Figure 3.13. In an ideal CPC, incident light within the concentrator acceptance angle, θ_a, shown in Figure 3.16(a), is transmitted to the exit aperture. C_G is the CPC geometric concentration ratio, defining the ratio of CPC entry to exit apertures. An *ideal* CPC transmission curve, as shown in Figure 3.16 (b), is assumed in order to simplify initial analysis, however, fabricated CPCs have been shown to achieve close to the ideal transmission curve (Welford and Winston, 1989).

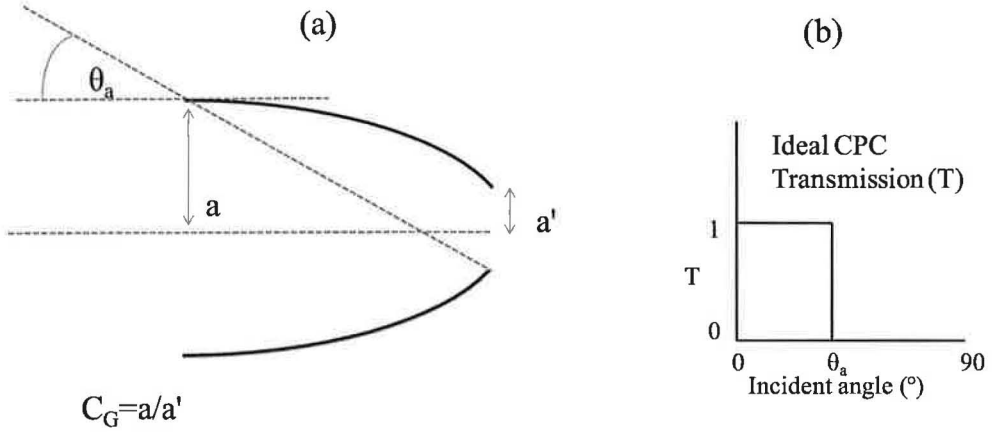

Figure 3.16. (a) C_G is the CPC geometric concentration ratio, defining the ratio of CPC entry aperture, a, to exit aperture, a'. θ_a is the CPC acceptance angle. (b) A CPC with unity transmission for all incident angles $\leq \theta_a$ is considered.

For a 3-D CPC, C_G is less than or equal to;

$$C_G \leq \frac{1}{\sin^2 \theta_a} \qquad 3.5$$

For a dielectric-filled CPC (Winston, 1976), C_G is enhanced by a factor corresponding to the refractive index of the CPC medium, n_{CPC} squared;

$$C_G \leq \frac{n_{CPC}^{\ 2}}{\sin^2 \theta_a} \qquad 3.6$$

C_G, shown in Figure 3.17(b) for varying CPC θ_a is the maximum possible concentration ratio of the CPC, assuming all photons entering the ideal CPC are within θ_a, and assuming n_{CPC} of 1.5. C_2 is defined as the effective concentration ratio of a particular CPC receiving light from the fibre optic bundle (FOB), a proportion of which may be outside θ_a. The angular distribution of photons exiting the FOB, shown in Figure 3.17(a), is determined from the ray-trace model. The fraction of photons incident on the CPC entry aperture which are within θ_a, termed k_a, is shown in Figure 3.17(c). C_2 is thus defined as;

$$C_2 = C_G k_a \qquad 3.7$$

CPC θ_a is inversely proportional to C_2, as shown in Figure 3.17(d). The total system efficiency decreases with higher C_2 due to reduced k_a. More leaves and more FOs would therefore be required to attain a given power output. The relative cost per unit power output of the solar tree system, with varying CPC θ_a, is calculated in section 3.2.3.

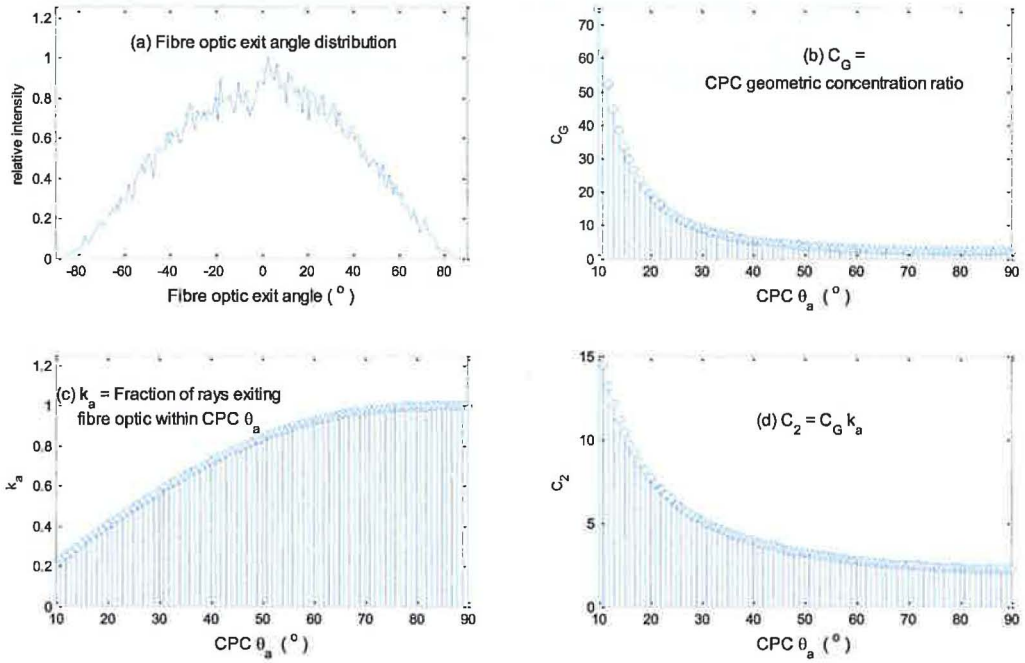

Figure 3.17. (a) Angular distribution of light exiting fibre optic bundle (FOB). (b) C_G is the ratio of the cross-sectional area of the FOB to the area of PV cells, and is determined by the particular CPC acceptance angle, θ_a. (c) k_a is the fraction of photons exiting the FOB which are within the CPC θ_a. (d) C_2 is the effective concentration ratio of the CPC, given the angular distribution of incident photons shown in (a).

3.2.3 Solar tree evaluation for varying fibre optic costs and CPC θ_a

The relative cost per unit power of the solar tree, for varying θ_a and FO cost per unit length is determined by;

$$\text{rel. cost/power} = \frac{1}{C_1 C_2} + \frac{L_{Leaf} C_G}{C_1 C_2 W_{FO} costfactor_1} + \frac{\overline{L_{FO}} C_G}{C_1 C_2 W_{FO} costfactor_2} \qquad 3.8$$

where, $costfactor_1$ and $costfactor_2$ relate the cost of the leaves and FO, respectively, to the cost of the PV per unit area, as detailed in Appendix A. Calculating the cost

per unit power allows a comparison to be made with single-plate QDSCs with equivalent optical properties to those of the individual solar leaves. The following parameter values and assumptions are made;

- C_1 is determined in section 3.2.1 as a function of leaf length, L_{Leaf}, where the optimum length is determined to be ~4.0 cm for a plate thickness of 0.1 cm. A $costfactor_1$ of 45 is considered here, i.e., the relative cost per unit area of the 0.1 cm thick leaves is assumed to be three times less than the 0.3 cm thick plates detailed in section 3.1.2.
- The FO width, W_{FO}, is equal to the thickness of the leaves, i.e., 0.1 cm. The average length of each FO, $\overline{L_{FO}}$, is assumed to be (a minimum of) 0.1 m.
- The FO cost per unit length is varied from €1.00/m to €0.001/m, which correspond to $costfactor_2$ values of 0.45 and 450 respectively, for the particular W_{FO}.
- The CPC geometric concentration ratio, C_G, and overall effective 2nd stage concentration ratio, C_2, for a range of CPC acceptance angles, θ_a are given in Figure 3.17 (b) and (d), respectively.

The predicted relative costs per unit power for the idealised solar tree system are shown in Figure 3.18, showing that FO costs must be significantly less than €0.01/m for the solar tree to attain a lower cost per unit power than an equivalent single-plate QDSC. However, commercial bulk FO prices are currently much higher, ranging from €0.50/m to €5.00/m (OceanOptics, 2009; AnchorOptics, 2009; Kandilli and Ulgen, 2009), depending on the transmission grade, core diameter and material used. It is also noted that, to simplify the initial analysis of the solar tree system, the

cost of the multiple CPCs required is assumed to be zero, and hence the predictions underestimate the solar tree cost per unit power output[vii].

The analysis shows that the solar tree configuration does not result in a reduction in cost per unit power output, compared to that of a QDSC due to (i) the concentration effect of the 2nd stage concentrator being limited by the angular distribution of photons exiting the FOs, and (ii) the associated costs of the additional system components. FO costs need to be < €0.01 per metre for the solar tree system to have manufacturing costs per W_p of the same order as single-plate QDSCs.

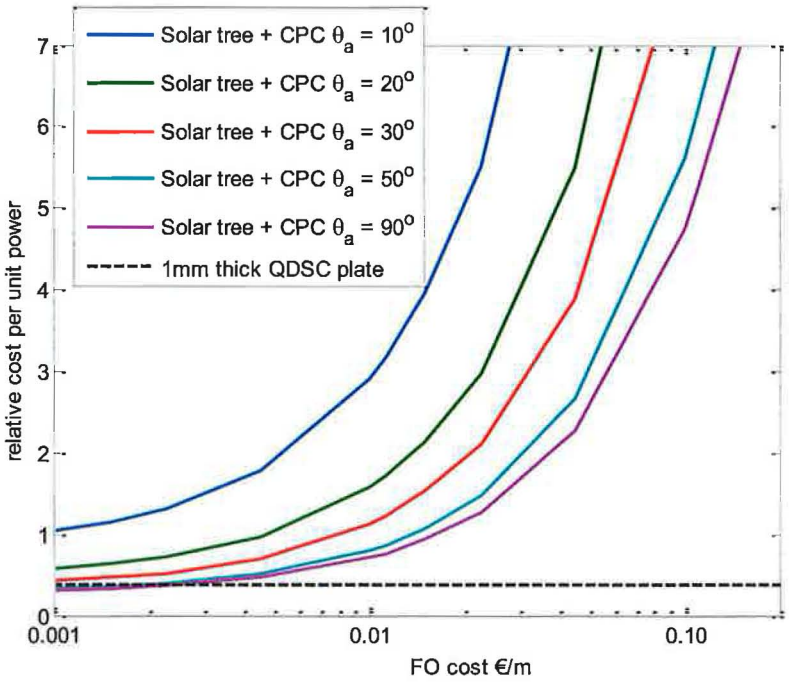

Figure 3.18. The relative cost per unit power of the solar tree with a 2nd stage CPC, for varying CPC acceptance angle, θ_a, and fibre optic (FO) cost. The relative cost per unit power for a 1mm thick single-plate QDSC is given by the black line. At fibre optic costs < €0.01/m the solar tree attains costs per unit power of the same order as the single-plate QDSC.

[vii] Fibre optic transmission losses and the cladding thickness are also assumed to be zero, in order to simplify the analysis.

3.3 Luminescent Down Shifting Layers

A luminescent down-shifting (LDS) layer (Hovel *et al.*, 1979) can enhance the short circuit current density, J_{sc}, of solar cells by transforming the wavelength of incident light from short to longer wavelengths better matching the spectral response of the cell, as shown by the schematic in Figure 3.19. For mc-Si cells, ~2% relative increase in J_{sc} is predicted by Klampaftis *et al.* (2008), using a LDS layer incorporating the optimum combination (at the optimum doping concentration) of the particular organic dyes investigated. A larger increase of 7.5 - 10% is predicted by van Sark *et al.* (2005) using a LDS layer incorporating *QD*s, however. The LSC ray-trace model, described in section 2, is modified to predict the J_{sc} of a mc-Si solar cell attached to a LDS layer. The model is used to investigate whether the optical properties of QDs (i.e. broad absorption range and characteristic increased absorption in the UV and blue wavelength regions) make them a better potential candidate for incorporation in LDS layers than organic dyes. The American Society for Testing and Materials (ASTM, 2003) G-173-03 standard global hemispherical solar spectrum corresponding to air-mass 1.5 (AM 1.5g) is used as the input solar irradiance, following the normal standard for solar cell power conversion efficiency characterization.

Although the results presented here in section 3.3 are for mc-Si cells, it is important to note that LDS layers have been proven to enhance overall conversion efficiencies more significantly with other solar cell types. For example, a 16% increase in efficiency was measured by Richards and McIntosh (2007) for a CdS/CdTe cell. Maruyama and Kitamura (2001) obtained a 36% increase for a CdS/CdTe cell, but with a poorer quality cell with lower EQE in the blue region.

LDS layers have been shown to increase overall conversion efficiencies of organic solar cells (Koeppe *et al.*, 2007), and dye-sensitised solar cells (Liu *et al.*, 2006). Up-converting layers could also be used to convert sub band-gap energy to photons at wavelengths above the PV cell band-gap. However, the efficiency and stability of up-conversion species are not sufficient to realise significant gains in PV cell electrical output.

The main aims of this section are (i) to investigate whether the optical properties of QDs (i.e. broad absorption range and characteristic increased absorption in the UV and blue wavelength regions) make them a more suitable candidate than organic dyes for incorporation in LDS layers, and (ii) to quantify the increase in PV cell power output, using a "partially-covered" LDS layer.

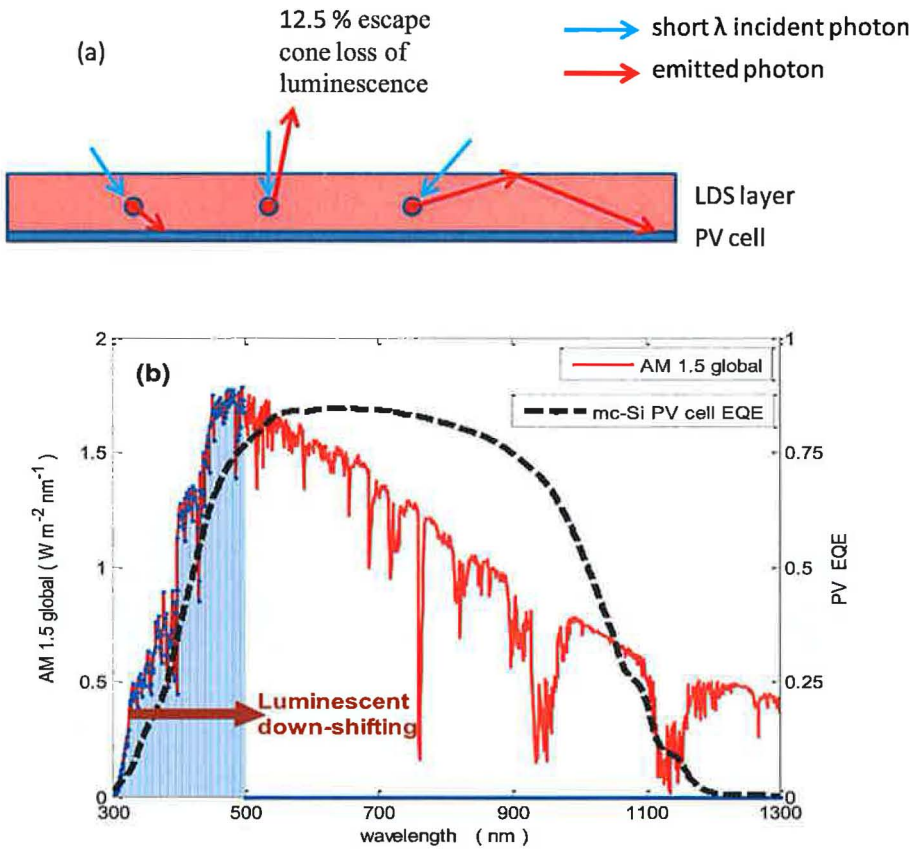

Figure 3.19. The luminescent down-shifting (LDS) layer transforms the wavelength of short wavelength incident photons to wavelengths better matching the EQE response of the mc-Si PV cell attached under the LDS layer.

3.3.1 LDS layers incorporating QDs.

The EQE of a mc-Si solar cell is shown in Figure 3.20. The lower EQE at short wavelengths results from higher emitter recombination in the cell, and higher reflection and absorption of the anti-reflective (AR) coating which is optimised for longer wavelengths (Klampaftis *et al.*, 2009).

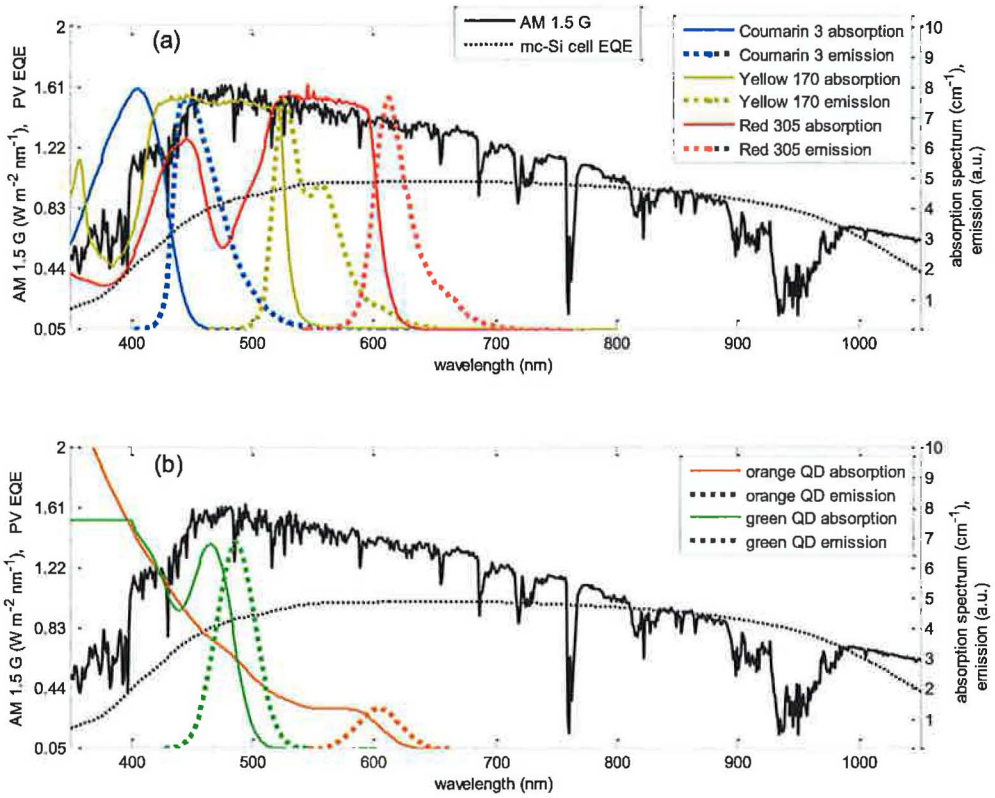

Figure 3.20. (a) Absorption and emission spectra of Coumarin-3-Carboxylic (blue), Perylene Lumogen Yellow 170, Perylene Lumogen Red 305 dyes. Also shown are the mc-Si cell EQE, and global solar spectrum measured at air-mass 1.5. (b) Absorption and emission spectra of two QD types; green emitting CdSe/ZnS QDs, and orange emitting CdSe/ZnS QDs.

LDS layers containing blue Coumarin, yellow Perylene, and red Perylene dyes, and layers containing CdSe/ZnS green-emitting and CdSe/ZnS orange-emitting quantum

dots were simulated using the ray-trace model. The doping concentration of each species can be varied in the model. The optimum absorption spectra and emission spectra of each luminescent species are shown in Figure 3.20. The same luminescent QY (98%) was assumed for each species, in order to compare the near maximum potential of each.

The enhancement in the mc-Si cell J_{sc} using the blue, yellow and red dye doped LDS layers, compared to the reference cell covered with an undoped layer, is 1.01, 1.00, and 0.98, respectively. The enhancement using the green and orange QDs is 1.01 in both cases. The cell EQE for each LDS layer is shown in Figure 3.21. The device EQE is improved by the LDS layers at short incident wavelengths, resulting from incident photons being shifted to wavelengths better matching the cell EQE. The device EQE decreases at longer incident wavelengths, however, as the losses within the layer are greater than the gain attained by shifting the incident photon wavelength. The predicted enhancement of $\leq 1\%$ attained using the *QD* LDS layers is significantly lower than that predicted analytically (van Sark *et al.*, 2005) for similar QD LDS layers (7.5 – 10% enhancement). The van Sark model uses QD absorption and emission spectra, and the incident light spectrum to determine a modified spectrum incident on the PV cell attached underneath the LDS layer. Re-absorption effects are not calculated in the analytic approach, however, thereby overestimating the PV cell short circuit current enhancement (van Sark *et al.*, 2005). The ray-trace approach used here does incorporate the effects of photon re-absorption, and therefore allows a more accurate modified spectrum to be determined. The *PV* model, as described in section 2.3 is a less detailed model than that used by van Sark *et al.*, which also calculates variation in open-circuit voltage and cell fill-factor. However, the *short-circuit current* enhancement is primarily

determined by the modified spectrum and the cell spectral response as given by 2.17. The different PV models used, therefore, are unlikely to account for the differing predictions.

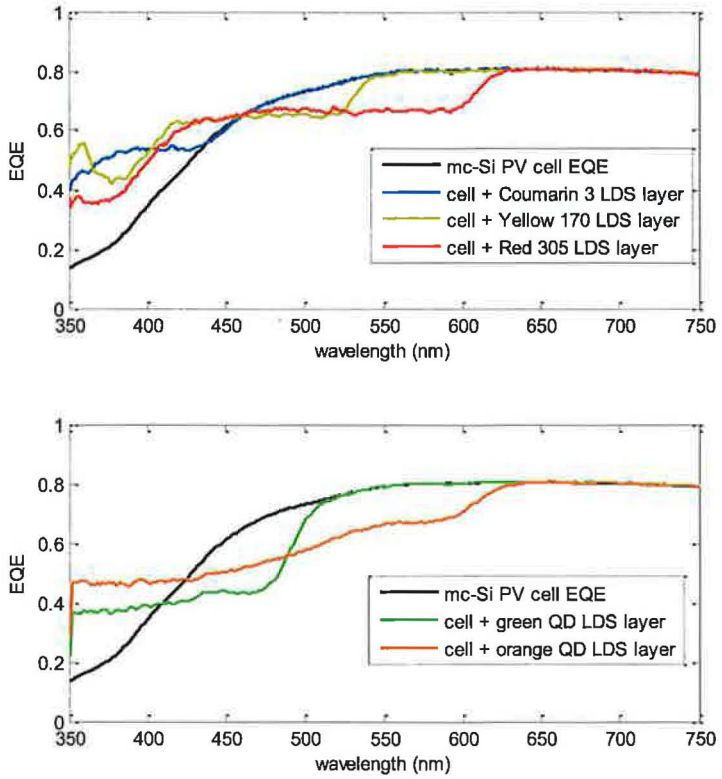

Figure 3.21. EQE of reference mc-Si cell and the cell attached to luminescent down shifting (LDS) layers.

3.3.2 Partially covered LDS layers and comparison with LSCs

A geometric gain is added to the LDS layer, by reducing the area of PV cells attached to the LDS layer, as illustrated in Figure 3.22. The J_{sc} of the active area of PV is enhanced as short wavelength photons are shifted to longer wavelengths better matching the PV cell spectral response. In addition, there is a light concentration effect as photons are transmitted to the cells (from areas of the layer not covered by

PV) via TIR, as shown in Figure 3.22. The configuration has previously been described by Sakuta *et al.* (1994) and Rau *et al.* (2005). Rau's simulated device utilised a photonic structure acting as a spectrally selective reflector (SSR) on the top surface aperture. The devices considered here assume no SSR top layer.

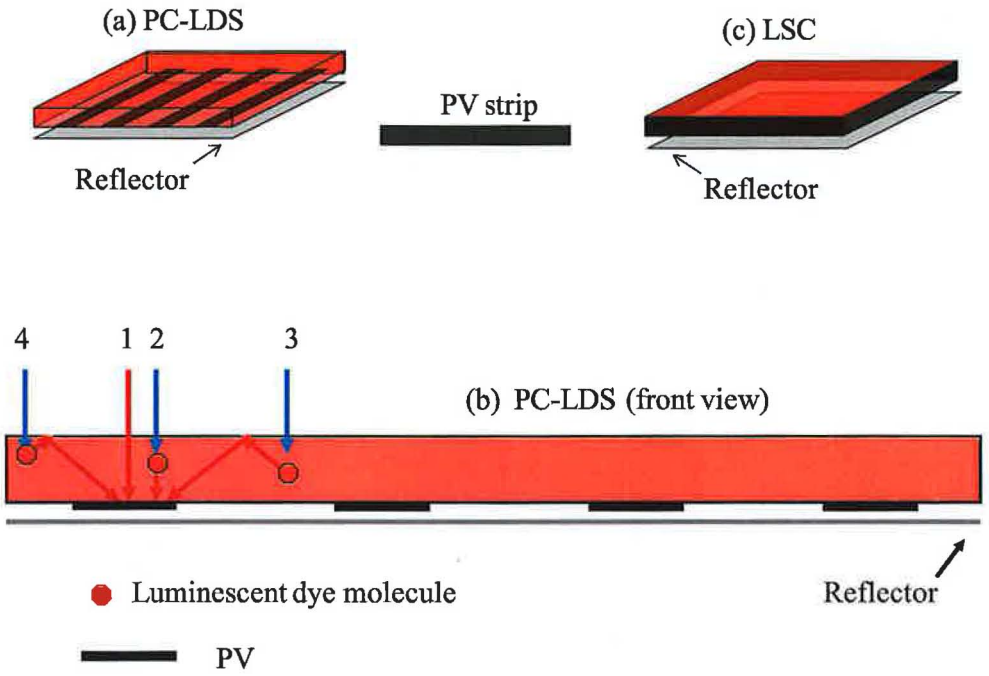

Figure 3.22. (a) In the partially covered luminescent down-shifting layer (PC-LDS), a reduced fraction of the layer is covered by PV cell strips. (b) The PV cell J_{sc} is enhanced as short wavelength photons are shifted to longer wavelengths better matching the PV cell EQE (ray 2), and longer wavelength photons not absorbed by the dye pass through the PC-LDS layer to the PV cell (ray 1). In addition, there is a geometric gain as the layer aperture area is greater than the area of PV. Hence, emitted photons (rays 3 and 4) transmitted to the PV cell via TIR increase the cell J_{sc} compared to a fully covered LDS layer. (c) An LSC configuration employing the same luminescent plate, external reflector, and PV cells as used in (a).

The increase in mc-Si cell J_{sc} using a 10x10 cm "partially covered" luminescent down-shifting (PC-LDS) layer is shown as a function of decreasing coverage fraction for varying luminescent dye types in Figure 3.23. The increase is greatest for the red dye, as it has the broadest absorption range of the three dyes, and, therefore, the light concentration effect is greatest. Reducing the coverage fraction to 10% results in an increase in cell J_{sc} from 30.8 mA/cm^2 to 70 mA/cm^2. The short

circuit current is determined from eqn. 2.15 in this analysis, i.e., reflection at the PV cell is independent from the angle of incidence at the PV surface.

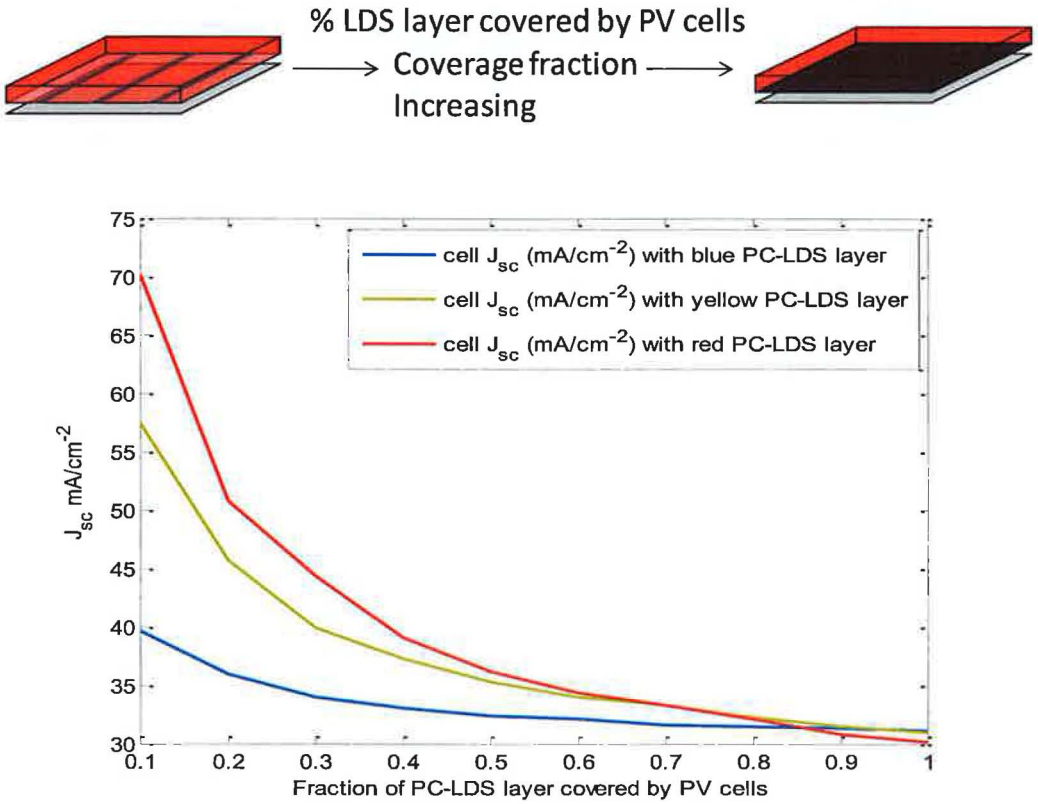

Figure 3.23. J_{sc} (of the active cell area) increases as the fraction of the LDS layer covered by PV cells decreases. The effect is greatest for the red dye, as it has the broadest absorption range of the three dyes, as shown in Figure 3.20. Luminescent QY = 98% and α_{mat} =0.02 cm^{-1} are assumed.

The PC-LDS devices are comprised of the same materials as an LSC, with the PV cells positioned at the bottom surface rather than at the side surfaces, as illustrated in Figure 3.22 (a) and (c). However, the electrical output of the attached PV cells in each configuration may differ. For example, assuming a normally incident AM 1.5 input spectrum, the predicted C for an 8 x 8 cm LSC containing Red 305 dye, with PV cells attached at the four sides, is 1.4. In the PC-LDS configuration, the four PV cells are attached to the bottom of the plate and the predicted concentration ratio increases from 1.4 to 1.9 due to longer wavelength incident photons being transmitted to the cells in the latter case. The material costs

are approximately the same in both the LSC and PC-LDS configurations, however C is ~30% higher in the PC-LDS for these particular dimensions.

C is shown for both the LSC and PC-LDS layer for increasing device size in Figure 3.24(a). For a given top surface aperture area, an equal area of PV cell is used in both device configurations. For smaller plate sizes, predicted C is higher for the PC-LDS configuration. The average pathlength of emitted photons to the PV cells is higher in the PC-LDS layer than in the LSC. Therefore, at larger plate sizes the advantage of using the PC-LDS is counteracted by increased matrix absorption losses and re-absorption losses, and higher C results for the LSC as shown in Figure 3.24(a).

The relative cost per unit power, calculated as in section 3.1.2, is shown in Figure 3.24(b) for both configurations. Both the LSC and PC-LDS layer attain approximately the same minimum relative cost per unit power of ~0.7, which corresponds to a 30% reduction in the cost per W_p compared to the mc-Si cells.

Overall device power conversion efficiency, η, decreases for larger LSC and PC-LDS layer plate sizes. Predicted η, shown in Figure 3.24 (c), is significantly higher for the PC-LDS layer than the LSC, at device sizes corresponding to equivalent costs per unit power. For example, to attain a relative cost per unit power of 0.8, η for the PC-LDS layer is 7.1%, compared to just 3.6% for the LSC, as shown in Figure 3.24(c). This is significant as current single-plate LSCs utilizing mc-Si cells, have low power conversion efficiencies, η, of ~2.5% – 3.5% (depending on G_{gain}[viii]) under standard test conditions (van Sark *et al.*, 2008; Slooff *et al.*, 2008; Pravettoni *et al.*, 2009a), with optimised plates predicted to attain η, of 3.8% for G_{gain}

[viii] Efficiency of LSCs is not a useful comparative measure unless the geometric gain (or concentration ratio attained) is specified, as LSC efficiency is highly dependent on the plate dimensions and number of attached solar cells.

of 10 (van Sark *et al.*, 2008). The ray-trace predictions show that employing the same PV cells and matrix materials in the PC-LDS layer configuration would significantly increase η, as compared to the LSC configuration. It should be noted that if the band-gap of the attached cell was matched better to the spectral range of the absorbing species, the benefit accruing from the PC-LDS layer would diminish. This is because the efficiency increase in PC-LDS layers is primarily due to longer wavelength light, not absorbed by the dye, being transmitted to the PV cells attached underneath.

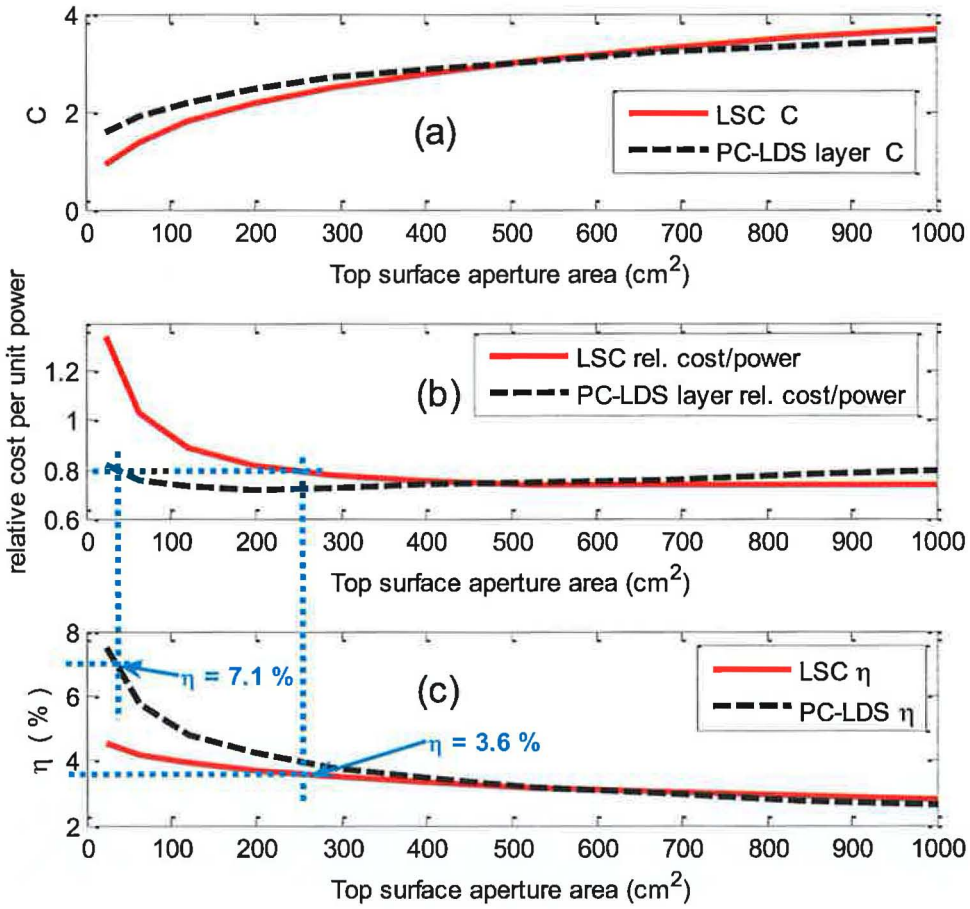

Figure 3.24. (a) The concentration ratio, C, quantifying the relative increase in PV cell J_{sc}, (b) relative cost per unit power, and (c) power conversion efficiency, η, for LSC (red) and PC-LDS (dashed black) layer of varying plate size. Luminescent QY = 98% and α_{mat} =0.02 cm^{-1} are assumed. At a relative cost per unit power of 0.8, η for the PC-LDS layer is ~double η for the LSC, as indicated by the blue lines.

3.4 Chapter conclusions

The effect of varying device geometry and PV cell configurations was investigated using the ray-trace model, concluding that;

- For any given A_{conc}, hexagonal geometries attain higher C than square or triangular geometry.
- Factoring in approximate relative costs of PV cells and QDSC plate material, the relative cost per unit power, for varying geometry type and A_{conc}, can be determined.
- The various geometry types all attain the same minimum cost per unit power if the correct A_{conc} for that particular geometry is selected.
- The correct selection of A_{conc} is critical for attaining the lowest possible cost per W_p. Ray-trace modelling provides an important tool for doing so.
- A non-uniform photon distribution along the QDSC plate edge would result in (1) reduced current through PV cells connected in series along any one plate edge, and/or (2) reduced fill factor for an individual cell attached at that edge. Hexagonal QDSC plates yield a more uniform spatial distribution of photons along the plate edges than rectangular or triangular plates.
- Whether PV cells are (a) attached at all sides of the device, or (b) attached at one side only with external mirrors at other sides, does not affect the minimum cost per unit power. This analysis, however, does not take into account the costs of additional mirrored surfaces required in case (b). Therefore, case (a) is, in fact, a marginally more optimal configuration.
- Higher QD doping concentrations are required for thinner QDSC plates to attain a given η_{abs}, and total re-absorption losses consequently increase. Despite the

increased re-absorption losses, the net effect of thinner QDSC plates is a significant increase in C.

- A tapered plate was proposed in an attempt to reduce QDSC re-absorption losses. The tapered device allows a lower QD doping concentration to be used to attain a given absorption efficiency while maintaining a high geometric gain. The tapered device does not result in higher C, due to an increase in top surface losses.
- A solar tree system, utilizing fibre optics to transmit light from multiple luminescent plates to a single PV cell via a 2^{nd} stage concentrator, was proposed and the relative cost per unit power compared to that of a QDSC. The solar tree does not provide a reduction in relative cost per unit power output, due to the gain of the 2^{nd} stage concentrator being limited by the angular distribution of photons emerging from the fibre optics, and due to the associated costs of the additional system components. If fibre optic costs were significantly reduced compared to current levels, however, then the concept should be further evaluated.
- An increase in mc-Si cell J_{sc} of $\leq$ 1% is predicted, using a *quantum dot* luminescent down-shifting (LDS) layer. The predicted increase is significantly lower than analytical predictions for quantum dot LDS layers in the literature.
- The minimum relative cost per unit power of a partially covered LDS layer is approximately the same as that attained for a LSC device. Power conversion efficiencies, η, of PC-LDS layers were quantified. It was shown that η attained by the PC-LDS layer is greater than that attained by the LSC, at the respective optimum device sizes. This is significant as current LSC η utilizing mc-Si cells under standard test conditions are low (c. 3% at a geometric gain of 10). Employing the same device materials that are used in an LSC in a PC-LDS layer configuration, would significantly increase η without any additional costs.

3.5 References

Anchor Optics, New Jersey, USA, (2009). http://www.anchoroptics.com/catalog/product.cfm?id=354 (last accessed 20/9/09)

Carrascosa, M., Unamuno, S., Agullo-Lopez, F., (1983). Monte-Carlo simulation of the performance of PMMA luminescent solar collectors. *Applied Optics,* 22, 20, 3236-41.

Hinterberger, H., Winston, R., (1966). Efficient Light Coupler for Threshold Cherenkov Counters. *Review of Scientific Instruments,* 37, 1094-5.

Hovel, H.J., Hodgson, R.T., Woodall, J.M., (1979). The effect of fluorescent wavelength shifting on solar cell spectral response. *Solar Energy Materials,* 2, 19-29.

Kandilli, K., Ulgen, K., (2009). Review and modelling the systems of transmission concentrated solar energy via optical fibres. *Renewable and Sustainable Energy Reviews,* 13, 67-84.

Klampaftis, E., Richards, B.S., Wilson, L.R., McIntosh, K.R., Cole, A., Heasman, K., (2008). Improving spectral response of mc-Si cells via luminescent down-shifting of the incident spectrum. *Proceedings of 4th Photovoltaic Science, Applications and Technology Conference*, Bath, UK, 59-62.

Klampaftis, E., Ross, D., McIntosh, K.R., Richards, B.S., (2009). Enhancing the performance of solar cells via luminescent down-shifting of the incident spectrum: A review. *Solar Energy Materials and Solar Cells,* 93, 1182-94.

Koeppe, R., Sariciftci, N.S., Büchtemann, A., (2007). Enhancing photon harvesting in organic solar cells with luminescent concentrators. *Applied Physics Letters,* 90, 1811261-3.

Liu, J., Yao, Q., Li, Y., (2006). Effects of downconversion luminescent film in dye-sensitized solar cells. *Applied Physics Letters,* 88, 17, 173113-9.

Maruyama, T., Kitamura, R., (2001). Transformations of the wavelength of the light incident upon CdS/CdTe solar cells. *Solar Energy Materials and Solar Cells,* 69, 1, 61-8.

Meyer, T., (2007). *Private Communication.*

Ocean Optics, Florida, USA, (2009). http://www.oceanoptics.eu/html/index.php (last accessed 20/9/09)

Pravettoni, M., Pravettoni, F., Virtuani, A., Kenny, R.P., Chatten, A.J., Barnham, K.W.J., (2009). Outdoor characterisation of Luminescent Solar Concentrators and their possible architectural integration on a historically relevant site in Milan (Italy) *Proceedings of 34th IEEE Photovoltaics Specialists Conference*, Philadelphia, USA., to be published.

Rau, U., Einsele, F., Glaeser, G.C., (2005). Efficiency limits of photovoltaic fluorescent collectors. *Applied Physics Letters,* 87, 1711011-3.

Reisfeld, R., Jorgensen, C.K., (1982). Luminescent solar concentrators for energy conversion. *Structure & Bonding,* 49, 1-36.

Richards, B.S., McIntosh, K.R., (2007). Overcoming the poor short-wavelength spectral response of CdS/CdTe photovoltaic modules via luminescence

down-shifting - ray-trace simulations. *Progress in Photovoltaics,* 15, 1, 27-34.

Roncali, J., Garnier, F., (1984). Photon transport properties of luminescent solar concentrators: analysis and optimisation. *Applied Optics,* 23, 16, 2809-17.

Sakuta, K., Sawata, S., Tanimoto, M., (1994). Luminescent concentrator module of a practical size. *Proceedings of 1st World Conference on Photovoltaic Energy Conversion*, Hawaii, USA, 1115-8.

Sidrach de Cardona, M., Carrascosa, M., Messeguer, F., Cusso, F., Jaque, F., (1985). Edge Effect on Luminescent Solar Concentrators. *Solar Cells,* 15, 225-30.

Slooff, L.H., Bende, E.E., Burgers, A.R., Budel, T., Pravettoni, M., Kenny, R.P., Dunlop, E.D., Büchtemann, A., (2008). A luminescent solar concentrator with 7.1% power conversion efficiency. *physica status solidi (RRL) - Rapid Research Letters,* 2, 6, 257-9.

Smyth, M., A., Z., Eames, P.C., Norton, B., (1999). An experimental procedure to determine solar energy flux distributions on the absorber of line-axis compound parabolic concentrators. *Renewable Energy,* 16, 1, 761-4.

van Sark, W.G.J.H.M., Barnham, K.W.J., Slooff, L.H., Büchtemann, A., Meyer, A., McLafferty, J.B., Koole, R., Chatten, A.J., Farrell, D.J., Bose, R., Bende, E.E., Quilitz, J., Kennedy, M., Meyer, T., Wadman, S.H., Meijerink, A., Vanmaekelbergh, D., (2008). Luminescent Solar Concentrators - A review of recent results. *Optics Express,* 16, 26, 21773-92.

van Sark, W.G.J.H.M., Meijerink, A., Schropp, R.E.I., van Roosmalen, J.A.M., Lysen, E.H., (2005). Enhancing solar cell efficiency by using spectral converters. *Solar Energy Materials and Solar Cells* 87, 395-409.

Welford, W.T., Winston, R., (1989). *High collection nonimaging optics.* Academic Press, San Diego, USA.

Winston, R., (1974). Principles of Solar Concentrators of a Novel Design. *Solar Energy,* 16, 89-95.

Winston, R., (1976). Dielectric Compound Parabolic Concentrators. *Applied Optics,* 15, 2, 291-2.

4 Device materials

4.0 Introduction

This chapter investigates the effect of varying QD, matrix material, and external reflector optical properties on QDSC performance. While maximizing QDSC efficiency ultimately remains a materials challenge, modelling can be used to investigate under what circumstances certain goals are possible. For example, what is the minimum quantum yield required for a QDSC to attain a particular concentration ratio or particular power output. Moreover, gains that ensue from changes to device materials in currently realizable QDSCs may not ensue to the same degree in future *higher efficiency* QDSCs. For example, the solar energy concentration ratio, C, of current fabricated low efficiency QDSCs increases by a factor of two with the addition of a diffuse rear reflector in place of a specular rear reflector. Ray-trace modelling was used to show what increase is attained by the inclusion of a diffuse reflector in a *higher efficiency* QDSC.

The ray-trace model was used to determine the effect of varying QD optical properties on concentration ratios. Low QD luminescent quantum yields have limited concentration ratios attained in devices fabricated to-date. QDs with ideal luminescent quantum yields (QY) were modelled to quantify the potential performance of QDSCs, subject to *re-absorption* limitations arising from spectral overlaps between QD emission and absorption spectra.The analysis shows that escape-cone losses account for up to 58% of photons absorbed in a QDSC containing green-emitting QDs, – much higher than the minimum 25% escape cone losses

predicted for a luminescent species with no spectral overlaps in the same plate with a plate refractive index of 1.5[ix]. Higher matrix material refractive index, n, results in reduced escape cone losses but increased external reflection losses. The ray-trace model was used to examine the net effect of varying n and matrix material absorption coefficient, α_{mat}, on QDSC concentration ratios.

Utilizing rear reflectors with diffuse angular reflection results in significantly enhanced C compared to specular reflector types. The effect of varying the external rear reflector type on C is analysed for varying insolation angular distributions. The predictions indicate that the actual *reflectivity* of the reflector used, along with its *cost*, are the most important considerations for a viable QDSC reflector, and not the *type* of reflector used.

A spectrally selective reflector (SSR) top layer, e.g., a thin-film dielectric mirror, can reduce escape-cone losses in the device by reflecting QD emitted light within the angular range of the escape cone, while allowing incident light in the QD absorption range to enter the device. The modelling predictions illustrate why only limited gains have been obtained to date with SSR top layers. Owing to the multiple reflections at the SSR layer, even a small decrease in SSR reflectivity results in significant top surface losses. The ray-trace analysis also demonstrates the critical importance of utilizing a highly reflective *rear* reflector when measuring the performance of any SSR top layer.

[ix] The refractive index of materials typically used in QDSCs fabricated to-date is ~1.5 in the visible wavelength range (400 – 700 nm).

4.1 QD optical properties

One advantage of using QDs over an organic luminescent dye, as the device luminescent species, is the ability to tune a device by varying the quantum dot size to collect specific wavelengths in the solar spectrum (Barnham *et al.*, 2000; Chatten *et al.*, 2003). The optical efficiency (η_{opt}) of currently fabricated QDSCs, however, has been limited by low luminescent quantum yields (QY) and large overlaps between QD emission and absorption spectra (Hyldahl *et al.*, 2009; Rowan *et al.*, 2008 Sholin *et al.*, 2007). Spectral overlap results in QD-emitted photons being re-absorbed in the plate before reaching the PV cell, giving both higher escape cone losses and higher QY losses.

Re-absorption losses in QDSCs containing commercially-available green emitting and orange emitting (CdSe/CdS core-shell) QDs, and laboratory (CdSe CdS/CdZnS/ZnS multi-shell) near infra-red emitting QDs, are quantified. The absorption and emission spectra of the three QD types are shown Figure 4.1. To analyse re-absorption effects solely in terms of escape cone losses, and hence investigate the potential performance of QDSCs subject to spectral overlap limitations, particular device parameters are assumed (Kennedy *et al.*, 2009);

- an ideal QD QY of 100%
- no matrix material absorption or scattering of light emitted by the QD
- perfectly reflecting external mirrors

Model parameter values also assumed are;

- a matrix material refractive index of 1.5
- an incident insolation spectrum corresponding to air-mass 1.5
- a QDSC plate size of 6 x 6 x 0.3 cm

- the spectral response, given in Figure 4.1, of the attached mc-Si solar cell.

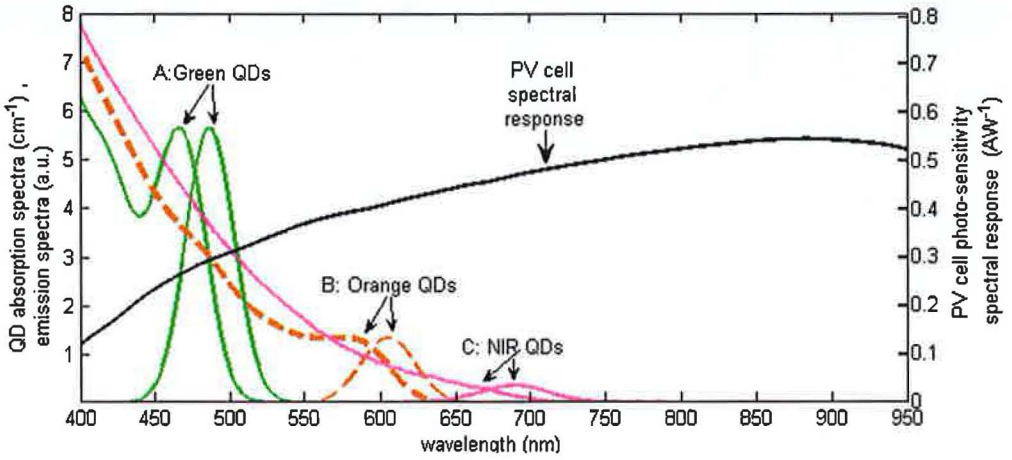

Figure 4.1. Absorption and emission spectra of three QD types. A: Green emitting QDs: CdSe/ZnS, peak emission wavelength (λ_{em}) = 488nm, Nanoco technologies. B: Orange emitting QDs: CdSe/ZnS, λ_{em} = 605nm, Evident technologies. C: NIR emitting QDs: CdSe multi-shell coating CdS/CdZnS/ZnS, λ_{em} = 690 nm, fabricated at Utrecht University, Netherlands, and the mc-Si PV cell photo-sensitivity spectral response.

4.1.1 QDSC absorption efficiency and escape cone losses

The absorption efficiency (η_{abs}) is defined as the fraction of incident photons absorbed on a double-pass through the plate. Predicted η_{abs} of the green, orange and near infra-red (NIR) QDSCs are 11.6%, 21.7% and 23.1%, respectively, as shown in Figure 4.2. η_{abs} is highest in the NIR QDSC due to the broad absorption range. From Figure 4.1, it is noted that the NIR QD absorption coefficient (α_{QD}) at the NIR peak emission wavelength is significantly lower than the orange α_{QD} and green α_{QD} at their respective peak emission wavelengths. A consequence should be comparatively lower re-absorption and associated escape cone losses in the NIR QDSC. In the green, orange and NIR QDSCs, escape cone losses account for, respectively, 58%

±5%[x], 57% ±4%[x], and 43% ±1%[x] of incident photons absorbed in the plate. These losses are much higher than the ~25% minimum escape cone loss predicted for no spectral overlaps, also in a plate of refractive index 1.5 (Batchelder *et al.*, 1979). However, escape cone losses are significantly lower for the NIR QDSC when compared to the green and orange QDSCs. The retention efficiency (η_{ret}) is defined as the fraction of QD emitted photons transmitted to the PV cell. The predicted optical efficiency (η_{opt}), in this ideal case, is thus given by;

$$\eta_{opt} = \eta_{abs}\eta_{ret} \qquad 4.1$$

η_{opt} of the green, orange and NIR QDSCs is 5.0%, 9.3% and 13.2%, respectively, as shown in Figure 4.3. The higher η_{opt} of the NIR QDSC, compared to the orange QDSC, is due partly to the slightly higher η_{abs} but *more significantly* due to lower re-absorption and associated escape cone losses.

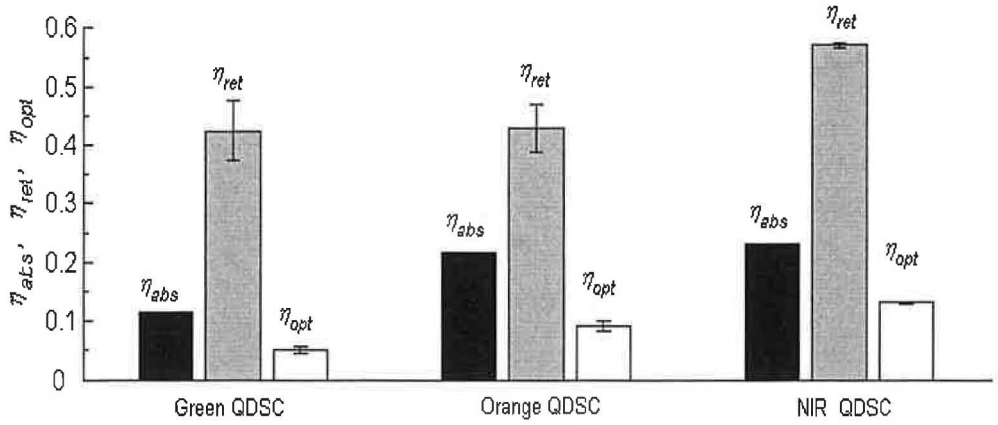

Figure 4.2. Predicted optical efficiency (η_{opt}) of 6 x 6 x 0.3 cm QDSCs containing green, orange and NIR emitting QDs. $\eta_{opt} = \eta_{abs}$ x η_{ret} , where the retention efficiency, η_{ret} = 1-(escape cone loss).

[x] Measured QD emission spectra vary in their peak wavelength, depending on the excitation energy used. The uncertainty in the predicted escape cone losses, arise from the use of only a single emission spectrum in the model.

4.1.2 Solar energy concentration ratios for varying QD quantum yield

Ideal QYs were assumed in section 4.1.1 to analyse re-absorption effects solely in terms of escape cone losses and, hence, investigate the potential performance of QDSCs, subject to spectral overlap limitations. Commercially-available QDs have significantly lower QYs of 30%-50% (Nanonco Technologies, UK; Evident Technologies, USA), however, QD QYs > 85% have been demonstrated (Rogach, 2008). The effect of decreasing QY on predicted concentration ratios, C, is shown in Figure 4.3. Lower QYs have a less detrimental effect on the NIR QDSC, than on the green and orange QDSCs, due to lower re-absorption.

The predicted values of C are compared with that of an efficient organic dye (Lumogen Red305) LSC in Figure 4.3. The Red305 dye has a broad absorption range (from 400 to 600 nm) and a QY of 98% (Boehm, 2008). The estimated QY of these particular NIR CdSe QDs is ~50% (Koole, 2007), yielding a predicted device concentration ratio only 1/3 of that attained by the Red305 dye LSC.

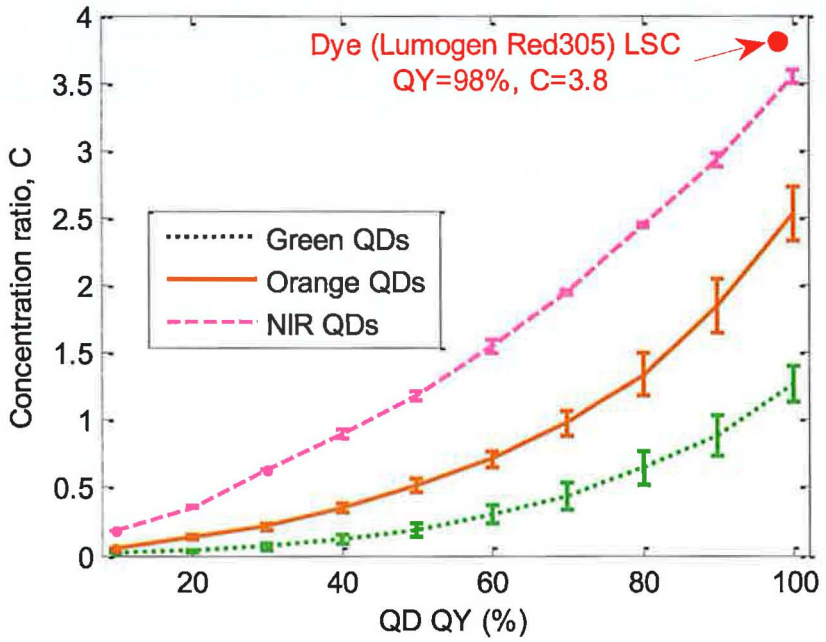

Figure 4.3. Predicted concentration ratios, C, of 6.0 x 6.0 x 0.3 cm QDSCs containing green, orange and NIR emitting QDs of varying quantum yield (QY). The QDSCs concentration ratio is compared with that of a high QY dye LSC.

The results indicate that, even allowing for ideal QD QYs, homogeneously doped single-plate QDSCs containing current commercially-available visible-emitting QDs are unlikely to result in practical devices, due to the large spectral overlaps. The NIR emitting QDs have lower re-absorption losses owing to the shape of the absorption cross-section. Coupled with the broader absorption range, NIR emitting QDs remain potential candidates for viable QDSCs provided higher luminescent QYs are attained.

4.2 Matrix material properties

Multiple characteristics are required for a suitable QDSC matrix material (Gallagher *et al.*, 2007), i.e., low absorption coefficient, solubility with QDs, high luminescence when cast with QDs, chemical durability, non-toxicity, and low cost. The effect of varying the matrix material absorption coefficient, α_{mat}, can be analysed using the ray-trace model. An epoxy resin used in previously fabricated QDSCs has α_{mat} of ~0.04 cm^{-1} across the wavelength range 400-800 nm (Gallagher *et al.*, 2007). Various α_{mat} for dye doped LSC plates are quoted in the literature, ranging from 0.04 cm^{-1} (Burgers *et al.*, 2006), to 0.005cm^{-1} (Thomas *et al.*, 1983, van Sark *et al.*, 2008). Matrix material absorption is wavelength dependent, with increased absorption at UV wavelengths. PMMA, for example, also shows increases at narrow bands in the NIR region due to harmonic vibrations involving the hydrogen atom. (Thomas *et al.*, 1983), For this analysis, α_{mat} is assumed to be wavelength independent over the spectral response range of the attached solar cell (e.g. 300-1200 nm for crystalline silicon solar cells).

The refractive index of the plate, n, is an important parameter in relation to QDSC efficiency. The refractive index of polymer materials commonly used in LSCs is ~1.48 - 1.6. Optical glass with refractive indicies up to 1.82 have been used as substrates in thin-film LSCs (Mulder *et al.*, 2009, Currie *et al.*, 2008). Higher n results in higher retention efficiency, η_{ret}, as escape cone losses are diminished. External reflection losses are increased, however, with higher n. The ray-trace model is used to examine the net effect of varying n (and α_{mat}) on QDSC concentration ratios. Figure 4.4 shows predicted concentration ratios for the QDSC detailed in section 4.1, with varying n and α_{mat}. Increasing the refractive index from 1.5 to 1.7

would increase C by 10% (assuming α_{mat} = 0.01 cm^{-1}). Employing a matrix material with α_{mat} = 0.04 cm^{-1} would decrease C by 35%, compared to a QDSC with α_{mat} = 0.01 cm^{-1} (assuming n = 1.5).

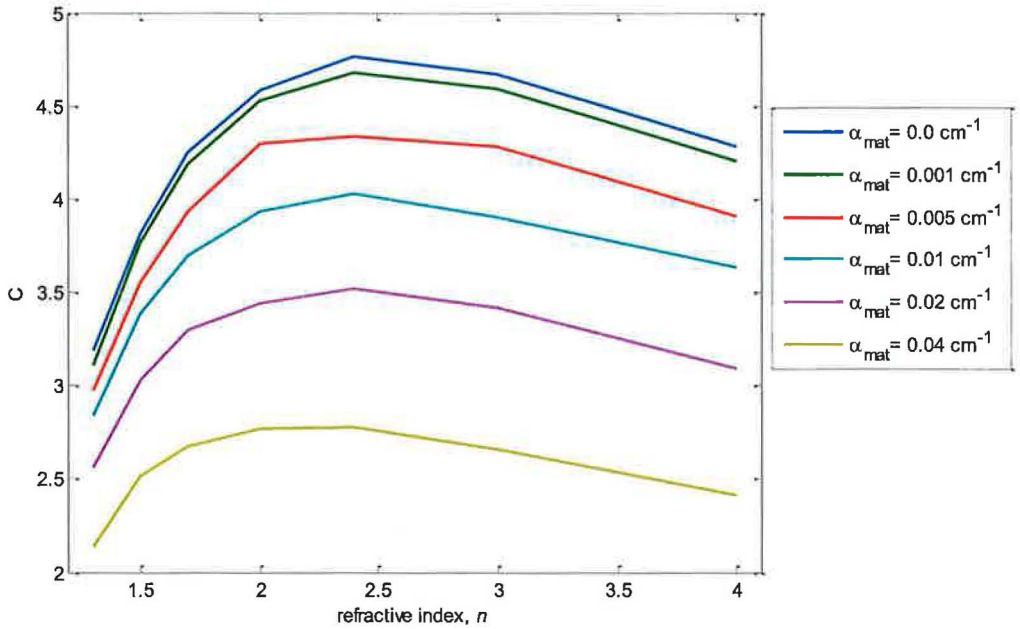

Figure 4.4. QDSC Concentration ratio for varying plate refractive index, n, and matrix material absorption coefficients, α_{mat}.

The results clearly highlight the importance of maintaining α_{mat} as low as possible, with significant gains achievable with lower α_{mat}. Attempts to increase device efficiency by increasing n must consider the effect of any variation in α_{mat}. It is noted that C has been predicted for normal incidence. While the variation in C (and hence, in device power conversion efficiency ratings) are representative of those attainable under standard test conditions, realistic external reflection losses would be higher in outdoor conditions with increased insolation incident angles. Therefore, the effect of varying n on outdoor annual energy yields is examined in section 5 using more realistic solar radiation modelling.

4.3 Specular and diffuse rear reflectors types

In this section, the effect of rear reflector *type* (i.e., whether the reflector type is diffuse or specular) on C is analysed using the ray-trace model. Under normally incident light, device C may increase with the inclusion of a diffuse reflector through two mechanisms (Kennedy *et al.*, 2007);

(a) With a diffuse reflector, the initial pathlength of normally incident light on a double-pass through the plate is increased, as illustrated in Figure 4.5, resulting in a higher absorption efficiency.

(b) Normally incident light not absorbed in the plate may be reflected onto the attached PV cell when a diffuse rear reflector is utilised, whereas utilizing a specular reflector this does not occur.

Varying relative increases are reported in the literature. Rowan *et al.* (2007) observed more than 100% increases in C, whereas Burgers *et al.* (2005) measured an increase of ~25% for an LSC employing a diffuse reflector, compared to the same device with a specular reflector.

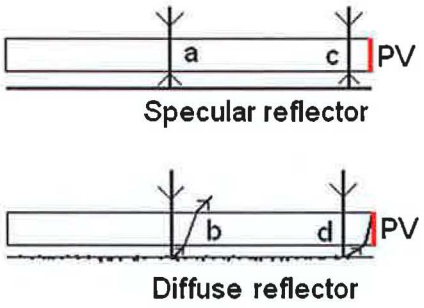

Figure 4.5. For direct normal incidence, there is an increased average pathlength using a diffuse reflector(b) compared to a specular reflector(a), resulting in a higher absorption efficiency. Moreover, there is a probability that incident light will be reflected directly onto the PV cell using a diffuse reflector(d), but not using a specular reflector(c).

C is calculated for the NIR QDSC, described in section 4.1, assuming a diffuse rear reflector in place of the specular rear reflector used therein. A Lambertian angular distribution, with an ideal reflectivity, is assumed for the diffuse reflector. Two insolation incident angular distributions are considered - (i) direct normal to the QDSC top surface, and (ii) isotropic diffuse insolation. An air-gap is assumed to exist between the plate and external reflectors allowing TIR to occur at this boundary. Higher device efficiencies ensue with an air-gap, as η_{TIR} is greater than the reflector reflectivity (Debije *et al.*, 2009).

As shown by the ray-trace predictions in Figure 4.6(a), the potential increase in C from a diffuse rear reflector depends on the QD QY. Assuming a QD QY of 20%, for example, the diffuse reflector results in a 60% relative increase in predicted C. Assuming a QD QY of 90%, however, only a 15% relative increase in C ensues. This explains the varying results presented in the literature with lower relative increases accruing in more efficient devices. In overcast outdoor conditions the sky undertakes the role of the diffuser, negating the advantages of the diffuse reflector outlined above for normally incident light (Sidrach de Cardona *et al.*, 1985b). There is no significant difference in predicted C assuming isotropic diffuse insolation, as shown in Figure 4.6(b). These results indicate that the actual *reflectivity* of the reflector used, along with its *cost*, are the most important considerations for a viable QDSC reflector, and not the *type* of reflector used.

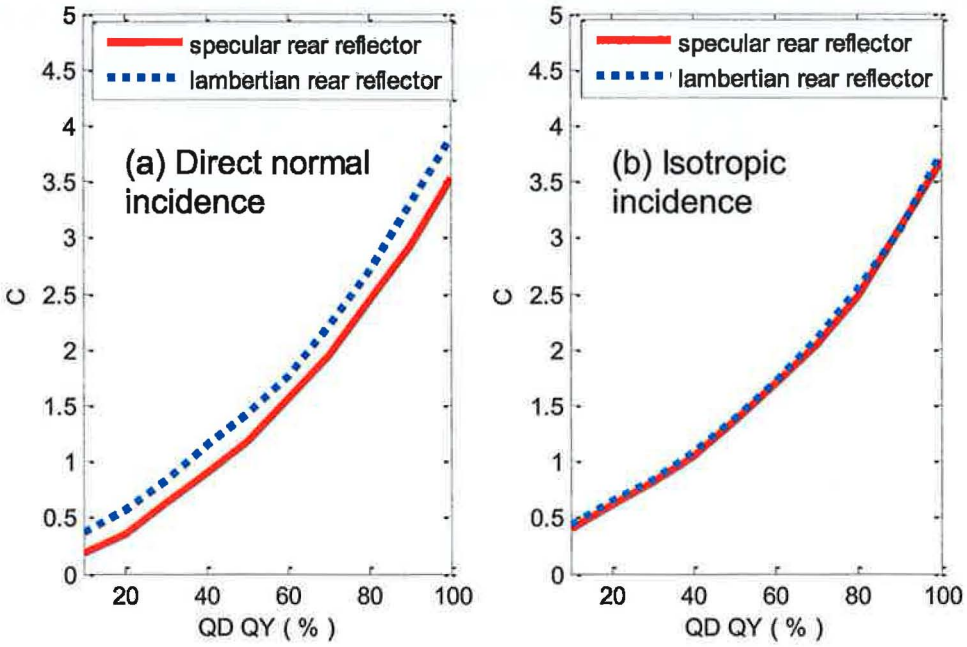

Figure 4.6. Predicted C for QDSC assuming external specular (red line) and Lambertian (dashed blue line) rear reflectors for (a) direct normal, and (b) isotropic diffuse incident insolation.

4.4 Spectrally selective reflecting top layers

Spectrally selective reflector (SSR) top layers can reduce the escape-cone losses in the device by reflecting QD emitted light within the angular range of the escape cone, while allowing light in the QD absorption range to enter the device (Smestad *et al.*, 1990). With a perfectly reflecting SSR, Rau *et al.* (2005) have shown that LSC efficiency can approach that of the maximum possible for a single junction solar cell. "Hot mirrors" were proposed as SSR layers by Richards *et al.* (2004), but no increase in overall efficiency was observed with the particular hot mirror used. Rugate filters (Goldschmidt *et al.*, 2006) resulted in an 11% increase in LSC internal optical efficiency due to the reduction in escape-cone losses. However, the gains were negated by partial transmission losses, reflection of short wavelength incident light, and scattering at the filter surface. More recent prototypes have demonstrated a 20% increase in device efficiency with the inclusion of a Rugate filter (Goldschmidt *et al.*, 2009). Cholesteric liquid crystal coatings have also been proposed (Chatten *et al.*, 2007), however no significant increase (within the experimental error) was found using the cholesteric reflector on two dye LSC plates, compared to control samples without the cholesteric reflector, due to reflection of short wavelength light negating the advantage of reduced escape cone losses.

In section 4.4.1, the cut-off wavelength of the SSR modelled is optimised for the particular luminescent species used. An ideal cut-off and zero transmission losses are assumed for the SSR. Emitted photons exiting the device through the escape-cone are reflected by the SSR layer. However, multiple reflections are required at the SSR layer interface (and at the rear reflector) before the photon is transmitted to the plate edges and, therefore, even a small decrease is SSR reflectivity, R_{SSR}, may result in a

significant overall top surface losses. In sections 4.4.2 and 4.4.3, the ray-trace model is used to investigate the effect of reduced R_{SSR} and rear reflector reflectivity on device concentration ratios.

4.4.1 SSR cut-off wavelength optimisation

Assuming a diffuse rear reflector with a reflectivity of 0.98, a concentration ratio of 3.8 is predicted for the 6 x 6 x 0.3 cm QDSC detailed in section 4.3. Top surface escape cone losses account for 41% of incident photons absorbed in the QDSC. A SSR top layer with a reflectivity of 0.999 is incorporated into the ray-trace model of the QDSC. An-air gap is assumed between the SSR layer and the QDSC top surface, which allows TIR to occur for incident light within the angular range. To simplify calculations, transmission losses through the SSR layer are assumed to be zero. In SSR layers the reflectivity is found to blue-shift with higher angles of incidence (Richards *et al.*, 2004). However, for this preliminary analysis, reflectivity is assumed to be angle independent.

The SSR reflection/transmission cut-off wavelength (λ_{co}), shown in Figure 4.7, is varied and the resulting device concentration ratio calculated. Using a shorter λ_{co}, more QD emitted light escaping the top surface is reflected, but a larger fraction of the incident light is also reflected from the device. With a longer λ_{co}, less QD emitted light is reflected, but more of the incident light enters the device. Predicted C for varying λ_{co} is shown in Figure 4.8, with an optimum λ_{co} of 655 nm predicted for this particular QDSC. The analysis shows that it is critical to optimise λ_{co} for the particular optical properties of the luminescent species used.

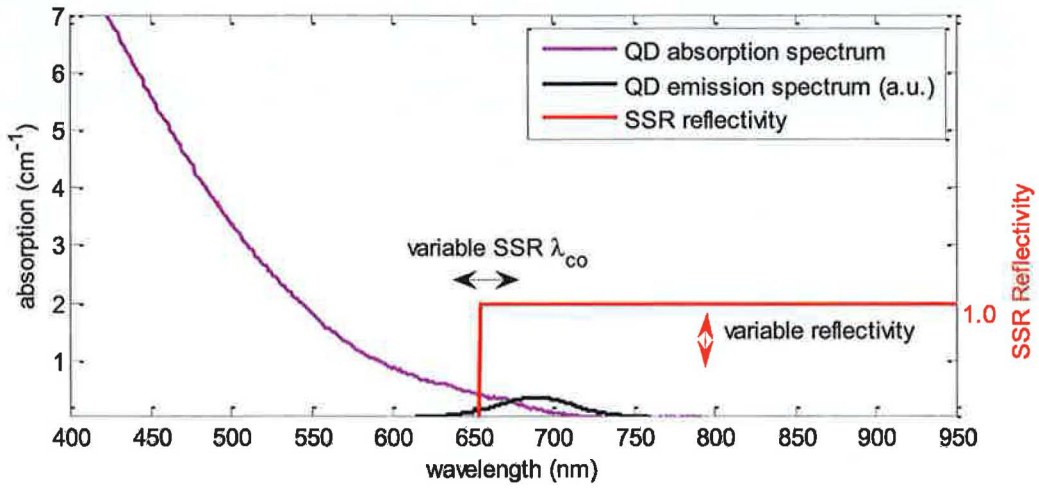

Figure 4.7. A spectrally selective reflector (SSR) with angle-independent reflectivity and ideal "cut-off" between reflection and transmission wavelength regions is modelled.

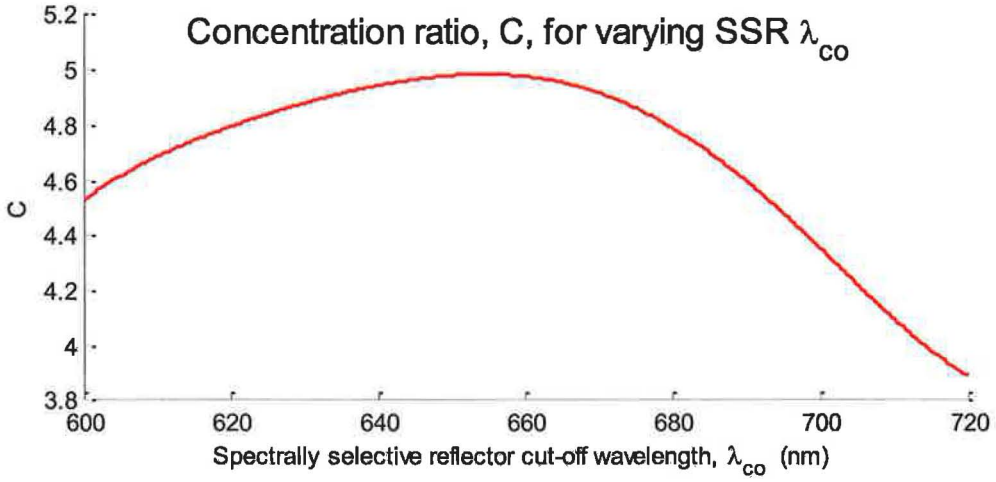

Figure 4.8. Predicted QDSC concentration ratio, C, for varying spectrally selective reflector layer cut-off wavelength, λ_{co}.

4.4.2 Top surface losses for varying SSR reflectivity

As shown in Figure 4.9(a), a concentration ratio of 5.0 is predicted for the particular QDSC assuming an R_{SSR} of 0.999. The top surface losses are reduced from 41% (without an SSR) to 2%. The effect of reduced R_{SSR} on top surface losses is shown in Figure 4.9(b). For example, assuming reduced R_{SSR} of 0.95 and 0.85, the total top surface losses increase (from 2%) to 19% and 29%, respectively. The modelling predictions partly explain why only limited gains have been obtained to date with many SSR top layers. Owing to the multiple reflections at the SSR layer, even a small decrease in R_{SSR} results in significant overall top surface losses.

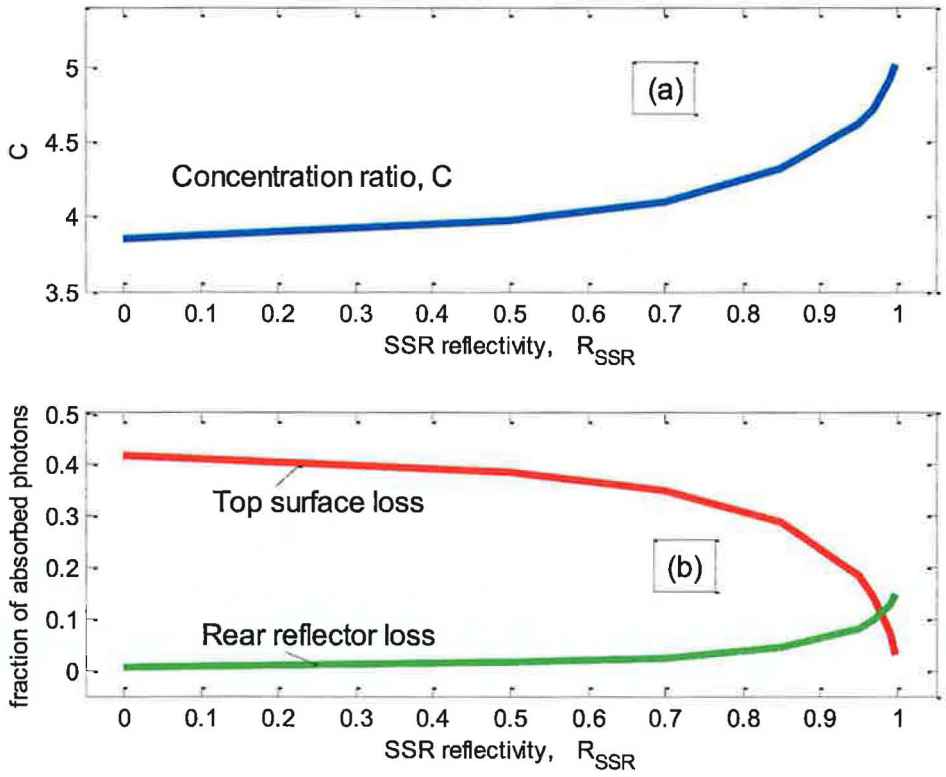

Figure 4.9. (a)Variation in concentration ratio, C, with increasing spectrally selective reflector (SSR) reflectivity. (b)Top surface losses decrease with higher SSR reflectivity, however, rear reflector (R_{Mirror}=0.98) losses increase.

4.4.3 Effect of rear reflector reflectivity

Figure 4.10 shows the effect of variation in *rear reflector* reflectivity, R_{Mirror}, on C of QDSCs[xi] with, and without, a near-ideal SSR top layer with R_{SSR} of 0.999. Relatively small decreases in R_{Mirror} significantly affect the potential gain in C. Even though R_{SSR} is close to ideal, the multiple reflections required at the rear reflector before photons are transmitted to the plate edges results in significant reductions in C when $R_{Mirror} < 1.0$. The results highlight the importance of utilizing a highly reflective *rear* reflector when measuring the performance of any SSR top layer.

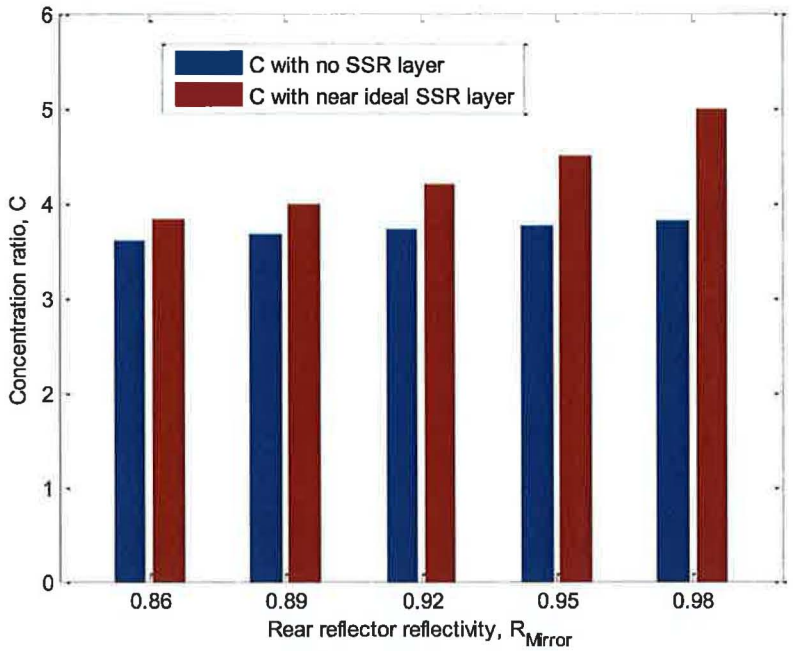

Figure 4.10. Predicted concentration ratio, C, for increasing rear reflector reflectivity, R_{Mirror}. The QDSCs modelled assume a near-ideal spectrally selective reflector (SSR) top layer with reflectivity of 0.999. Relatively small decreases in R_{Mirror} significantly affect the potential gain in C attained an SSR layer. The results highlight the importance of utilizing a highly reflective *rear* reflector when measuring the performance of any SSR top layer.

[xi] The other QDSC parameters are as detailed above in section 4.1.

4.5 Chapter conclusions

While maximizing QDSC efficiency ultimately remains a materials challenge, modelling can be used to investigate under what circumstances certain goals are possible. The effect of varying QD, matrix material, and external reflector optical properties on QDSC performance has been investigated.

- Escape cone losses account for 58% and 57% of incident photons absorbed in the green and orange QDSCs modelled, respectively. This is much higher than the ~25% minimum escape cone loss assuming a luminescent species with no spectral overlaps in the same plate. Predicted escape cone losses are reduced to 43% for the QDSC incorporating NIR QDs.
- Even allowing for ideal QYs, commercially-available visible-emitting QDs are not suitable candidates for inclusion in viable QDSCs, due to spectral overlaps and the resulting re-absorption losses. The NIR emitting QDs have lower re-absorption losses owing to the shape of the absorption cross-section. Coupled with the broader absorption range, NIR emitting QDs remain potential candidates for viable QDSCs, provided higher luminescent QYs are attained.
- Higher matrix material refractive index, n, results in reduced escape cone losses but increased external reflection losses. The ray-trace model was used to examine the net effect of varying n and matrix material absorption coefficient, α_{mat}, on C of a particular 6 x 6 x 0.3 cm QDSC. For example, increasing n from 1.5 to 1.7 would increase C by 10% (assuming α_{mat} = 0.01 cm^{-1}). Employing a matrix material with α_{mat} = 0.04 cm^{-1} would decrease C by 35%, compared to a QDSC with α_{mat} = 0.01 cm^{-1}. The results clearly highlight the importance of maintaining α_{mat} as low as possible, with significant gains achievable with lower α_{mat}. Attempts

to increase device efficiency by increasing n must consider the effect of any variation in α_{mat}.

- Under direct normal insolation, the advantage of employing a diffuse rear reflector reduces with more efficient QDSCs. There is no significant difference in predicted C assuming isotropic diffuse insolation. The results indicate that the actual *reflectivity* of the reflector, and its *cost*, are the most important considerations for a viable QDSC reflector, and not the reflector *type*.
- The ray-trace model is an important tool for determining the optimum cut-off wavelength of a spectrally selective reflector (SSR) top layer.
- The effect of reduced SSR reflectivity, R_{SSR}, and rear reflector reflectivity on device concentration ratios was analysed. The modelling predictions partly explain why limited gains have been obtained experimentally to date with many SSR top layers. Owing to the multiple reflections at the SSR layer interface, even a small decrease in R_{SSR} results in significant top surface losses. For the same reason, it is of critical importance to utilise a highly reflective *rear* reflector when measuring the performance of any SSR *top* layer.

4.6 References

Barnham, K.W.J., Marques, J.L., Hassard, J., O'Brien, P., (2000). Quantum dot concentrator and thermodynamic model for the global redshift. *Applied Physics Letters,* 76, 9, 1197-9.

Batchelder, J.S., Zewail, A.H., Cole, T., (1979). Luminescent solar concentrators. 1:Theory of operation and techniques for performance evaluation. *Applied Optics,* 18, 18, 3733-54.

Boehm, A., ColorFlex GmbH & Co., Germany, (2008). *Private Communication.*

Burgers, A.R., Slooff, L.H., Büchtemann, A., Van Roosmalen, J.A.M., (2006). Performance of single layer Luminescent Concentrators with multiple dyes. *Proceedings of 4th World Conference on Photovoltaic Energy Conversion*, Hawaii, USA, 198-201.

Burgers, A.R., Slooff, L.H., Kinderman, R., Van Roosmalen, J.A.M., (2005). Modelling of Luminescent Concentrators by Ray-tracing. *Proceedings of 20th European Photovoltaic Solar Energy Conference*, Barcelona, Spain, 394-7.

Chatten, A.J., Barnham, K.W.J., Buxton, B.F., Ekins-Daukes, N.J., Malik, M.A., (2003). A new approach to modelling quantum dot concentrators. *Solar Energy Materials and Solar Cells,* 75, 3-4, 363-71.

Chatten, A.J., Farrell, D.J., Bose, R., Debije, M.G., Büchtemann, A., Barnham, K.W.J., (2007). Thermodynamic modelling of luminescent solar concentrators with reduced top surface losses. *Proceedings of 22nd European Photovoltaic Solar Energy Conference and Exhibition*, Milan, Italy, 349-53.

Currie, M., Mapel, J.K., Heidel, T.D., Goffri, S., Baldo, M.A., (2008). High-Efficiency Organic Solar Concentrators for Photovoltaics. *Science,* 321, 226-8.

Debije, M.G., Teunissen, J., Kastelijn, M.J., Verbunt, P.P.C., Bastiaansen, C.W.M., (2009). The effect of a scattering layer on the edge output of a luminescent solar concentrator. *Solar Energy Materials and Solar Cells,* 93, 1345-50.

Gallagher, S.J., Rowan, B.C., Doran, J., Norton, B., (2007). Quantum dot solar concentrator: Device optimisation using spectroscopic techniques. *Solar Energy,* 81, 4, 540-7.

Goldschmidt, J., Glunz, S.W., Gombert, A., Willeke, G., (2006). Advanced Fluorescent Concentrator. *Proceedings of Proceedings of 21st European Photovoltaic Conference,* Dresden, Germany, 107-10.

Goldschmidt, J., Peters, M., Bosch, A., Helmers, H., Dimroth, F., Glunz, S.W., Willeke, G., (2009). Increasing the efficiency of fluorescent concentrator systems. *Solar Energy Materials and Solar Cells,* 93, 176-82.

Hyldahl, M.G., Bailey, S.T., Wittmershaus, B.P., (2009). Photo-stability and performance of CdSe/ZnS quantum dots in luminescent solar concentrators. *Solar Energy,* 83, 566-73.

Kennedy, M., McCormack, S.J., Doran, J., Norton, B., (2007). Ray-trace modelling of reflectors for Quantum Dot Solar Concentrators. *Proceedings of SPIE Optics and Photonics and Solar Energy Conference*, San Diego, USA, (CD).

Kennedy, M., McCormack, S.J., Doran, J., Norton, B., (2009). Improving the optical efficiency and concentration of a single-plate quantum dot solar concentrator using near infra-red emitting quantum dots *Solar Energy,* 83, 7, 978-81.

Koole, R., (2007). *Private Communication.*

Mulder, C.L., Theogarajan, L., Currie, M., Mapel, J.K., Baldo, M.A., Vaughn, M., Willard, P., Bruce, B.D., Moss, M.W., McLain, C.E., Morseman, J.P., (2009). Luminescent solar concentrators employing phycobilisomes. *Advanced Materials,* 21, 1-5.

Rau, U., Einsele, F., Glaeser, G.C., (2005). Efficiency limits of photovoltaic fluorescent collectors. *Applied Physics Letters,* 87, 1711011-3.

Richards, B.S., Shalav, A., Corkish, P., (2004). A Low Escape-Cone-Loss Luminescent Solar Concentrator. *Proceedings of Proceedings of 19th European Photovoltaic Solar Energy Conference*, Paris, France, 113-6.

Rogach, A.L., (2008). *Semiconductor nanocrystal quantum dots: synthesis, assembly, spectroscopy.* Springer-Verlag/Wien, Austria.

Rowan, B.C., (2007). PhD Thesis: The Development of a Quantum Dot Solar Concentrator. School of Physics, Dublin Institute of Technology, Dublin.

Rowan, B.C., Wilson, L.R., Richards, B.S., (2008). Advanced material concepts for luminescent solar concentrators. *IEEE Journal of Selected Topics In Quantum Electronics,* 14, 5, 1312-22.

Sholin, V., Olson, J.D., Carter, S.A., (2007). Semiconducting polymers and quantum dots in luminescent solar concentrators for solar energy harvesting. *Journal of Applied Physics,* 101, 1231141-9.

Sidrach de Cardona, M., Carrascosa, M., Messeguer, F., Cusso, F., Jaque, F., (1985). Outdoor evaluation of luminescent solar concentrator prototypes. *Applied Optics,* 24, 13, 2028-32.

Smestad, G.P., Ries, H., Winston, R., Yablonovitch, (1990). The thermodynamic limits of light concentrators. *Solar Energy Materials,* 21, 99-111.

Thomas, W.R.L., Drake, J.M., Lesiecki, M.L., (1983). Light transport in planar luminescent solar concentrators: the role of matrix losses. *Applied Optics,* 22, 21, 3440-9.

van Sark, W.G.J.H.M., Barnham, K.W.J., Slooff, L.H., Büchtemann, A., Meyer, A., McLafferty, J.B., Koole, R., Chatten, A.J., Farrell, D.J., Bose, R., Bende, E.E., Quilitz, J., Kennedy, M., Meyer, T., Wadman, S.H., Meijerink, A., Vanmaekelbergh, D., (2008). Luminescent Solar Concentrators - A review of recent results. *Optics Express,* 16, 26, 21773-92.

5 Outdoor modelling of LSCs

5.0 Introduction

The performance of LSCs can vary over the course of a given day due to variation in:

- the incident insolation spectrum due to changes in air mass and atmospheric conditions;
- the diffuse fraction of total incident insolation;
- the skyward distribution of the diffuse insolation component;
- albedo radiation, from the ground or from adjacent buildings, which may be incident on the LSC plane.

Mansour *et al.* (2002) and El-Shaarawy *et al.* (2007) obtained higher efficiencies and concentration ratios for fixed plate LSCs in morning and evening times, compared to those obtained at mid-day. This was attributed to the higher diffuse component of the insolation available at those times (Mansour *et al.*, 2002). The effect of varying tilt angle was also found to have a significant effect on overall power output. El-Shaarawy *et al.* found the optimum LSC tilt angle to be 16° during summer testing at a particular location in Egypt (latitude 31°). In a year long LSC outdoor field trial also at a location in Egypt, Salem *et al.* (2000) determined the relative seasonal increase in average power output for LSCs employing two-axis tracking compared to an LSC at varying fixed tilt angles, concluding that tracking was not beneficial for LSC systems due to the additional capital and operational costs. Pravettoni *et al.* (2009b) measured the diurnal variation in LSC electrical output over two separate

days at a location in Italy. Increases in efficiency were noted a) when the diffuse component increased due to short-term cloud cover, and b) at morning and evening times when light was incident at higher angles. Indoor testing has also demonstrated higher efficiencies at higher incidence angles (Pravettoni *et al.*, 2009a).

The ray-trace model was used to investigate the outdoor performance of a QDSC in a climate with a large diffuse component of insolation at a location in Dublin, Ireland (53°N). Monthly averaged hourly spectral irradiance and incident angle distributions on a tilted QDSC plate were determined from horizontal irradiance measurements. Using the hourly data as input to the ray-trace model the following were investigated;

- the diurnal variation in QDSC concentration ratio,
- the effect of tilt angle and solar tracking on QDSC outdoor performance,
- the effect of varying the QDSC plate refractive index on annual energy yield,
- the effect of an anti-reflective coating in minimizing external reflection losses and increasing annual energy yield.

5.1 Solar radiation modelling

Variation of the global irradiance on a tilted surface, G_t, is required to model the outdoor performance of a QDSC. G_t, is given by the sum of the beam, B_t, diffuse, D_t, and ground albedo reflected, R_t, irradiance components;

$$G_t = B_t + D_t + R_t \qquad 5.1$$

Global horizontal irradiance, G_h, from which B_t, D_t, and R_t can be determined, was measured at the Dublin Institute of Technology, Ireland (53° N, 6° W), at five minute intervals over the year January to December, 2008. A diffuse-global correlation model (Mondol *et al.*, 2008) is used to predict the horizontal diffuse and beam irradiance components, D_h and B_h, from G_h. The beam and ground reflected components on a tilted surface, B_t and R_t are easily determined from B_h and G_h, respectively, with knowledge of the solar geometry and the plane tilt and orientation. Determining D_t is less straightforward as, ideally, an accurate angular distribution of the diffuse component is required to determine the diffuse irradiance on any given tilted surface. The semi-empirical Perez slope irradiance model (Perez *et al.*, 1987; Perez *et al.*, 1990) is used to predict D_t from D_h. Sections 5.1.1 - 5.1.6 detail the methods used to obtain the spectral irradiance on a tilted surface, required as ray-trace model input. All solar irradiance data and results are presented in solar time. Solar time describes the angular motion of the sun across the sky at a particular location, with solar noon occurring when the sun reaches maximum altitude as observed from that location. Appendix B details how to convert from local standard time to solar time.

5.1.1 Beam and diffuse horizontal irradiance

Extraterrestrial global horizontal irradiance, E_h, is the irradiance a horizontal surface would receive in the absence of any clouds or atmosphere around the earth and is given by;

$$E_h = I_0 \cos\theta_s \qquad 5.2$$

where I_0 is the solar constant. I_0, measured outside the earth's atmosphere, varies slightly throughout the year and instrumentation uncertainty is also a factor in determining I_0 (Liou, 2002). An annual average value of $1366 \pm 3 W/m^2$ is quoted by Lean and Rind (1998) for I_0. A constant value of 1366 W/m^2 is assumed for irradiance calculations.

The clearness index, k_T, an indicator of the relative clearness of the atmosphere is given by;

$$k_T = G_h / E_h \qquad 5.3$$

Increased cloud cover and/or sky turbidity [xii] decreases the measured global irradiance, G_h, yielding a lower clearness index. The diffuse fraction, k_D, of hourly irradiance is correlated with k_T, and can therefore be determined from measured hourly G_h data. The Mondol diffuse-global correlation model (Mondol *et al.*, 2008) is given by;

$$\begin{aligned} k_D &= 0.98 && \text{for} \quad k_T \le 0.2 \\ k_D &= 0.61092 + 3.6259 k_T - 10.171 k_T^2 + 6.338 k_T^3 && \text{for} \quad 0.2 < k_T \le 0.7 \\ k_D &= 0.672 - 0.474 k_T && \text{for} \quad k_T > 0.7 \end{aligned} \qquad 5.4$$

The Mondol model was found to predict k_D more accurately than two other diffuse-global correlation models (Erbs *et al.*, 1982; Reindl *et al.*, 1990) when compared with measurements taken over a 33 month period at a location in Northern Ireland at latitude 54° N (Mondol *et al.*, 2008). Mean hourly D_h, (and B_h) were calculated for

[xii] due to absorption of solar irradiance by water vapour or scattering by aerosol particles

each calendar month of 2008. Predictions for January and July are shown in Figure 5.1. D_h is significantly greater than B_h in both months. The total annual horizontal diffuse fraction at the location (Dublin, Ireland), was 0.77. LSCs, with limited absorption ranges, operate more efficiently in diffuse light conditions as a higher fraction of the incident irradiance is within the absorption range (Goetzberger, 1978).

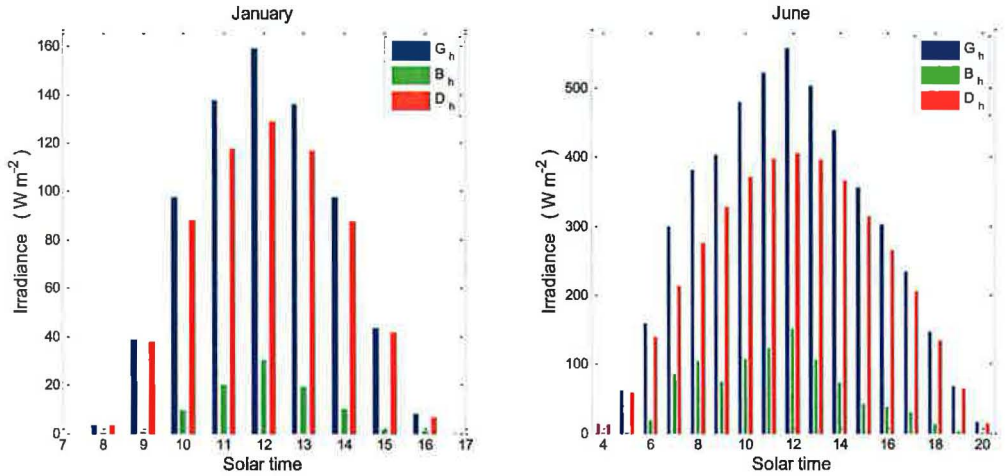

Figure 5.1. The measured mean hourly global horizontal irradiance, G_h, and predicted mean hourly horizontal beam irradiance, B_h, and diffuse irradiance, D_h, for the months January and June, 2008.

5.1.2 Solar geometry

The position of the sun is defined by the solar zenith angle, θ_s, and the solar azimuth angle, γ_s, as shown in Figure 5.2. The 15th day of each calendar month is taken as an approximate "mean day", representative of the solar path of all days in that month. The solar path, describing hourly θ_s and γ_s, for the mean day of months January to June, at a location 53° N, is shown in Figure 5.3.

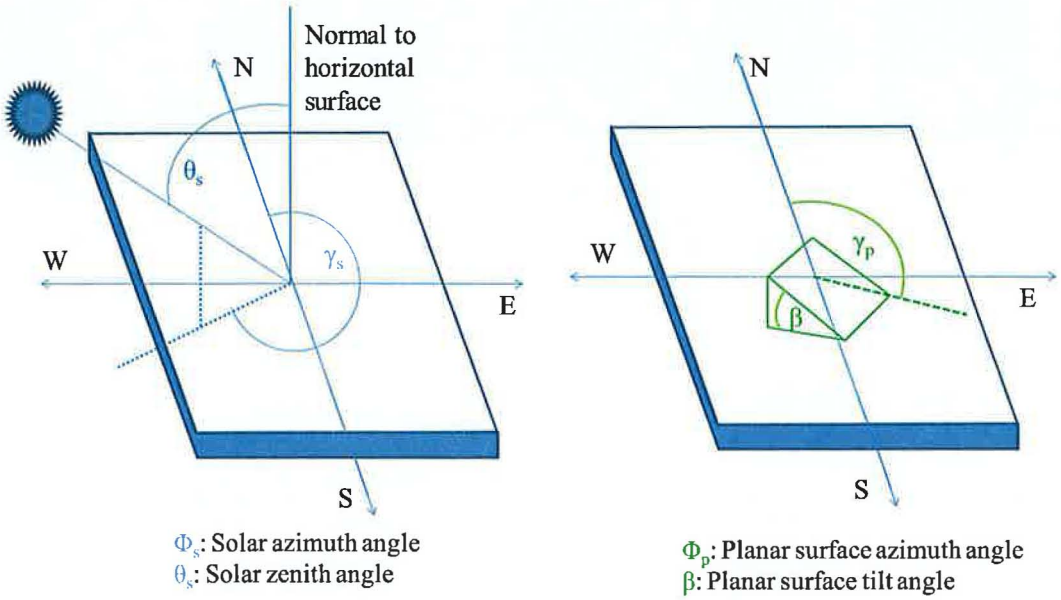

Figure 5.2. The position of the sun is defined by the solar zenith angle, θ_s, and the solar azimuth angle, γ_s. A tilted planar surface has tilt angle, β, and surface azimuth angle γ_p.

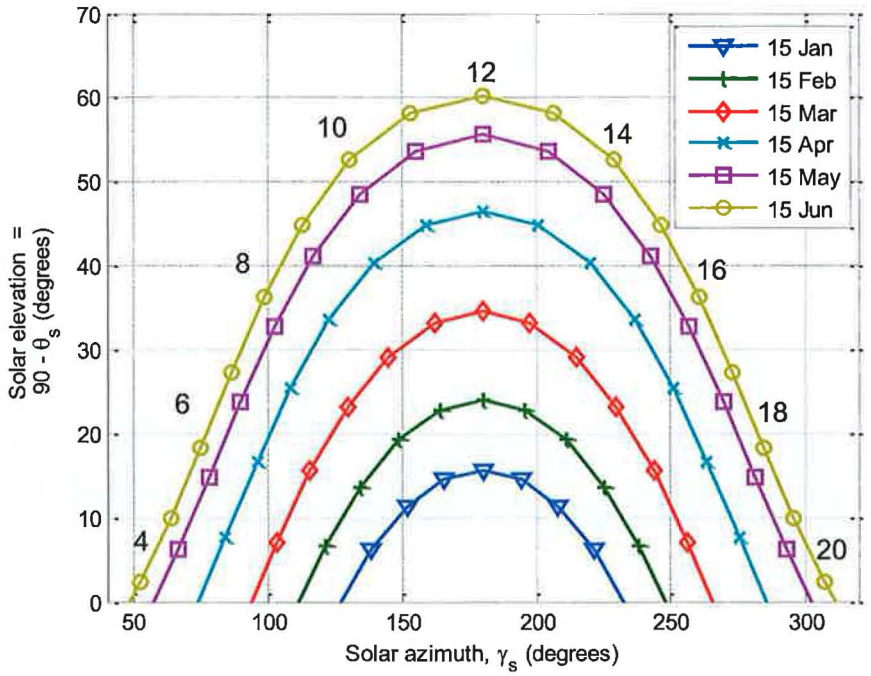

Figure 5.3. The solar path, describing hourly solar elevation angle ($90°-\theta_s$) and azimuth angle, γ_s, for the 15th day of months January to June, at a location latitude 53° North.

The solar angles θ_s and γ_s are given (Sproul, 2007) by;

$$\theta_s = \cos^{-1}(\sin\delta\sin\phi + \cos\delta\cos\phi\cos\omega) \tag{5.5}$$

$$\gamma_s = \cos^{-1}\left(\frac{\cos\phi\sin\delta - \cos\delta\sin\phi\cos\omega}{\cos\left(\pi/2 - \theta_s\right)}\right) \tag{5.6}$$

$$\text{if } \omega > 0\,, \quad \gamma_s = 2\pi - \gamma_s$$

where, Φ is the location latitude, north (positive) or south (negative) of the equator, δ is the solar declination, i.e., the angular position of the sun with respect to the plane of the earth's equator, given (Duffie and Beckman, 1990) by;

$$\delta_{\text{degrees}} = 23.45\sin\left(360\frac{284 + day_J}{365}\right) \tag{5.7}$$

and ω is the hour angle, i.e., the angular displacement of the sun to the east (negative) or west (positive) of the local meridian, given by;

$$\omega = 15(\text{solar hour-12})\pi/180 \tag{5.8}$$

5.1.3 Beam irradiance on tilted surface

For a surface with tilt angle, β, oriented at a planar azimuth angle, γ_p, as shown in Figure 5.2, the beam irradiance on a tilted surface, B_t, is given (Drif *et al.*, 2008) by;

$$B_t = B_h \frac{\max(0, \cos\theta_{ip})}{\cos\theta_s} \qquad 5.9$$

where θ_{ip} is the angle of incidence on the tilted planar surface given (Sproul, 2007) by;

$$\cos\theta_{ip} = \cos\beta\cos\theta_s + \sin\beta\sin\theta_s\cos(\gamma_p - \gamma_s) \qquad 5.10$$

If the sun is located behind the tilted surface plane, the beam irradiance on the tilted surface, B_t, is zero, as is shown by the graph in Figure 5.4.

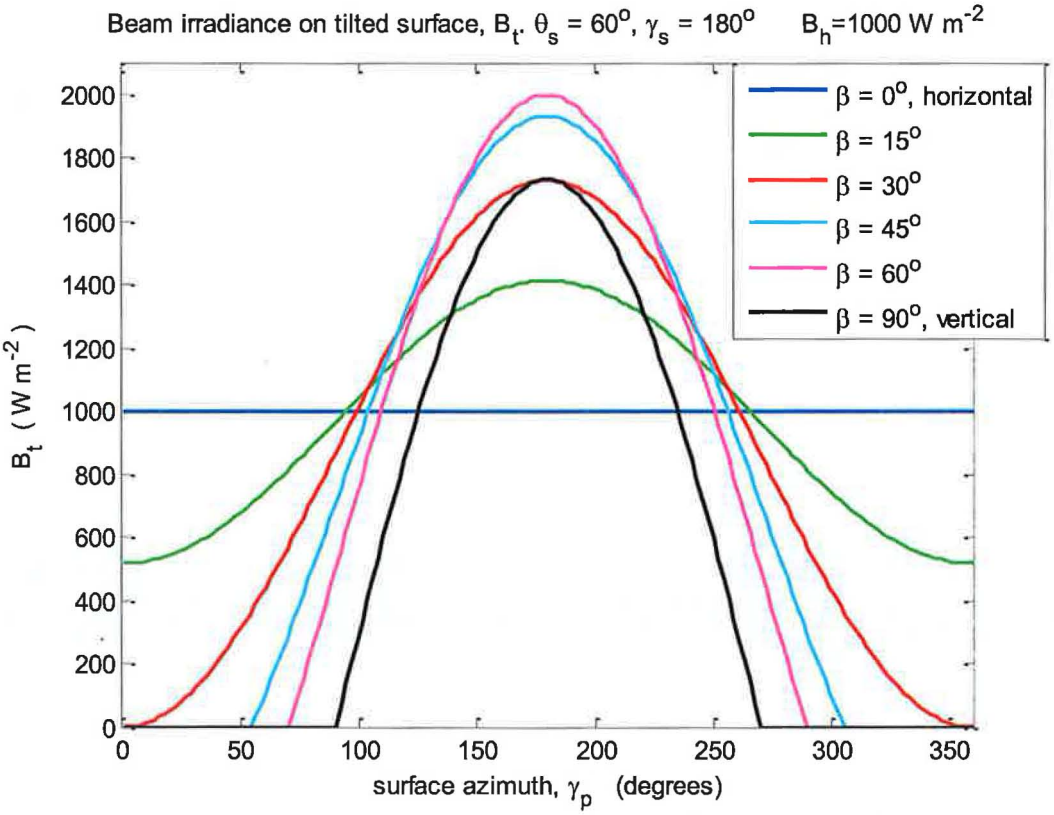

Figure 5.4. Beam irradiance on surface with varying tilt angle, β and azimuth angle γ_p. calculated using eqn. 5.10, for an arbitrary beam irradiance on the horizontal of 1000 W m^{-2}. The solar zenith angle, θ_s, and azimuth angle, γ_s, are arbitrarily set to 60° and 180°, respectively.

5.1.4 Diffuse irradiance on tilted surface

The simplest model for calculating D_t is to assume that solar diffuse radiation is isotropic (Liu and Jordan, 1960), however, this model leads to an underestimation of D_t (Drif *et al.*, 2008). The Perez slope irradiance model is an anisotropic model which divides the sky dome into three geometric zones; (i) the circumsolar zone, (ii) the horizon band, and (iii) the remainder of the hemispherical sky dome, as illustrated in Figure 5.5. (Perez *et al.*, 1987; Perez *et al.*, 1990). In a two year study comparing predicted and measured hourly D_t on sloped surfaces at two sites in France (Perez *et al.*, 1987), the root mean squared errors in predicted D_t were 16.3%, 9.3%, 6.5% and 8.7% for North, South, East and West facing vertical surfaces, respectively.

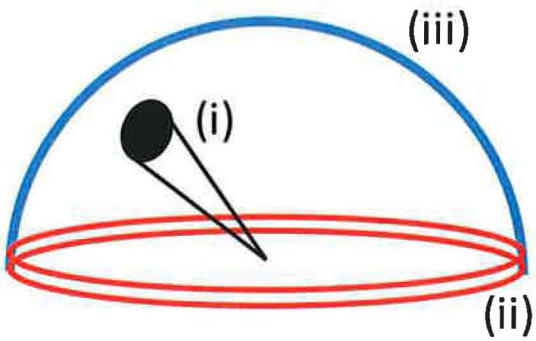

Figure 5.5. The Perez model of the sky dome divided into three geometric zones; (i) the circumsolar zone, (ii) the horizon band, and (iii) the remainder of the hemispherical sky dome.

The point-source Perez model for calculating diffuse irradiance on a tilted surface, D_t, is given by;

$$D_t = D_{cs} + D_{hz} + D_{iso} \qquad 5.11$$

where the circumsolar, horizon brightening and isotropic diffuse components, D_{cs}, D_{hz}, and D_{iso} are given by;

$$
\begin{aligned}
D_{cs} &= D_h F_1 \frac{\cos\theta_{ip}}{\cos\theta_s} \\
D_{hz} &= D_h F_2 \sin\beta \\
D_{iso} &= D_h (1 - F_1) \frac{(1+\cos\beta)}{2}
\end{aligned}
\qquad 5.12
$$

The circumsolar and horizon brightening coefficients, F_1 and F_2, are given by;

$$
\begin{aligned}
F_1 &= \max[0,\ (f_{11} + f_{12}\Delta + f_{13}\theta_s)] \\
F_2 &= f_{21} + f_{22}\Delta + f_{23}\theta_s
\end{aligned}
\qquad 5.13
$$

where, f_{1j} and f_{2j} (j=1→3) depend on the "sky clearness", and are obtained from the lookup table given in Appendix B. The sky brightness parameter, Δ, is defined as;

$$\Delta = m D_h / I_0 \qquad 5.14$$

where m is the air-mass given (Kasten and Young, 1989) by;

$$m = 1 \Big/ \left(\cos\theta_{s\,(\text{degrees})} + 0.50572(96.07995 - \theta_{s\,(\text{degrees})})\right)^{-1.6364} \qquad 5.15$$

5.1.5 Ground reflected irradiance

Ground reflectance is assumed to be isotropic from a horizontal ground surface. The ground reflected irradiance, R_t, depends on β and the ground surface albedo, ρ (Duffie and Beckman, 1990);

$$R_t = G_h(1-\cos\beta)\frac{\rho}{2} \qquad 5.16$$

Ground surface albedo, ρ, varies depending on the environment and also on the solar zenith angle. If the value of ρ is unknown, it is common to consider that $\rho = 0.2$ (Drif *et al.*).

5.1.6 Spectral irradiance

The average photon energy of solar insolation varies depending on air-mass and atmospheric conditions, with the transmitted spectrum being more "blue rich" in overcast conditions. Using a single standard spectrum, such as the American Society for Testing and Materials (ASTM, 2003) G-173-03 global hemispherical solar spectrum for air-mass 1.5 (AM 1.5g), will therefore underestimate QDSC power output in diffuse insolation conditions. Therefore, approximate beam and diffuse *spectral* irradiance are determined for use in the QDSC ray-trace model. The standard direct normal irradiance at air-mass 1.5 (AM 1.5d), shown in Figure 5.6, is normalised and then weighted by B_t to simulate the beam spectral irradiance component. Subtracting the AM 1.5d from the AM 1.5g irradiance, normalizing the result, and weighting by D_t yields the diffuse spectral irradiance component approximation. A useful study would be to compare the hourly spectral irradiance with measured spectral irradiance data, to quantify the error arising from using the approximated spectra. Comparisons could also be made with spectral irradiance models, such as the parameterised semi-empirical SPCTRL2 (Bird and Riordan, 1986) and SEDES2 (Nann and Riordan, 1991; Nann and Emery, 1992; Houshyani, 2007).

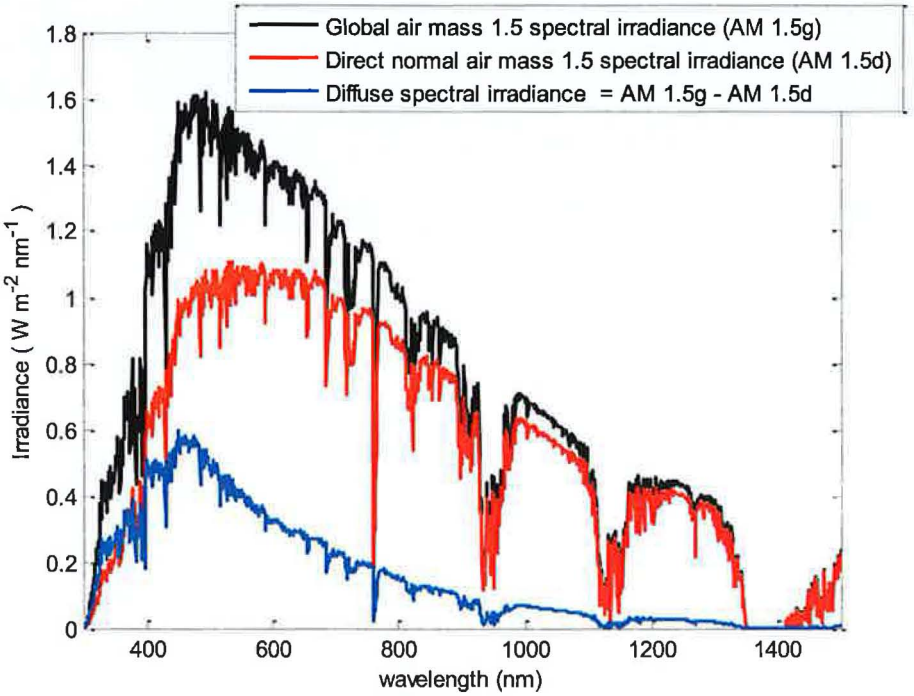

Figure 5.6. The diffuse spectral irradiance distribution (blue) is obtained by subtracting the direct normal (red) from the global (black) American Society for Testing and Materials, G-173-03, spectral irradiance.

5.1.7 Annual in-plane insolation

Total insolation (J/m^2) on a tilted surface is calculated by integrating G_t over a given time period. The total annual insolation on a tilted surface for the year 2008 at the Dublin location[xiii] is shown in Figure 5.7, with a broad maximum occurring at a tilt angle, β, of ~30°. Insolation levels ≥ 95% of the maximum are obtained over a wide range of β (<10° β <55°).

The optimum QDSC tilt angle may not necessarily correlate exactly with the maximum in-plane insolation, however, due to spectral effects and surface reflection

[xiii] assuming a surface albedo, $\rho = 0.2$

losses. Relative QDSC annual energy yields for varying tilt angles are determined in section 5.2.2.

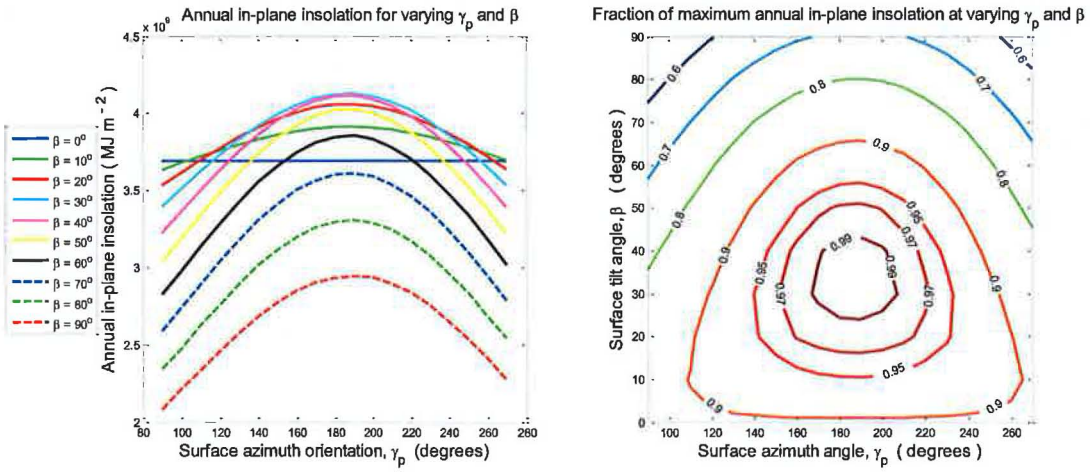

Figure 5.7. (a) Annual in-plane insolation for varying γ_p and β. (b) Fraction of the maximum annual in-plane insolation available at varying γ_p and β.

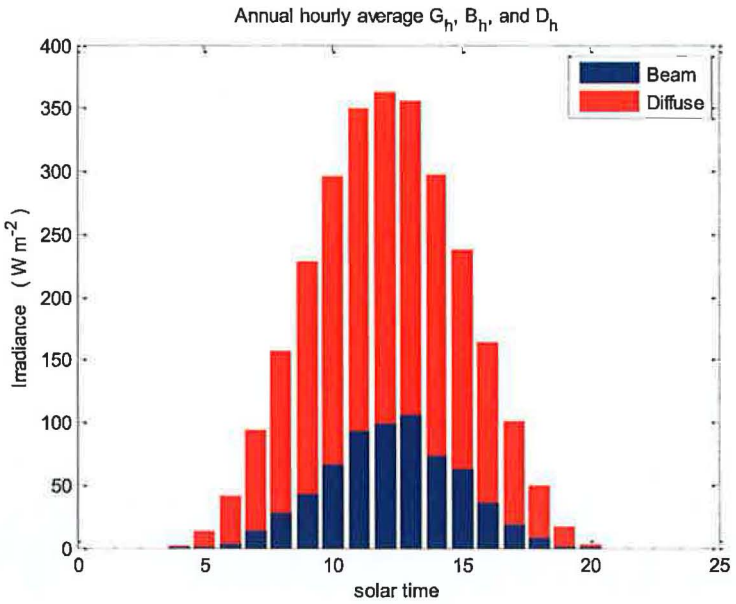

Figure 5.8 Annual hourly global horizontal irradiance, G_h, (red + blue) measured at a location in Dublin, Ireland, and the calculated beam and diffuse components, B_h (blue) and D_h (red).

5.2 QDSC performance in outdoor conditions

5.2.1 Diurnal variation in QDSC concentration ratio

The hourly concentration ratio of a 20 x 20 x 0.3 cm QDSC is determined for the mean day of each calendar month under the following assumptions;

- Fixed QDSC plate at β=30° and γ_p=180°.
- QD QY = 100%,
- $\alpha_{mat} = 0.02\ cm^{-1}$,
- $n_2 = 1.5$,
- $\rho = 0.2$,
- 20 x 0.3 cm mc-Si cells, characterised by the IQE and R_{pv} curves shown in Figure 2.6, are attached at each of the four QDSC edges.

QDSC concentration ratio is equivalent to the ratio of the short circuit current of the PV cells attached to the concentrator, I_{sc,PV_C}, to the short circuit current of the same PV cells not attached to the concentrator, $I_{sc,PV}$, oriented on the same plane as the concentrator top surface, i.e.;

$$C = \frac{I_{sc,PV_C}}{I_{sc,PV}} \qquad 5.17$$

Using the irradiance data from the Dublin location, average hourly $I_{sc,PV}$ and I_{sc,PV_C} are predicted for the mean day of each month from eqn. 2.22. The annual hourly average $I_{sc,PV}$ and I_{sc,PV_C} are shown in Figure 5.9. The concentration ratio, C, is

higher in mornings and evenings than at mid-day, due to an increase in QDSC η_{abs} at these times arising from;

i) An increase in pathlength of the direct component of the solar radiation on a double pass through the QDSC plate.

ii) A higher mean photon energy of the global irradiance, as hourly k_D is higher in mornings and evenings at this location, as shown in Figure 5.8.

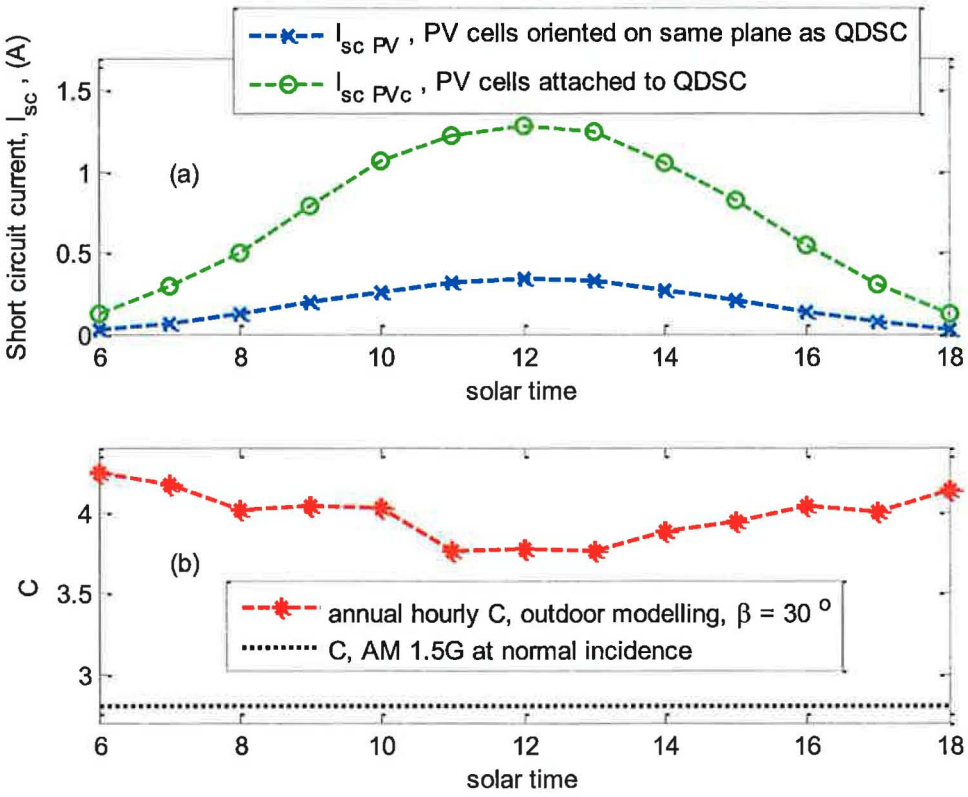

Figure 5.9. Diurnal variation of annual average hourly (a) I_{sc,PV_C} and $I_{sc,PV}$ and (b) concentration ratio, C, for a QDSC inclined at 30°. The predicted C for the same QDSC assuming the standard AM1.5G spectrum at normal incidence is just 2.8, indicated by the dashed black in line in (b).

Higher C at times when global irradiance is low is a further advantage of LSC devices, in that the useful daily operating time of the PV cells is extended. The predicted C for the same QDSC assuming the standard AM1.5G spectrum at normal incidence is just 2.8. In outdoor simulations, however, $3.7 < C < 4.2$ is attained on an

annual average. Therefore, comparing QDSCs to crystalline silicon PV cells using STC does not give a realistic reflection on the relative power output of the two technologies in outdoor conditions, particularly in climates where the diffuse component of solar radiation is predominant[xiv]. The results highlight the advantage of using QDSCs in such climates.

5.2.2 Monthly and annual relative energy output.

Hourly short circuit current of the attached PV cells, I_{sc,PV_C} , are calculated for the QDSC described in section 5.2.1, for varying β ($0° \leq \beta \leq 90°$) over the duration of each calendar month's "mean" day. QDSC power output is assumed to be directly proportional to I_{sc,PV_C} . The relative monthly *energy* yield is assumed to be proportional to the sum of the predicted hourly I_{sc,PV_C} over the duration of the mean day of each month;

$$\text{relative monthly energy output} \propto \sum_{hour=1}^{24} I_{sc,PV_C} \qquad 5.18$$

The relative *annual* energy yield is proportional to the sum of the twelve predicted monthly yields;

$$\text{relative annual energy output} \propto \sum_{month=1}^{12} \sum_{hour=1}^{24} I_{sc,PV_C} \qquad 5.19$$

[xiv] As the absorption range of the LSC extends towards the band-gap of the attached solar cell, the difference between AM 1.5G and outdoor predicted C diminishes.

5.2.3 Optimum QDSC tilt angle, β

Relative monthly energy yields are calculated for varying tilt angle, β, to determine the optimum QDSC β for the given location. Optimal β in terms of a tilted surface receiving the maximum *insolation*, can be determined without ray-trace modelling by calculating hourly G_t and summing over a given time period (see section 5.1.7). However, the optimum β in terms of the maximum energy yield may not necessarily match the maximum in-plane insolation, due to a) spectral effects, e.g., it may be more beneficial to fix the QDSC tilt angle to receive more diffuse insolation, as the device is more efficient at shorter wavelengths, and b) reflection losses.

Monthly and annual energy yields for varying β are shown in Figure 5.10. The predicted monthly optimum β varies from ~15° in summer to ~80° in winter months. A broad annual optimum exists between 20° and 30°. The predicted variation in annual energy yield is very similar to the variation in received in-plane insolation, as shown in Figure 5.10

QDSCs with one-axis tracking

Compared to a QDSC fixed at β = 30°, only a 13% increase is obtained if β is varied hourly to the particular hourly optimum β angle (i.e. utilizing one-axis tracking with the axis oriented east-west), as shown in Figure 5.11. QDSCs as low cost devices are, therefore, unlikely to benefit from utilization of solar tracking due to the additional associated installation, operational, and maintenance costs of tracking devices. Monthly adjustments in β to the monthly optimum β angle would result in only a 5% increase in annual energy yield.

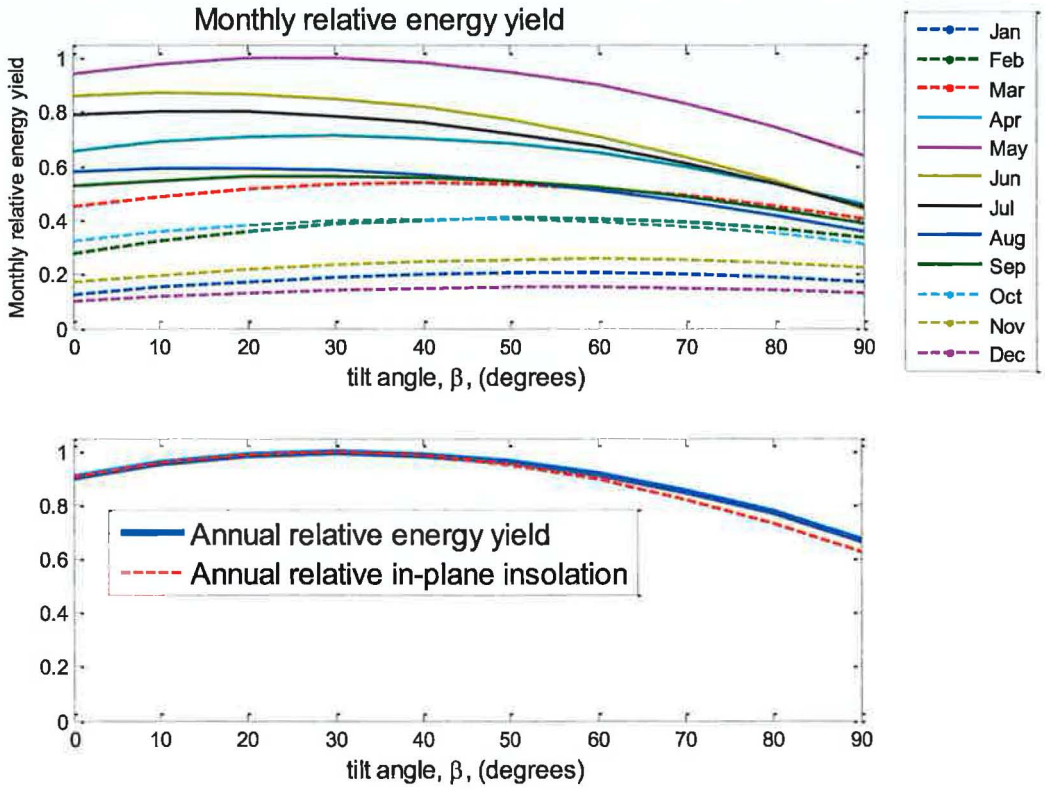

Figure 5.10. Relative QDSC monthly and annual energy output with varying tilt angle, β.

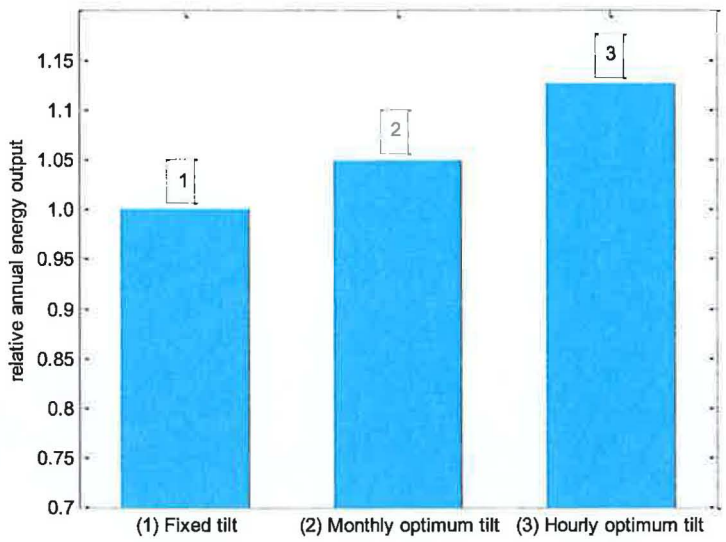

Figure 5.11. Relative annual QDSC energy yield for; 1: A fixed QDSC tilt angle (β=30°), 2: β adjusted each month to the monthly optimum β, and 3: β adjusted hourly to hourly optimum β.

5.2.4 Annual energy yield for varying matrix material properties

As discussed in chapter 4, increasing the plate refractive index, *n*, reduces escape cone losses but increases external top surface reflection losses. Assuming a QD QY of 80%, the relative annual energy yield is predicted for the QDSC detailed in section 5.2.1. The results for varying *n* are shown in Figure 5.12. In section 4.2, a 10% increase in device concentration ratio was attained, under direct normal insolation, with an increase in *n* from 1.5 to 1.7. However, there is only ~5% increase in annual outdoor QDSC energy yield with an identical increase in *n* from 1.5 to 1.7. The relatively smaller increase under outdoor conditions is due to larger external top surface reflection losses than is the case under direct normal insolation.

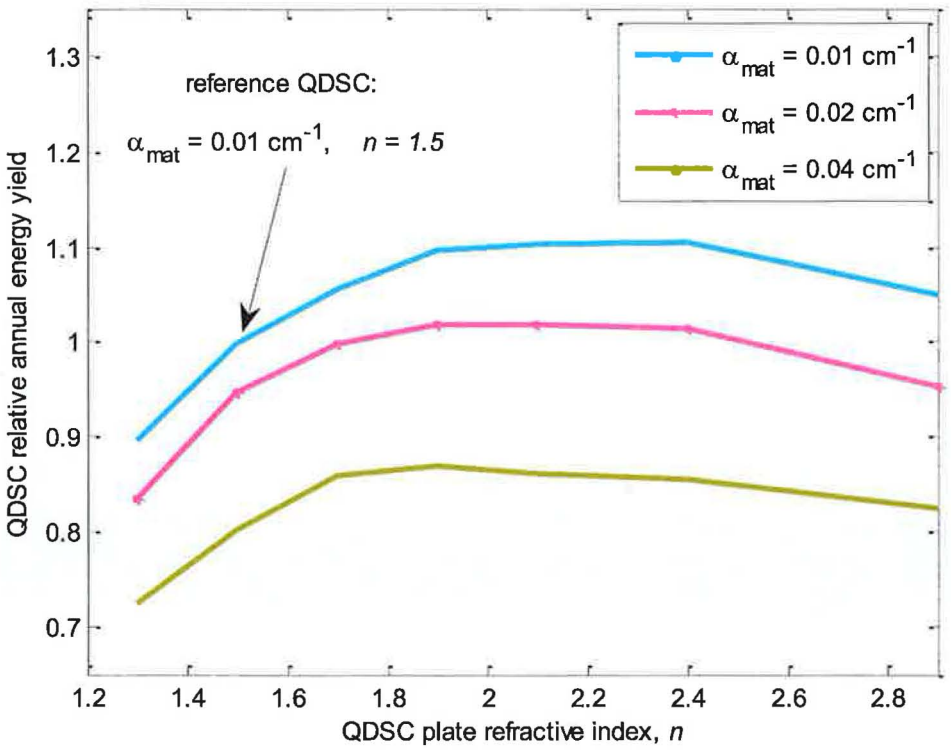

Figure 5.12. Variation in QDSC relative annual energy yield with plate refractive index, *n*, and absorption coefficient, α_{mat}.

5.3 Anti-reflection coatings

Annual reflection losses total 13% of photons incident on the QDSC modelled in section 5.2.4 with plate refractive index of 1.7. Anti-reflective coatings (ARCs) can reduce reflection losses. The effectiveness of an ARC on annual energy yields differs to the effect on power output under direct normal incidence (Wohlgemuth *et al.*, 2005), as reflectance depends on the angle of incidence, θ_1, and the wavelength of the incident light, λ_1. MgF_2, a common thin-film ARC material, has a refractive index of 1.38 (at 550 nm). Reflectance from the QDSC with a MgF_2 ARC is determined from the set of equations in Appendix D for varying θ_1, λ_1, and thin-film thickness, t_f, and is shown in Figure 5.13. A thicker thin-film results in the minimum reflectance shifting to longer wavelengths. The ARC does not have an effect on the total internal reflection efficiency within the QDSC plate (Petrova-Koch *et al.*, 2008)

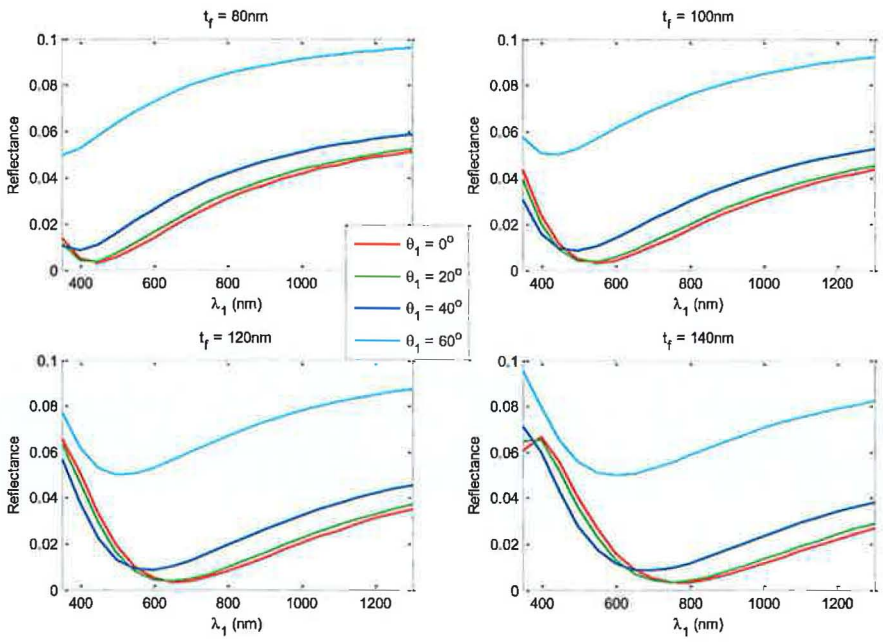

Figure 5.13. Reflectance from MgF_2 thin-film anti-reflection coating on substrate of refractive index 1.7, for varying angles of incidence, θ_1, thin-film thickness, t_f, and wavelength of incident light, λ_1.

5.3.1 Effect of ARC on QDSC annual energy yield

Annual energy yields are determined assuming a thin-film ARC deposited on the QDSC of plate refractive index of 1.7 modelled in section 5.2.4. Optimising thin-film thicknesses, t_f, to minimise total *reflection losses* does not necessarily maximise QDSC *energy yield*, as reflection ought to be reduced in wavelength regions where the QDSC is most efficient. Four values of t_f are assumed for the analysis - 80, 100, 120, and 140 nm - and external reflection losses are calculated as in Appendix D. An optimum ARC thickness, t_f, of 120 nm results in an increase in QDSC energy yield of 8% compared to the same QDSC with no ARC, as shown in Figure 5.14. A thickness of 140 nm minimises total *reflection* losses but doesn't maximise the *energy* yield. While more accurate spectral irradiance data would be required to fully optimise ARC thickness, the results do show that significant gains in QDSC annual energy yields are realizable through the inclusion of an optimised ARC.

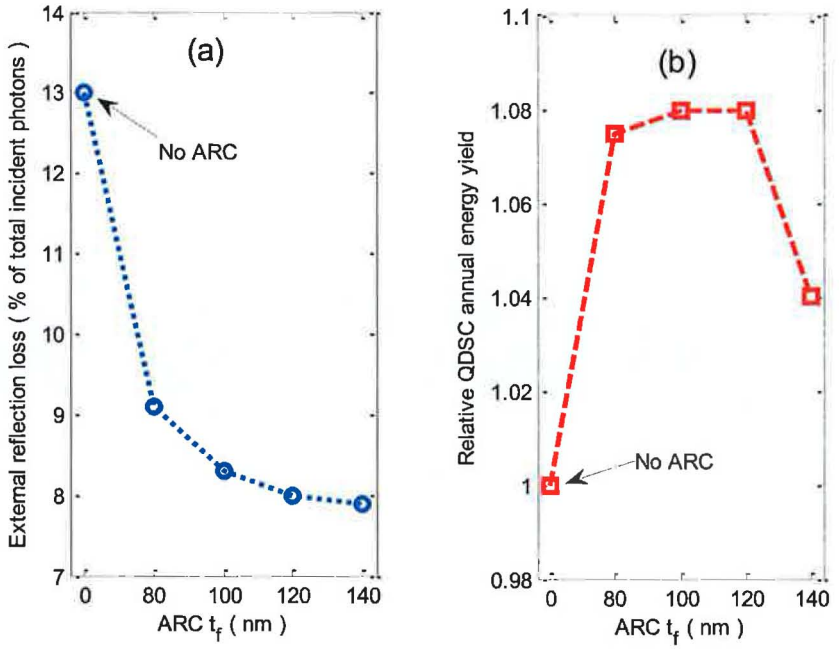

Figure 5.14. (a) External reflection losses (% of total incident photons) and (b) relative QDSC annual energy yield for varying MgF_2 thin-film ARC thickness, t_f.

5.4 Chapter conclusions

- Measured horizontal irradiance data from a location in Dublin, Ireland, were used as ray-trace model input. Combined with the Mondol diffuse-global correlation model and the Perez slope irradiance model, monthly averaged hourly spectral irradiance and incident angle distributions on tilted QDSC plates were determined.
- Predicted QDSC concentration ratio, C, is higher in mornings and evenings than at mid-day, due to a higher diffuse component at those times. Higher C at times when global irradiance is low is a further advantage of QDSC devices, in that the useful daily operating time of the PV cells is extended.
- The predicted C for a particular QDSC under the standard AM1.5G spectrum at normal incidence is just 2.8. In outdoor simulations, however, $3.7 < C < 4.2$ is attained on an annual hourly average for the same QDSC. The results highlight the advantage of using QDSCs in climates where the diffuse component of solar radiation is predominant.
- The predicted monthly optimum tilt angle, β, varies from ~15° in summer months to ~80° in winter, with a broad annual optimum between 20° and 30°.
- Compared to a QDSC fixed at $\beta = 30°$, a 13% increase in annual energy yield is attained if β is varied hourly to the particular hourly optimum β (i.e., assuming one-axis tracking with the axis oriented east-west). QDSCs as low cost devices are, therefore, unlikely to benefit from utilization of solar tracking due to the additional associated installation and maintenance costs of tracking devices.
- A 5% increase in annual QDSC energy yield is attained with an increase in QDSC plate refractive index, n, from 1.5 to 1.7. This is significantly lower than the predicted increases observed under direct normal insolation, due to larger external

top surface reflection losses in outdoor conditions than is the case under direct normal insolation.

- Annual external reflection losses account for 13% of total photons incident on a QDSC, of refractive index 1.7, fixed at $\beta = 30°$. The ray-trace model can be used to optimize anti-reflective coating (ARC) thickness in order to minimize reflection losses in the spectral range where the QDSC is more efficient. A potential 8% increase in QDSC annual energy yield is predicted using an optimized anti-reflective coating with the QDSC of refractive index 1.7.

5.5 References

American Society for Testing and Materials, (2003). Terrestrial Reference Spectra for Photovoltaic Performance Evaluation - G-173-03 http://www.astm.org/ (last accessed 01/08/09)

Bird, R.E., Riordan, C., (1986). Simple Solar Spectral Model for Direct and Diffuse Irradiance on Horizontal and Tilted Planes at the Earth's Surface for Cloudless Atmospheres. *Journal of Climate and Applied Meteorology,* 25, 87-97.

Drif, M., Pérez, P.J., Aguilera, J., Aguilar, J.D., (2008). A new estimation method of irradiance on a partially shaded PV generator in grid-connected photovoltaic systems. *Renewable Energy,* 33, 2048-56.

Duffie, J.A., Beckman, W.A., (1990). *Solar Engineering of Thermal Processes*, John Wiley & Sons, New York.

El-Shaarawy, M.G., El-Bashir, S.M., Hammam, M., El-Mansy, M.K., (2007). Bent fluorescent solar collectors (BFSCs): Spectroscopy, stability and outdoor performance. *Applied Physics,* 7, 643-9.

Erbs, D.G., Klein, S.A., Duffie, J.A., (1982). Estimation of the diffuse radiation fraction for hourly, daily and monthly-average global radiation. *Solar Energy,* 28, 293-302.

Goetzberger, A., (1978). Fluorescent Solar Energy Collectors: Operating Conditions with Diffuse Light. *Applied Physics,* 16, 399-404.

Houshyani, B., (2007). SEDES2 Spectral Model Validation; A comparative study of spectral radiative transfer models for clear and cloudy sky conditions using SMARTS, SPCTRL2 and MODTRAN. Department of Science, Technology and Society, Copernicus Institute for Sustainable Development and Innovation,, Utrecht University, The Netherlands.

Kasten, F., Young, A.T., (1989). Revised optical air mass tables and approximation formula. *Applied Optics* 28, 22, 4735–8.

Lean, J., Rind, D., (1998). Climate Forcing by Changing Solar Radiation. *Journal of Climate,* 11, 12, 3069-94.

Liou, K.N., (2002). *An introduction to atmospheric radiation*, Academic Press, San Diego.

Liu, B., Jordan, R., (1960). The interrelationship and characteristic distribution of direct, diffuse and total solar radiation. *Solar Energy,* 4, 3, 1-19.

Mansour, A.F., El-Shaarawy, M.G., El-Bashir, S.M., El-Mansy, M.K., Hammam, M., (2002). A qualitative study and field performance for a fluorescent solar collector. *Polymer Testing,* 21, 277-81.

Mondol, J.D., Yohanis, Y.G., Norton, B., (2008). Solar radiation modelling for the simulation of photovoltaic systems. *Renewable Energy,* 33, 1109-20.

Nann, S., Emery, K., (1992). Spectral effects on PV-device rating. *Solar Energy Materials and Solar Cells,* 27, 189-216.

Nann, S., Riordan, C., (1991). Solar Spectral Irradiance under Clear and Cloudy Skies: Measurements and a Semiempirical model. *Journal of Applied Meteorology,* 30, 447-62.

Perez, R., Ineichen, P., Seals, R., Michalsky, J., Stewart, R., (1990). Modelling daylight availability and irradiance components from direct and global irradiance. *Solar Energy,* 44, 5, 271-89.

Perez, R., Seals, R., Ineichen, P., Stewart, R., Menicucci, D., (1987). A new simplified version of the Perez diffuse irradiance model for tilted surfaces *Solar Energy,* 39, 3, 221-31.

Petrova-Koch, V., Hezel, R., Goetzberger, A., (2008). *High-Efficient Low-Cost Photovoltaics: Recent Developments*, Springer-Verlag, New-York.

Pravettoni, M., Pravettoni, F., Virtuani, A., Kenny, R.P., Chatten, A.J., Barnham, K.W.J., (2009a). Outdoor characterisation of Luminescent Solar Concentrators and their possible architectural integration on a historically relevant site in Milan (Italy) *Proceedings of 34th IEEE Photovoltaics Specialists Conference*, Philadelphia, USA., to be published.

Pravettoni, M., Virtuani, A., Kenny, R.P., Farrell, D.J., Chatten, A.J., Barnham, K.W.J., (2009b). Outdoor Characterization of High Efficiency Luminescent Solar Concentrators for Smart Windows. *Proceedings of Materials Research Society Spring Meeting* San Francisco, USA., to be published.

Reindl, D.T., Beckman, W.A., Duffie, J.A., (1990). Diffuse fraction corrections. *Solar Energy,* 45, 1-7.

Salem, A.I., Mansour, A.F., El-Sayed, N.M., Bassyouni, A.H., (2000). Outdoor testing and solar simulation for oxazine 750 laser dye luminescent solar concentrator. *Renewable Energy,* 20, 95-107.

Sproul, B.A., (2007). Derivation of the solar geometric relationships using vector analysis. *Renewable Energy,* 32, 1187-205.

Wohlgemuth, J.H., Cunningham, D.W., Nguyen, A.M., Shaner, J., Ransome, S.J., Artigao, A., Fernandez, J.M., (2005). Increased energy collection using anti-reflective coated glass. *Proceedings of 20th European Photovoltaic Solar Energy Conference*, Barcelona, Spain, 1985-8.

6 Towards a viable QDSC.

6.0 Introduction

Crystalline silicon technologies currently represent over 90% of PV module market share (Bagnall, 2008). As global silicon PV module manufacturing capacity and scale has increased, average manufacturing costs have decreased from US$6 / W_p in 1992 to US$2.75 / W_p in 2005 (Margolis *et al.*, 2006). The rate of reduction was greatest in the period 1992-2000. The reduction in average costs slowed significantly after 2000 when the cost per W_p was already as low as $2.75/ W_p. In the next 20 years, total costs per W_p of "1st generation" silicon PV technologies are predicted to fall by less than 30% (Bagnall, 2008). QDSC costs per W_p are determined to analyse the potential for (stable) devices to compete with crystalline silicon technologies. The QD *QY* required to do so, under varying QDSC cost scenarios, is quantified.

6.1 QDSC manufacturing costs

Minimum QDSC manufacturing costs can be estimated from the total cost of the principal components, i.e., the matrix materials and quantum dots;

Matrix materials

The price of bulk-purchased PMMA is < €3/kg (ICIS, 2009). A $1m^2$ plate of 0.3 cm thickness would require ~3.5 kg of PMMA, assuming a specific density of 1.16 (Sane *et al.*, 2001), which equates to ~€10/m^2.

Quantum Dots

Using the ray-trace model, the optimum concentration (mass/volume) of PbS QDs in a 3mm thick QDSC incorporating a rear reflector was determined to be ~0.05 mg/ml. For a 1 m^2 plate, therefore, ~0.15 g of the particular PbS QDs are required. Current prices of PbS QDs from commercial suppliers are ~€15,000/g (Evident Technologies, USA), equivalent to ~€2,000/m^2 of QDSC plate – costs which would need to be reduced by two to three orders of magnitude for QDs to be considered viable candidates for LSC devices. Cademartiri *et al.* (2006) estimate the total cost of materials required in the production process of their PbS QDs, however, to be < €10/g. It is estimated that with a very large scale production process, QDs could be produced for as little as €3/g (Barnham, 2008), whereby QD costs would be negligible compared to the other materials required for a QDSC.

6.1.1 QDSC manufacturing costs per Watt peak calculations

The potential QDSC manufacturing cost per W_p is compared with that of crystalline silicon modules. The manufacturing cost of a QDSC is assumed to be proportional to the area of concentrator plate, A_{conc}, and PV cells, A_{pv}, required;

$$\text{relative cost} = \left(\frac{A_{pv}}{costfactor_{pv}}\right) + \left(\frac{A_{conc}}{costfactor}\right) \qquad 6.1$$

where the variable *costfactor*, defines the cost of the concentrator plate relative to the cost of (single-sided) crystalline silicon PV per unit area;

$$costfactor = \frac{\text{cost of PV per unit area}}{\text{cost of concentrator plate per unit area}} \qquad 6.2$$

The QDSC relative power output is determined from eqn. 3.4. Bende *et al.* (2008) proposed the use of bi-facial PV cells on LSCs, with cells attached to two edges of each individual LSC plate (of optimum size), and multiple plates configured onto a larger module so that each of the four LSC edges is in contact with one side of a bi-facial cell, as illustrated in Figure 6.1. In this configuration, costs per W_p can be reduced providing that the cost of bi-facial cells, per m^2 *active* area, is less than twice that of single sided cells of equivalent efficiency, η. The variable $costfactor_{pv}$ in eqn. 6.1 defines the cost of the bi-facial cells;

$$costfactor_{pv} = \frac{\text{cost of single-sided PV per unit active area}}{\text{cost of bi-facial cells per unit active area}} \qquad 6.3$$

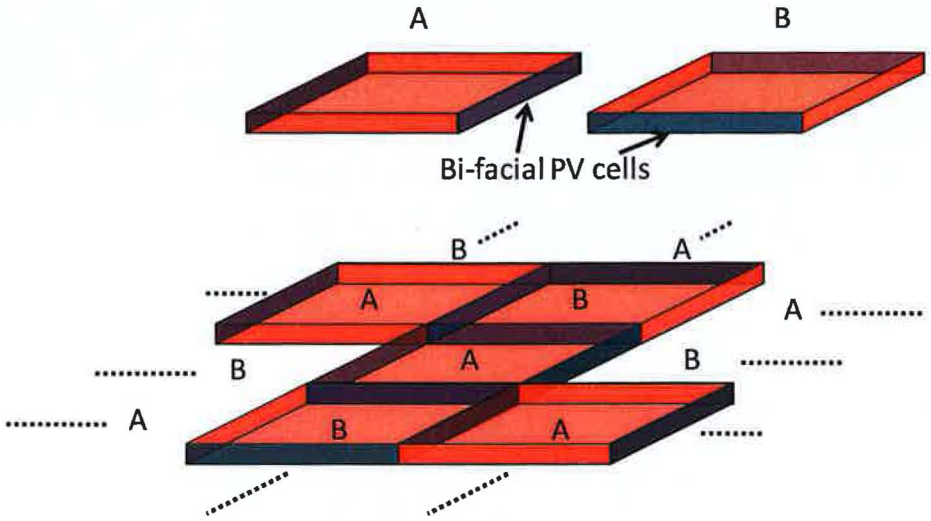

Figure 6.1. The cost of attached PV cells can be reduced if bi-facial cells are used, with the bi-facial cells attached to two sides of each QDSC plate of optimum dimensions. Multiple plates are packed adjacently, in a chequered configuration, to form a larger panel of required size.

At €2/W_p manufacturing costs, a PV module with η = 18% equates to €360/m^2. Richards *et al.* (2007) estimated the potential dye LSC plate costs (including PMMA, dyes, glass cover, and framing) to be potentially as low as €24/m^2, equating to a *costfactor* of 15. A *costfactor* of 15 is also used in the cost optimisation analysis of Bende *et al.* (2008), based on estimated LSC material costs[xv].

Assuming the current cost of PMMA and potentially low cost of QDs outlined in section 6.1, a QDSC cost of ~€22/m^2 (*costfactor* = 16) seems reasonable. However, Smestad (2008) estimates that ~€70/m^2 of actual production costs of thin film silicon PV modules, fabricated in a large scale production facility (20MW_p/ year), is attributed to the moisture barrier, framing, electrical interconnections, encapsulant and sealant materials required. Arguably, all these materials would be

[xv] Bende *et al.* include the cost of attached PV cells in estimated "plate" costs, whereas the analysis above *excludes* the cost of the PV cells in the "plate" cost, treating them as an additional separate cost. The relative cost factor of 15, assumed by Bende *et al.* (2008), is actually equivalent to a *costfactor*, as defined in eqn. 6.2, of ~16.5.

required for a QDSC module, resulting in significantly greater manufacturing costs per m^2. A *costfactor* of 4 (i.e. €90/m^2 QDSC) is considered below, to account for this higher QDSC manufacturing cost scenario.

From eqn 2.15, concentration ratios, C, are predicted for a QDSC of varying top surface aperture area, A_{conc}, with the following assumptions;

- an incident insolation spectrum corresponding to air-mass 1.5
- a plate refractive index of 1.5
- a matrix material absorption coefficient of 0.01 cm^{-1}
- the QD photon absorption and emission spectra shown in Figure 6.2.
- a diffuse rear reflector with reflectivity 0.97
- PV cells attached at all four QDSC sides

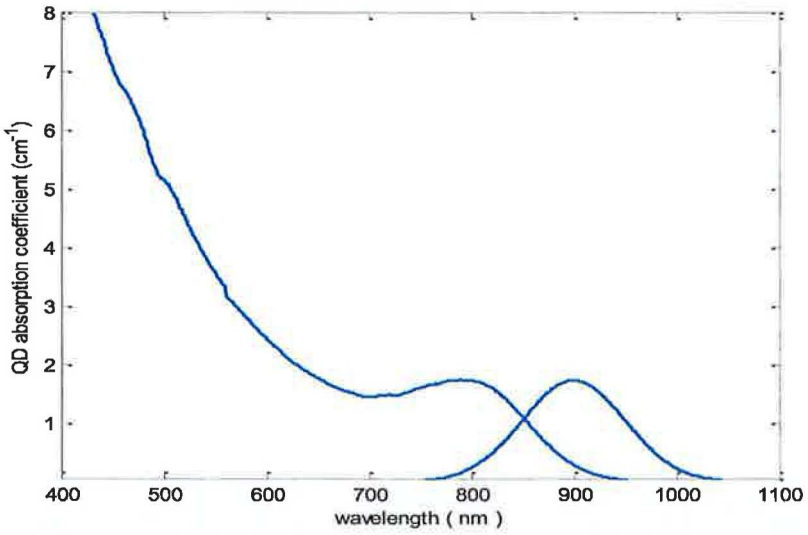

Figure 6.2. Absorption and emission spectra of PbS QDs (λ_{em} = 905 nm, Evident technologies)

6.1.2 QD quantum yields required for a viable QDSC

C are predicted for QDSCs of varying top surface aperture area, A_{conc}, to determine what QD QY is required for the QDSC to compete with conventional PV module manufacturing costs per unit power output. A *manufacturing* cost of €2/W_p is assumed for current crystalline silicon technologies. Figure 6.3 (a) shows the predicted C for varying A_{conc} and QD QY. Assuming a *costfactor* of 16, the cost per unit power for varying A_{conc} is given in Figure 6.3 (b). A QD QY of 50% is required for this particular QDSC to attain a manufacturing cost per unit power < €2/W_p.

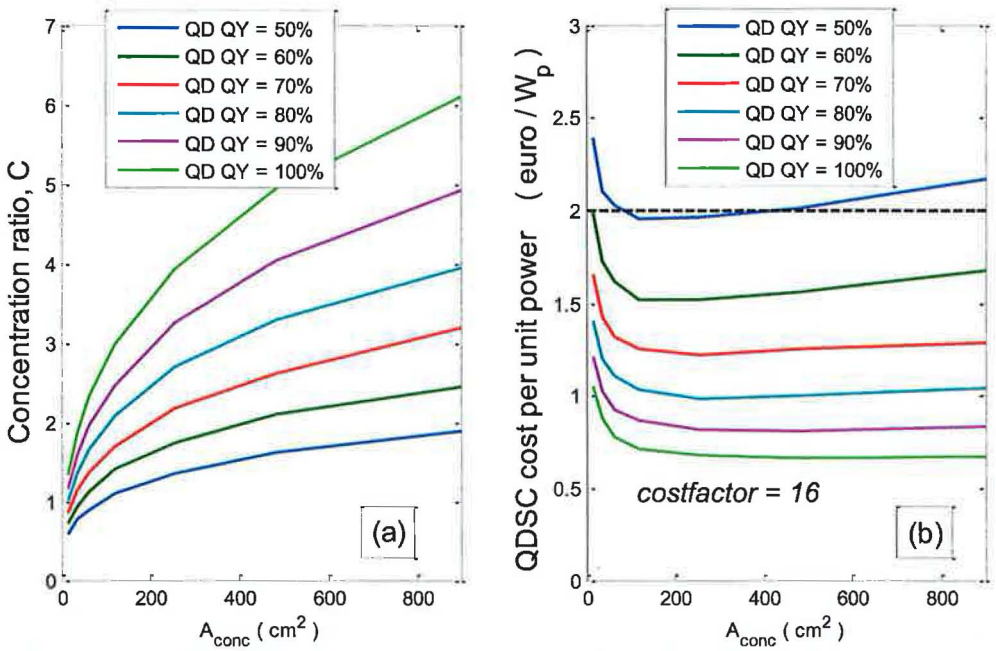

Figure 6.3. (a) Predicted C and (b) cost per W_p for QDSCs of varying top surface aperture area, A_{conc}, and QD quantum yield (QY).

A *costfactor* of 16 may underestimate the realistic manufacturing costs of QDSCs, when the framing, sealing and interconnection costs are included, as discussed above. Therefore, reduced *costfactor* of 8 and 4 are considered below. Three bi-facial PV cell costs are assumed in the analysis – (i) 360, (ii) 240, and (iii)

€180/m^2 active area. The maximum bi-facial cell cost of €360/m^2 active area would be equivalent to using two single-sided PV cells, of equivalent η, back-to-back.

The optimised cost per unit power output attained using each of the three QDSC cost scenarios (i.e. *costfactor* of 16, 8, and 4), and for each of the three bi-facial cost approximations, is shown in Figure 6.4. At a *costfactor* of 8, QD QYs of 70 – 80 % would yield QDSC manufacturing cost < €2/W_p. At a *costfactor* of 4, QD QYs > 95% are required. Bi-facial PV cells could reduce optimised QDSC cost per W_p by up to 25% compared to using single-sided cells.

As discussed in section 1.1 the production cost of *CdTe thin-film* PV modules is now estimated to be < €0.75/W_p. Only in the lowest QDSC cost assumptions, i.e. Figure 6.4(a), does this particular QDSC attain comparable cost per unit power to the CdTe modules. Clearly, the total module costs including framing etc., need to be minimised if QDSCs are to compete with newer emerging PV technologies, such as CdTe thin-film PV.

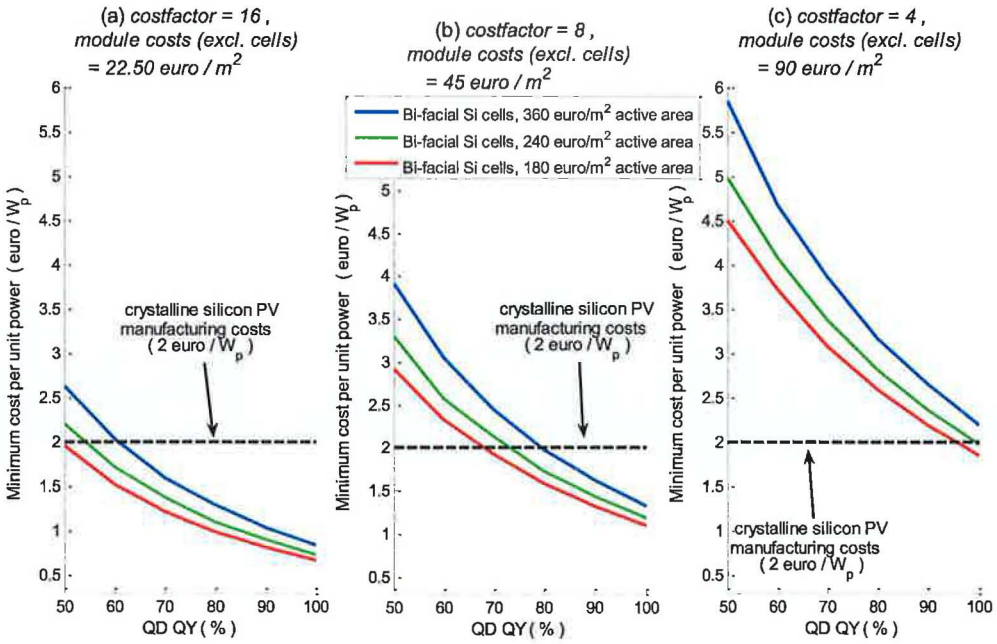

Figure 6.4. Minimum QDSC cost per W_p for varying plate costs (a), (b), and (c), varying QD quantum yield (QY), and varying bi-facial PV cell costs. A cost of €2/W_p is assumed for conventional silicon PV modules.

6.2 Chapter conclusions

- QDSC cost per W_p is a function of top surface aperture area. Optimised minimum QDSC cost per W_p have been quantified for varying QD QY under different cost scenarios.
- The QDSC high cost scenario assumes equivalent module sealing, framing, moisture barrier, encapsulant and interconnection costs as are incurred in current large-scale production of PV modules. In this case, the estimated QDSC cost is ~€90/m^2 (excluding PV cell costs). Even in the high cost scenario, QDSCs utilizing PbS near infra-red emitting QDs, can compete with "1st generation" silicon PV costs per W_p, provided efficient QDs can be exploited.
- *Bi-facial* PV cells can reduce optimised QDSC cost per W_p by up to 25%.
- Total QDSC module costs, including framing etc., need to be minimised if QDSCs are to compete with newer emerging PV technologies such as CdTe thin-film PV.

6.3 References

Bagnall, D.M., (2008). Photovoltaic technologies. *Energy Policy,* 36, 12, 4390-6.

Barnham, K.W.J., (2008). *Private Communication.*

Bende, E.E., Slooff, L.H., Burgers, A.R., van Sark, W.G.J.H.M., Kennedy, M., (2008). Cost & Efficiency Optimisation of the Luminescent Solar Concentrator. *Proceedings of 23rd European Photovoltaic Solar Energy Conference*, Valencia, Spain, 461-70.

Cademartiri, L., Bertolotti, J., Sapienza, R., Wiersma, D.S., von Freymann, G., Ozin, G.A., (2006). Multigram scale, solventless, and diffusion-controlled route to highly monodisperse PbS Nanoncrystals. *Journal of Physical Chemistry Letters B,* 110, 2, 671-3.

ICIS, Surrey, UK, (2009). www.icispricing.com (last accessed 13/9/09)

Margolis, R., Mitchell, R., Zweibel, K., (2006). Lessons Learned from the Photovoltaic Manufacturing Technology/PV Manufacturing R&D and Thin-Film PV Partnership Projects. National Renewable Energy Laboratory.

Richards, B.S., (2007). Performance enhancement and cost reduction potential of photovoltaic technologies via the application of luminescent materials. *Proceedings of Photovoltaic Science and Applications Technology 3*, Durham, UK, 5-8.

Sane, S.B., Cagin, T., Knauss, W.G., Goddard, W.A., (2001). Molecular dynamics simulations to compute the bulk response of amorphous PMMA. *Journal of computer-aided materials design* 8, 87-106.

Smestad, G.P., (2008). The basic economics of photovoltaics. *Proceedings of Solar Energy: New Materials and Nanostructured Devices for High Efficiency*, Palo Alto, USA, STuC8.

7 Conclusions

Commercially available visible-emitting QDs have been used by many groups to date in thin-film and homogeneously doped QDSC plates (Gallagher et al., 2007; Bose *et al.*, 2007; Sholin *et al.*, 2007; Rowan *et al.*, 2008). However, QDSC plates which increase the attached PV cell power output under standard test conditions (i.e. concentration ratio > 1) have not been reported. The low concentration ratios attained have been attributed to low luminescent QYs and large spectral overlaps between QD photon emission and absorption spectra. Initial motivation for developing the QDSC ray-trace model was to investigate the realistic potential performance of QDSCs (subject to the spectral overlap limitations), assuming efficient QDs could be encapsulated in suitable matrix materials whilst preserving high luminescent QY. Adopting a *ray-trace* approach allows the effect of varying geometry, and varying (multiple) luminescent species type on device performance to be analsyed. A *Monte-Carlo* ray-trace approach allows the multiple competing, interdependent QDSC loss mechanisms to be quantified (including those losses arising from re-absorption of QD emitted light) for a given set of device parameters. Scattering of QD emitted light has, for the first time, been included in a QDSC ray-trace model. The model has been extensively validated through comparison with a range of electrical and spectral experimental measurements, and with predictions of other numerical models. Ray-trace modelling of QDSCs has, for the first time, been combined with outdoor solar radiation models. A novel analysis of diurnal and seasonal variations in QDSC electrical output in outdoor conditions for different QDSC configurations has been completed.

7.1 QDSC optimisation using the ray-trace approach

7.1.1 The effect of varying geometry on QDSC performance

2-D planar geometry

The net effect of varying device geometry on QDSC solar energy concentration ratios, C, was investigated using the ray-trace model. A novel analysis of device geometry was undertaken using the ray-trace predictions to calculate relative costs per unit power output of varying two-dimensional planar QDSC shapes. The analysis shows that, under certain assumptions[xvi], all geometries attain the same minimum cost per unit power, indicating that no advantage accrues from varying the plate shape. The model predictions show that the correct selection of concentrator top surface aperture area is crucial in minimising QDSC cost per unit power output. PV cells should be attached at all plate perimeter sides. Bi-facial PV cells could result in up to 25% decrease in the cost per W_p of an optimised QDSC.

Tapered geometry

Re-absorption losses, which increase with higher QD doping concentration levels, severely limit the potential C of QDSC devices. Current fabricated devices utilise a planar geometry with plates of uniform thickness. A novel tapered QDSC device was proposed with the aim of reducing re-absorption losses in the QDSC. Tapered plates, with one PV cell attached to the thin end, allow a lower QD doping concentration to be used to attain a given absorption efficiency, without decreasing

[xvi] i.e. assuming a uniform spatial distribution of photons incident on attached PV cells

the geometric gain of the device. With the lower QD doping concentration, re-absorption losses in the plate are reduced. The disadvantage, however, is that the internal optical efficiency decreases due to the sloped top and rear surfaces of the tapered device. Ray-trace modelling was used to investigate the *net effect* on device C. The results show an overall decrease in C for tapered devices, compared to plates of uniform thickness.

7.1.2 QD and matrix material optical properties.

QD optical properties

Escape cone losses in QDSCs have been quantified for the first time using ray-trace modelling. Predicted escape cone losses accounted for 58% of incident photons absorbed in one particular QDSC containing visible-emitting QDs. This is much higher than the ~25% minimum escape cone loss, assuming a luminescent species with no spectral overlaps in the same plate. Therefore, even allowing for ideal QYs, the commercially-available visible-emitting QDs are unlikely to be suitable candidates for inclusion in viable QDSCs, due to spectral overlaps and the resulting re-absorption losses. Re-absorption losses vary considerably between different QD types. The NIR emitting QDs modelled have significantly lower re-absorption losses owing to the profile of their absorption cross-section. Coupled with the broader absorption range, NIR emitting QDs remain potential candidates for viable QDSCs provided higher luminescent QYs are attained.

Matrix materials

Higher matrix material refractive index, n, results in reduced escape cone losses but increased external reflection losses. The ray-trace model is used to determine device concentration ratios for any particular matrix material parameters (i.e., n and absorption coefficient, α_{mat}). The analysis shows that attempts to increase device efficiency by increasing n, must consider the possibly greater negative effect of any variation in α_{mat}. The primary experimental objective should be to reduce (and stabilise) matrix material light absorption. Higher refractive index materials should be used only if this criterion is fulfilled.

7.1.3 External reflectors

Specular/diffuse rear reflectors

Research in the literature has shown that utilizing a rear reflector with a diffuse angular reflection distribution results in increased device C under normally incident direct light. This analysis has quantified, for the first time, the increase in C as a function of luminescent QY, and has shown that the advantage of employing a diffuse rear reflector reduces with more efficient QDSCs. Assuming a *diffuse insolation* angular distribution, there is no significant difference in predicted C for devices utilizing either reflector type. It is concluded, therefore, that the *reflectivity* of the reflector, and its *cost*, that are the most important considerations for a viable QDSC rear reflector, and not the reflector *type*.

Spectrally selective reflector top layers

Spectrally selective reflector (SSR) top layers can reduce escape-cone losses in the device by reflecting QD emitted light within the angular range of the escape cone, while transmitting incident light in the QD absorption range into the device. It has been shown that the ray-trace model provides a useful tool for optimizing the SSR cut-off wavelength for any particular luminescent species.

The modelling predictions of SSR top layers can partly explain why limited gains have been obtained to date utilizing such layers. Photons reflected by the SSR layer re-enter the device at a small angle, and therefore multiple reflections are required at the SSR interface (and at the rear reflector) before the photon is transmitted to the plate edges. Therefore, even a small decrease in SSR reflectivity results in significant reflection losses. For the same reason, it is of critical importance to utilise a highly reflective *rear* reflector when measuring the performance of any SSR top layer, a criterion which has not previously been emphasised in the research work carried out on SSRs in LSCs.

7.1.4 QDSC outdoor performance predictions

Ray-trace modelling of QDSCs has, for the first time, been combined with solar radiation models allowing a novel analysis of QDSC electrical output in outdoor conditions for different QDSC configurations. Diurnal and seasonal variations in QDSC performance on a tilted plane were analysed.

Predicted QDSC concentration ratio, C, is higher in mornings and evenings than at mid-day. There is a higher diffuse component at those times, which results in a higher QDSC absorption efficiency due to (i) a more blue-rich spectrum better

matching the QD absorption spectrum, and (ii) larger angles of incidence and, hence, a longer pathlength on a double pass through the QDSC plate. Higher C at times when global irradiance is low is a further advantage of QDSC devices, in that the useful daily operating time of the PV cells is extended. The predicted C for a particular QDSC, under the standard AM1.5G spectrum at normal incidence, is 2.8. In outdoor simulations annual average C of the same QDSC is much higher - varying between 3.7 and 4.2 throughout the day. The results highlight the advantage of using QDSCs in climates where the diffuse component of solar radiation is predominant. It also highlights the need to determine device annual *energy* yields, and not only power output under STCs, when comparing LSC performance with that of conventional PV cells.

The predicted monthly optimum tilt angle, β, at the Dublin location varies from ~15° in summer months to ~80° in winter, with a broad annual optimum between 20° and 30°. Compared to a QDSC fixed at β = 30°, a 13% increase in annual energy yield is predicted assuming one-axis tracking with the axis oriented east-west. QDSCs as low cost devices are, therefore, unlikely to benefit from utilization of solar tracking due to the additional associated installation and maintenance costs of tracking devices.

A 5% increase in annual QDSC energy yield is predicted with an increase in QDSC plate refractive index, n, from 1.5 to 1.7. This is significantly lower than the predicted increases observed under direct normal insolation (i.e. 10%), due to larger external top surface reflection losses in outdoor conditions. The results further highlight that the primary experimental research, regarding matrix materials, should be to reduce (and stabilise) light absorption. Higher refractive index materials should be used only if this criterion is fulfilled.

Annual external reflection losses account for 13% of total photons incident on a particular QDSC fixed at β = 30°. Utilizing an anti-reflective coating (ARC), reflection losses can be significantly reduced at particular wavelengths. The outdoor modelling predictions show that the ARC thickness needs to be optimised to maximise QDSC output and not to minimise total reflection losses. A potential 8% increase in QDSC annual energy yield is predicted using an external ARC. Gains would need to be evaluated in terms of the relative increase in costs of applying a robust ARC to a low-cost QDSC module.

7.1.5 QDSC cost analysis

QDSC cost per W_p is a function of top surface aperture area. Optimised QDSC cost per W_p have been quantified for varying QD QY under different cost scenarios. The results show that, even in the high cost scenario, QDSCs utilizing PbS near infra-red emitting QDs, can compete with "1st generation" silicon PV costs per W_p, provided high QYs can be exploited.

The low C attained by QDSCs fabricated to-date have been attributed to low QYs and large spectral overlaps between QD photon emission and absorption spectra. Initial motivation for developing the QDSC ray-trace model was to investigate the realistic potential performance of QDSCs (subject to the spectral overlap limitations), assuming QDs with high QY could be encapsulated in suitable matrix materials. The predictions show that viable QDSCs are realizable without the need for a spectrally selective reflector top layer, providing efficient NIR emitting QDs can be exploited. The ray-trace model now developed provides an important

tool for optimizing device design for outdoor conditions, and minimizing the costs per unit energy produced.

7.2 Luminescent down shifting layers

Luminescent down-shifting (LDS) layers can enhance the short circuit current density, J_{sc}, of solar cells by transforming the wavelength of incident light from short to longer wavelengths better matching the spectral response of the cell. LDS layers were modelled, to investigate whether the optical properties of *QDs* (i.e. broad absorption range and characteristic increased absorption in the UV and blue wavelength regions) make them a more suitable candidate than organic dyes for incorporation in LDS layers. Predictions for LDS layers containing two types of commercially available QDs show that only a limited potential enhancement in mc-Si cell J_{sc} (1% relative increase) is attained[xvii]. This is significantly lower than analytical predictions in the research literature which yielded 7.5 % - 10% relative increase in J_{sc}.

7.2.1 Partially covered luminescent down shifting layers

In "partially-covered" LDS (PC-LDS) layers a reduced fraction of the down-shifting layer is covered with PV cells, thereby introducing a geometric concentration effect not present in an LDS layer. The performance of PC-LDS layers incorporating currently available luminescent dyes has been quantified for the first

[xvii] even assuming a near ideal QD QY of 98%

time for varying plate size and coverage fractions. As with LSC plates, the optimum size of a PC-LDS layer, of given parameters, must be determined.

Current single-plate LSCs, utilising mc-Si cells, have power conversion efficiencies, η, of 2.5 – 3.8% (depending on the geometric gain) under standard test conditions. The ray-trace predictions show that employing the same PV cells and matrix materials in the *PC-LDS* layer configuration could increase η significantly, as compared to the LSC device. As the absorption range of LSCs extends towards the attached PV cell band gap, the magnitude of the potential increase in η diminishes. However, it is a simple effective method to further increase η, in what are currently the most efficient LSCs utilising mc-Si cells.

7.3 Luminescent "solar tree"

A luminescent "solar tree" system was proposed, where fibre optics are used to transmit light exiting multiple plates, or "solar leaves", to a single PV cell via a 2nd stage concentrator. Potentially, the concept allows high concentration ratios to be attained under direct or *diffuse* insolation conditions. However, the maximum concentration ratio of the 2nd stage concentrator, C_2, is limited by the angular distribution of light exiting the fibre optics. It is shown that the limitations in C_2, combined with the additional associated costs of the fibre optics required, result in no cost per unit power reduction for the solar tree structure compared with that of a single-plate QDSC.

7.4 Future direction of model development

7.4.1 Spectral irradiance modelling

The spectral irradiance approximations, detailed in section 5.1.6, should be compared with measured spectral irradiance data to quantify the error arising from using the approximated spectra in outdoor modelling predictions. Comparisons could also be made with spectral irradiance models, such as the parameterised semi-empirical SPCTRL2 (Bird and Riordan, 1986) and SEDES2 (Nann and Riordan, 1991; Nann and Emery, 1992) models.

7.4.2 PV cell modelling

Currently the model calculates the PV cell short circuit current using the edge emission spectrum and measured cell IQE and reflectivity data. Angular dependent reflectivity curves are approximated from the optical properties of the cell material. A more detailed PV model could quantify the variation in cell internal resistance, open circuit voltage, and fill factor, under varying light intensity, spectra, and temperature. Modelling the cell temperature would be complex as it would also depend on the heat transfer to/from the polymer plate. The plate temperature would need to be calculated taking into account non-radiative recombination of absorbed solar energy by the luminescent species, matrix material photon absorption, ambient temperature and temperature increases in the cell.

7.5 References

Bende, E.E., Slooff, L.H., Burgers, A.R., van Sark, W.G.J.H.M., Kennedy, M., (2008). Cost & Efficiency Optimisation of the Luminescent Solar Concentrator. *Proceedings of 23rd European Photovoltaic Solar Energy Conference*, Valencia, Spain, 461-70.

Bird, R.E., Riordan, C., (1986). Simple Solar Spectral Model for Direct and Diffuse Irradiance on Horizontal and Tilted Planes at the Earth's Surface for Cloudless Atmospheres. *Journal of Climate and Applied Meteorology,* 25, 87-97.

Bose, R., Farrell, D.J., Chatten, A.J., Pravettoni, M., Büchtemann, A., Barnham, K.W.J., (2007). Novel configurations of luminescent solar concentrators. *Proceedings of 22nd European Photovoltaic Solar Energy Conference and Exhibition*, Milan, Italy, 210-4.

Gallagher, S.J., Rowan, B.C., Doran, J., Norton, B., (2007). Quantum dot solar concentrator: Device optimisation using spectroscopic techniques. *Solar Energy,* 81, 4, 540-7.

Hübner, A., Aberle, A.G., Hezel, R., (1997). Novel cost-effective bifacial silicon solar cells with 19.4% front and 18.1% rear efficiency. *Applied Physics Letters,* 70, 8, 1008-10.

Nann, S., Emery, K., (1992). Spectral effects on PV-device rating. *Solar Energy Materials and Solar Cells,* 27, 189-216.

Nann, S., Riordan, C., (1991). Solar Spectral Irradiance under Clear and Cloudy Skies: Measurements and a Semiempirical model. *Journal of Applied Meteorology,* 30, 447-62.

Rowan, B.C., Wilson, L.R., Richards, B.S., (2008). Advanced material concepts for luminescent solar concentrators. *IEEE Journal of Selected Topics In Quantum Electronics,* 14, 5, 1312-22.

Sholin, V., Olson, J.D., Carter, S.A., (2007). Semiconducting polymers and quantum dots in luminescent solar concentrators for solar energy harvesting. *Journal of Applied Physics,* 101, 1231141-9.

Appendix A

Solar tree relative cost per unit power

In this section, the relative cost per unit power output of the scalable solar tree system, described in section 3.2, is determined;

Positioning all FOs used in the system adjacently, as illustrated in Figure A.1, the total planar 'area' of FOs, A_{FO}, is defined by;

$$A_{FO} = \overline{L_{FO}}\, W_{FO}\, N_{FO} \qquad \text{A.1}$$

where, $\overline{L_{FO}}$ is the average FO length and N_{FO} is the total number of FOs. Expressing the quantity of FO in units of planar area allows the dimensionless variable *costfactor*$_2$ to approximate the cost of the FO relative to the cost of a unit area of PV.

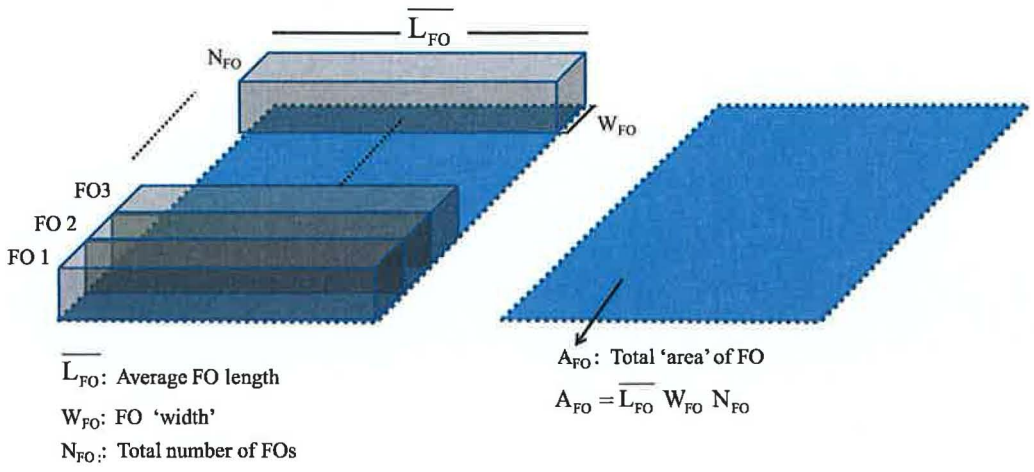

Figure A.1. The total 'area' of FO, A_{FO}, is equal to the product of the average FO length, times the FO 'width', times the total number of FOs.

Relative cost

The relative cost of a particular sized solar tree system, excluding the cost of the 2nd stage concentrator, is dependent on (i) A_{pv}, (ii) the number of leaves, N_{Leaf}, and the leaf dimensions, W_{Leaf} and L_{Leaf}, and (iii) the 'area' of fibre optics, A_{FO};

$$\begin{aligned} \text{cost} &= A_{pv} + \frac{W_{Leaf} L_{Leaf} N_{Leaf}}{costfactor_1} + \frac{A_{FO}}{costfactor_2} \\ &= A_{pv} + \frac{W_{Leaf} L_{Leaf} N_{Leaf}}{costfactor_1} + \frac{\bar{L}_{FO} W_{FO} N_{FO}}{costfactor_2} \end{aligned} \quad \text{A.2}$$

where, $costfactor_1$ and $costfactor_2$ relate the cost of the leaves and FO, respectively, to the cost of the PV per unit area;

$$\begin{aligned} costfactor_1 &= \frac{\text{cost of PV cells per m}^2}{\text{cost of solar leaf per m}^2} \\ costfactor_2 &= \frac{\text{cost of PV cells per m}^2}{\text{cost of fibre optic per m}^2} \end{aligned} \quad \text{A.3}$$

The number of leaves used, N_{Leaf}, in a particular tree system can be expressed relative to the area of PV cell used as follows;

In a scaleable solar tree system N_{FO} is related to N_{Leaf} by;

$$N_{FO} = N_{Leaf} \frac{W_{Leaf}}{W_{FO}} \quad \text{A.4}$$

where, W_{FO} is the 'width' of each FO. From Figure 3.14, the total cross-sectional area of the FOB, A_{cs_FOB}, is related to A_{pv} by;

$$C_G = \frac{A_{cs\_FOB}}{A_{pv}} = \frac{W_{FO}^2 N_{FO}}{A_{pv}} \quad \text{A.5}$$

substituting A.4 into A.5;

$$C_G = \frac{W_{FO}^2 N_{Leaf} W_{Leaf}}{A_{pv} W_{FO}} \quad \text{A.6}$$

N_{Leaf}, in a scalable solar tree system, is therefore related to A_{pv} by;

$$N_{Leaf} = \frac{C_G A_{pv}}{W_{FO} W_{Leaf}} \quad \text{A.7}$$

substituting eqns. A.4 and A.7 into eqn. A.2, the total relative cost is given by;

$$\text{rel. cost} = A_{pv} + \frac{L_{Leaf} C_G A_{pv}}{W_{FO}\ costfactor_1} + \frac{\overline{L_{FO}} C_G A_{pv}}{W_{FO}\ costfactor_2} \quad \text{A.8}$$

Relative power

The relative power of a scalable solar tree system is determined by the area of PV, C_1, and C_2;

$$\text{rel. power} = A_{pv} C_1 C_2 \quad \text{A.9}$$

Relative cost per unit power

Dividing eqn. A.8 by eqn. A.9 yields the lower bound relative cost per unit power of the solar tree;

$$\text{rel. cost/power} = \frac{1}{C_1 C_2} + \frac{L_{Leaf} C_G}{C_1 C_2 W_{FO} costfactor_1} + \frac{\overline{L_{FO}} C_G}{C_1 C_2 W_{FO}^2 costfactor_2} \qquad \text{A.10}$$

Appendix B

The measured horizontal global irradiance data in section 5.1 are converted from local standard time to "Solar time". Solar time describes the angular motion of the sun across the sky at a particular location, with solar noon occurring when the sun reaches maximum altitude as observed from that location. The sun takes 1 hour to traverse 15° of longitude, i.e., solar time lags local standard time by 4 minutes for every one degree west of the reference longitude. The rate of the earth's rotation on its own axis varies throughout the year. The variation is described by the equation of time. The equation of time (EOT), as a function of the Julian day of the year (day_J), is shown in Figure B.1 and is given (Duffie and Beckman, 1990) by;

$$EOT = 9.87\sin 2B - 7.53\cos B - 1.5\sin B \quad ,$$

where;

$$B(\text{degrees}) = \frac{360(day_J - 81)}{364} \qquad \text{B.1}$$

Solar time at a particular longitude is related to local standard time[xviii] by;

$$\text{solar time} = \text{local standard time} + 4(L_{ref} - L_{loc}) + EOT$$

where, L_{loc} is the location longitude in degrees west of the reference longitude, L_{ref}.

[xviii] Local standard time remains at Winter Time all year and does not change forward one hour in Summer Time.

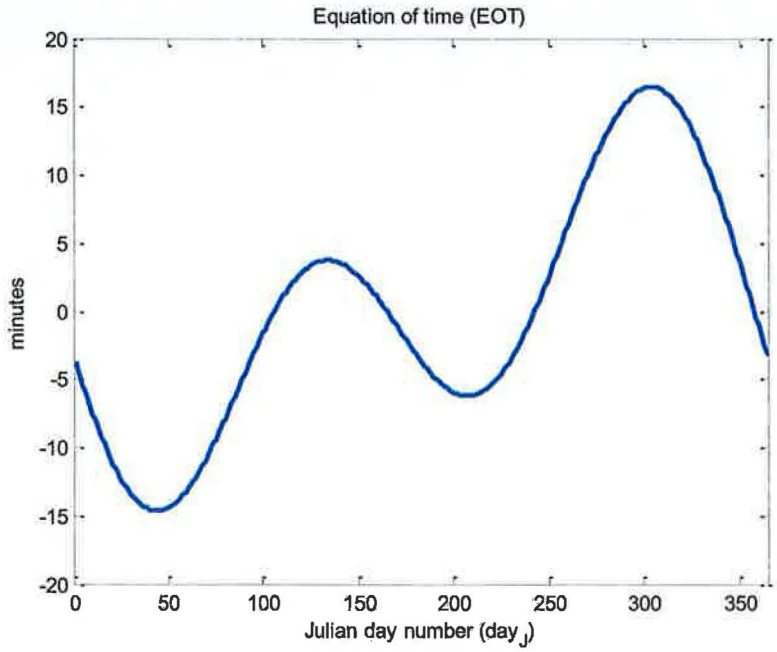

Figure B.1. The equation of time (EOT), given by eqn. B.1, accounting for the variation about the mean of the earth's rotation time on its own axis.

Appendix C

The sky clearness parameter, ε, used in eqn. 5.13 to determine the Perez circumsolar and horizon brightening coefficients, increases as sky conditions change from heavy overcast to a low turbidity clear sky and is defined as;

$$\varepsilon = \left(\frac{D_h + B_n}{D_h} + \kappa\theta_s^3 \right) \Big/ \left(1 + \kappa\theta_s^3 \right)$$

with the dimensionless constant κ = 1.041 and the other parameters defined in section 5.

The Perez coefficients, f_{ij}, are dependent on ε and are given in Table C.1.

ε	ε bin	f_{11}	f_{12}	f_{13}	f_{21}	f_{22}	f_{23}
$\varepsilon < 1.065$	1	-0.008	0.588	-0.062	-0.060	0.072	-0.022
$1.065 \leq \varepsilon < 1.23$	2	0.130	0.683	-0.151	-0.019	0.066	-0.029
$1.23 \leq \varepsilon < 1.50$	3	0.330	0.487	-0.221	0.055	-0.064	-0.026
$1.5 \leq \varepsilon < 1.95$	4	0.568	0.187	-0.295	0.109	-0.152	-0.014
$1.95 \leq \varepsilon < 2.80$	5	0.873	-0.392	-0.362	0.226	-0.462	0.001
$2.80 \leq \varepsilon < 4.50$	6	1.132	-1.237	-0.412	0.288	-0.823	0.056
$4.50 \leq \varepsilon < 6.20$	7	1.060	-1.600	-0.359	0.264	-1.127	0.131
$6.20 \leq \varepsilon$	8	0.678	-0.327	-0.250	0.156	-1.377	0.251

Table C.1. Perez coefficients, f_{ij}

Appendix D

The reflectance from the anti-reflective coatings, R, simulated in section 5.3 is determined below. R depends on the angle of incidence, θ_1, the wavelength of the incident light, λ_1 and the thickness of the thin-film, t_f;

$$R = \frac{R_p + R_s}{2} \quad \text{, where}$$

$$R_p = \frac{r_{12p}^2 + r_{23p}^2 + 2r_{12p}r_{23p}\cos 2\beta}{1 + r_{12p}^2 + r_{23p}^2 + 2r_{12p}r_{23p}\cos 2\beta} \quad \text{and} \quad R_s = \frac{r_{12s}^2 + r_{23s}^2 + 2r_{12s}r_{23s}\cos 2\beta}{1 + r_{12s}^2 + r_{23s}^2 + 2r_{12s}r_{23s}\cos 2\beta}$$

where β is the phase difference, in the external medium, between waves reflected from the first and second surfaces of the coating;

$$\beta = \frac{2\pi}{\lambda_1} n_2 t_f \cos\theta_2$$

The amplitude reflectance coefficients at the interface between the external medium and the ARC are given by;

$$r_{12p} = \frac{n_2\cos\theta_1 - n_1\cos\theta_2}{n_2\cos\theta_1 + n_1\cos\theta_2} \quad \text{and} \quad r_{12s} = \frac{n_1\cos\theta_1 - n_2\cos\theta_2}{n_1\cos\theta_1 + n_2\cos\theta_2}$$

and the amplitude reflectance coefficients at the interface between the ARC and the substrate (LSC plate) are given by;

$$r_{23p} = \frac{n_3\cos\theta_2 - n_2\cos\theta_3}{n_3\cos\theta_2 + n_2\cos\theta_3} \quad \text{and} \quad r_{23s} = \frac{n_2\cos\theta_2 - n_3\cos\theta_3}{n_2\cos\theta_2 + n_3\cos\theta_3}$$

where $n_1, n_2,$ and n_3 are the refractive indicies of the external medium, ARC, and substrate, respectively.

List of Publications

Journal publications

Kennedy, M., McCormack, S.J., Doran, J., Norton, B., (2009). Improving the optical efficiency and concentration of a single-plate quantum dot solar concentrator using near infra-red emitting quantum dots. *Solar Energy,* 83, 7, 978-81.

van Sark, W.G.J.H.M., Barnham, K.W.J., Slooff, L.H., Büchtemann, A., Meyer, A., McLafferty, J.B., Koole, R., Chatten, A.J., Farrell, D.J., Bose, R., Bende, E.E., Quilitz, J., Kennedy, M., Meyer, T., Wadman, S.H., Meijerink, A., Vanmaekelbergh, D., (2008). Luminescent Solar Concentrators - A review of recent results. *Optics Express,* 16, 26, 21773-92.

Conference publications

Kennedy, M., Chatten, A.J., Farrell, D.J., Bose, R., Büchtemann, A., McCormack, S.J., Doran, J., Barnham, K.W.J., Norton, B., (2008). Luminescent Solar Concentrators: A Comparison of Thermodynamic Modelling and Ray-trace Modelling Predictions. *Proceedings of 23rd European Photovoltaic Solar Energy Conference and Exhibition*, Valencia, Spain, 334-7.

Kennedy, M., Dunne, M., McCormack, S.J., Doran, J., Norton, B., (2008). Multiple dye luminescent solar concentrators and comparison with Monte-Carlo ray-trace predictions. *Proceedings of 23rd European Photovoltaic Solar Energy Conference and Exhibition*, Valencia, Spain, 390-3.

Kennedy, M., McCormack, S.J., Doran, J., Norton, B., (2007). Modelling the effect of device geometry on concentration ratios of quantum dot solar concentrators. *Proceedings of International Solar Energy Society World Solar Congress*, Beijing, China, 1484-8.

Kennedy, M., McCormack, S.J., Doran, J., Norton, B., (2007). Modelling of Re-absorption Losses in Quantum Dot Solar Concentrators. *Proceedings of 3rd Photovoltaic Science Application and Technology Conference*, Durham, UK, 123-6.

Kennedy, M., Rowan, B.C., McCormack, S.J., Doran, J., Norton, B., (2007). Modelling of a Quantum Dot Solar Concentrator and Comparison with Fabricated Devices. *Proceedings of 3rd Photovoltaic Science Application and Technology Conference*, Durham, UK, 27-30.

Kennedy, M., McCormack, S.J., Doran, J., Norton, B., (2007). Ray-trace modelling of reflectors for Quantum Dot Solar Concentrators. *Proceedings of SPIE Optics and Photonics and Solar Energy Conference*, San Diego, USA, (CD).

Bende, E.E., Slooff, L.H., Burgers, A.R., van Sark, W.G.J.H.M., Kennedy, M., (2008). Cost & Efficiency Optimisation of the Luminescent Solar Concentrator. *Proceedings of 23rd European Photovoltaic Solar Energy Conference*, Valencia, Spain, 461-70.